

AD-A225 472

DTIC FILE COPY

②

NONLINEAR ANALYSIS OF UBITRON, ORBITRON,
AND GYROHARMONITRON MECHANISMS
SAIC FINAL REPORT NO. 87/1163
NOVEMBER 1987



Science Applications International Corporation

Approved for public release
Distribution Unlimited

DTIC
ELECTE
AUG 22 1990
S B D
CP

98 07 20 123

NONLINEAR ANALYSIS OF UBITRON, ORBITRON,
AND GYROHARMONITRON MECHANISMS
SAIC FINAL REPORT NO. 87/1163
NOVEMBER 1987

SAIC

Science Applications International Corporation

2

NONLINEAR ANALYSIS OF UBITRON, ORBITRON,
AND GYROHARMONITRON MECHANISMS

SAIC FINAL REPORT NO. 87/1163

Submitted to:

Microwave and Millimeter Wave Tube Technology
Branch, Code 6840
Electronics Technology Division
Naval Research Laboratory
Washington, D.C. 20375

Submitted by:

Science Applications International Corporation
1710 Goodridge Drive
McLean, Virginia 22102

Prepared under:
Contract No. N00014-86-C-2042

November 1987

Approved for public release
Distribution Unlimited

A. K. Goumy

DTIC
ELECTE
AUG 22 1990
S B D

TABLE OF CONTENTS

ABSTRACT 1

1. GENERAL DISCUSSION 3

REFERENCES 14

APPENDIX I: THREE-DIMENSIONAL NONLINEAR
ANALYSIS OF FREE-ELECTRON
LASER AMPLIFIERS WITH PLANAR
WIGGLERS A-I

APPENDIX II: HARMONIC GENERATION IN FREE-ELECTRON
LASERS A-II

APPENDIX III: MULTI-MODE NONLINEAR ANALYSIS OF
FREE-ELECTRON LASER AMPLIFIERS IN
THREE DIMENSIONS A-III

APPENDIX IV: EFFICIENCY ENHANCEMENT IN
FREE-ELECTRON LASERS DRIVEN BY
ELECTROMAGNETIC-WAVE WIGGLERS A-IV



Accession For	
NTIS GRA&I	<input checked="" type="checkbox"/>
DTIC TAB	<input type="checkbox"/>
Unannounced	<input type="checkbox"/>
Justification	
By <i>per Form 50</i>	
Distribution/	
Availability Codes	
Dist	Avail and/or Special
<i>A-1</i>	

ABSTRACT

The research program during the contract period consisted of the analysis of the Ubitron/FEL amplifier in three-dimensions. The principal configuration of interest consisted of the propagation of an energetic electron beam through a loss-free rectangular waveguide in the presence of a linearly polarized wiggler field with parabolically tapered pole pieces. The purpose of the tapered pole faces is to provide a mechanism for focussing the electron beam in the plane of the bulk wiggler induced oscillation. A nonlinear theory and simulation code has been developed to study this configuration which can treat a multiple mode interaction, harmonic growth, efficiency enhancement by means of a tapered wiggler, the effect of beam thermal spread on the interaction, the injection of the beam into the wiggler, and detailed facets of the particle dynamics such as Betatron oscillations and velocity shear. Comparisons of the experiment at the Lawrence Livermore National Laboratory are excellent. Some of the principal results of the simulation relate to the harmonic and tapered wiggler interactions. In the case of the harmonic interaction, the nonlinear simulation shows both high gain and good efficiency at the harmonics, although the interaction is increasingly sensitive to the effects of

velocity spread at the higher harmonics. The tapered wiggler interaction shows high efficiencies are possible and that one effect of the tapered wiggler is to reduce the sensitivity to beam velocity spread. An additional area of study is the enhancement of the efficiency of a configuration based upon an electromagnetic wave wiggler by means of the tapering of an external axial guide field. The purpose of the electromagnetic wave wiggler is to achieve a higher operating frequency for a given beam energy (relative to a magnetostatic wiggler), however, electromagnetic wave wigglers are inherently more difficult to control (i.e. taper) for efficiency enhancement purposes. Thus, the use of a tapered axial guide field for this reason may have important applications.

1. GENERAL DISCUSSION

The fundamental interaction mechanism of the Ubitron is the same as that of the Free-Electron Laser (FEL), the distinction between the two is that the term Ubitron specifically refers to a microwave tube while the term FEL is often used to describe devices operating over the entire spectrum. The common Ubitron/FEL interaction mechanism derives from the propagation of an energetic (but not necessary relativistic) electron beam through a rippled magnetic field (called a "wiggler" or "undulator"). The effect of the wiggler field is to induce an oscillation in the transverse velocity which is to induce an oscillation in the transverse velocity which gives rise to spontaneous or incoherent radiation. Coherent radiation arises from electron bunching in the ponderomotive potential formed by the beating of the radiation and wiggler fields. The wavelength of the output radiation depends on both the period of the wiggler field and the energy of the electron beam, and experiments have proven the mechanism to operate over wavelengths ranging from the microwave through the visible spectra. Within this context, therefore, the Ubitron represents a specific application of the concept to the microwave regime and we shall use the term to describe

FEL's which employ electron beams with energies less than about 500 keV.

The primary configuration studied during the contract period consisted of the propagation of an electron beam through a loss-free rectangular waveguide in the presence of a linearly polarized wiggler field. The principal motivation for this work derives from the interest in Code 6840 at the Naval Research Laboratory in Ubitrons based upon extremely short period planar wigglers and/or higher harmonic Ubitrons. The advantage to be derived from such configurations is the possibility of generating high frequency radiation using low energy electron beams. The detailed wiggler field model we employ describes a planar wiggler with parabolically tapered pole faces. This type of wiggler field provides for enhanced focussing in the direction of the bulk-wiggler-induced motion, and was first employed experimentally by Phillips¹. An analytic model for this type of field has been given by Scharlemann², who found that the field can be represented in the form

$$B_w(x) = B_w \left[\cos k_w z \left[\sinh \left[\frac{k_w x}{\sqrt{2}} \right] \sinh \left[\frac{k_w y}{\sqrt{2}} \right] \hat{e}_x \right. \right. \\ \left. \left. + \cosh \left[\frac{k_w x}{\sqrt{2}} \right] \cosh \left[\frac{k_w y}{\sqrt{2}} \right] \hat{e}_y \right] \right]$$

$$- \sqrt{2} \sin k_w z \cosh \left[\frac{k_w x}{\sqrt{2}} \right] \sinh \left[\frac{k_w y}{\sqrt{2}} \right] \hat{e}_z \Bigg\} ,$$

where B_w denotes the amplitude and k_w ($\equiv 2\pi/\lambda_w$, where λ_w is the period) represents the wavenumber.

The analytical technique employed is based upon experience gained in the extensive prior treatment of Ubitron/FEL configurations based upon helical wiggler fields³⁻⁵. Since we are interested in an amplifier model only single-frequency wave propagation is considered, which permits Maxwell's equations to be averaged over a wave period. As a result, the fast time scale phenomena are eliminated from the problem. In addition, only a "beamlet" of electrons which enter the interaction region within one wave period needs to be included in the analysis. These two benefits result in major improvements in computational efficiency in comparison with full-scale particle-in-cell simulation codes. The boundary conditions imposed by the waveguide wall may be treated by the expansion of the radiation field in terms of the vacuum waveguide modes. In previous work with helical wiggler configurations a cylindrical waveguide was assumed; however, in treating the planar wiggler, we have assumed the boundary conditions to be determined by a rectangular waveguide.

While our primary interest is in the use of short period wigglers and higher harmonic interactions which permit high frequency operation with moderate energy electron beams, the only operational experiment against which our nonlinear theory can be compared is the ELF experiment at Lawrence Livermore National Laboratory^{6,7}. The ELF experiment makes use of a 3.5 MeV electron beam and a planar wiggler field with a 9.8 cm period and an amplitude of as much as 4 kG to obtain operation at a frequency of 35 GHz. As a consequence, the initial development and testing of the simulation code were performed for this experiment.

The initial formulation described a single-mode analysis, and gave results in reasonable agreement with the experiment. The analytical treatment and numerical results have been published in Physical Review A (see Appendix I). Resonant interaction was found with the TE_{01} , TE_{21} , TM_{21} modes. The saturated powers found for the TE modes were of the order of 200 MW which is comparable to that observed experimentally. The coupling to the TM mode is weaker than for either of the TE modes, and both the gain and saturated power are substantially lower than for the TE_{01} and TE_{21} modes.

The principal difference between the nonlinear analysis developed under the present contract and other treatments, such as described in the FRED code in use at the Lawrence Livermore National Laboratory⁷, is in the treatment of the particle dynamics. The particle orbits are treated by means of a reduced set of orbit equations obtained by an average of the Lorentz force equations over a wiggler period in FRED and virtually every other nonlinear treatment of the Free-Electron Laser. The average of the orbit equations is not performed in the present analysis, however, and the full set of Lorentz force equations (i.e., in three dimensions) is integrated for each particle in the simulation. As a result, the particle dynamics are treated more accurately in the present analysis than in simulation codes such as FRED. This is important in the description of the planar wiggler interaction because the magnitude of the bulk wiggler velocity is not constant for this configuration, and an oscillation occurs in the axial velocity with a period of half the wiggler wavelength. This rapid oscillation is lost when the orbit equations are averaged over a wiggler period, but manifests itself in an oscillation in both the wave power and phase at a wavelength of $\lambda_w/2$. While this does not affect the bulk growth of the wave, it does introduce an uncertainty in the measurement of the axial evolution of the wave power and phase which may be as high as 10-20%.

One advantage of the more accurate treatment of the particle dynamics employed in the present analysis is that the injection of the beam into the wiggler may be modelled. The injection process is crucial to the efficient operation of the Free-Electron Laser because poor matching of the beam into the wiggler can result in a large axial energy spread which degrades the interaction efficiency. In order to minimize this problem most experimental configurations employ an adiabatic entry taper on the wiggler amplitude which, in most cases, exceeds four wiggler periods in length. Simulation of the injection process shows that the adiabatic injection process is effective for entry taper regions longer than approximately 4-5 wiggler periods. Entry taper regions shorter than this are found to result in substantial declines in the operating efficiency.

A second advantage that derives from the improved treatment of the particle dynamics is that the analysis is applicable to the study of harmonic radiation. The harmonic interaction holds promise for the production of high frequency radiation using electron beams of moderate energy. This is an important future application of the analysis. However, in experiments designed to operate in the visible spectrum, the harmonic radiation would occur in the ultraviolet which can result in fatal damage to the optical

system As a result, the efficiencies and growth rates of the harmonic interaction can have important implications for a wide variety of Free-Electron Laser applications. The nonlinear simulation indicates that the harmonic interaction in a planar wiggler can be significant with growth rates comparable to that found at the fundamental. The saturation efficiency is found to decrease most sharply between the fundamental and the first harmonic, but shows a weak variation with harmonic number thereafter. Thus, the total power carried by the harmonics can be a significant fraction of that found at the fundamental. This is a particularly encouraging result from the standpoint of the design of a higher harmonic device. However, the simulation also shows that the harmonics are substantially more sensitive to the effect of an axial energy spread than the fundamental, and more precise control of the electron beam will be required to perform a harmonic experiment. These results have been published in Physical Review A (see Appendix II).

Another important configuration employed in the Free-Electron Laser interaction mechanism is the enhancement of the saturation efficiency by means of a tapered wiggler. The physical basis for the efficiency enhancement can be explained by first noting that wave-particle resonance in the Free-Electron laser occurs when $\omega \approx (k + k_w) v_z$, where

v_z denotes the axial electron velocity, k_w is the wiggler wavenumber, and (ω, k) denote the frequency and wavenumber of the radiation. As the beam gives up energy to the waves, the axial electron velocity decreases and the particles drop out of resonance with the wave. The purpose of the wiggler tapering is to accelerate the beam in the axial direction so as to maintain the resonance over an extended interaction length. This can be accomplished by means of a decrease in the wiggler amplitude which affects the partition of energy between motion in the perpendicular and parallel directions by decreasing the perpendicular velocity of the bulk wiggler motion while increasing the axial velocity. The tapered wiggler interaction mechanism has been addressed in the nonlinear analysis (see Appendix I), with particular emphasis placed on the effects of an axial energy spread on the maximum achievable saturation efficiency. The principal result is that the tapered wiggler interaction is significantly less sensitive to the effect of the energy spread than is the case for a uniform wiggler. This is encouraging from the standpoint of the design of a tapered wiggler harmonic experiment, since the higher sensitivity to beam energy spread encountered for the harmonic interaction may be compensated for by the tapered wiggler. This will be an important area of future study.

Recognizing that a single-mode representation is not appropriate for an overmoded configuration in which the beam is resonant with more than one mode, we undertook to include multiple modes in the simulation. The procedure for the inclusion of multiple modes within the present formulation involves (1) the integration of particle trajectories in the presence of the aggregate field, and (2) the computation of the coupling of each mode to the total current to obtain the growth of the wave mode. It should be remarked that although multiple modes can be treated within the framework of the analysis, all the modes are at the same frequency in order to perform the average of the field equations over a wave period. The results of the analysis have been submitted for publication in the Physical Review A (Appendix III). The analysis has also been applied to the case of the experiment at LLNL⁷ with excellent results. The experiment made use of a 3.5 MeV/850 A electron beam with an initial radius of 1 cm propagating through a waveguide of 9.8 cm x 2.9 cm cross section. The wiggler field was characterized by an amplitude of 3.72 kG and a period of 9.8 cm. The input radiation source was a magnetron producing 50 kW at a frequency of 34.6 GHz predominantly in the TE₀₁ mode of the waveguide. The best estimates available⁸ indicate that, perhaps, 1% of the total power is carried by the TE₂₁ and TM₂₁ modes. The observed output power for a uniform

wiggler (i.e. constant amplitude) was 180 MW, and rose to 1GW (for an efficiency of 34%) when the amplitude was decreased by 55% over a distance of 1.1 m. The simulation code for these parameters yield an output power of 185 MW for the uniform wiggler case, and 1 GW for the tapered wiggler interaction. It is important to remark, however, that the theory is not in complete correspondence with the experiment. The most important difference lies in the use of tapered pole pieces to provide for beam focussing in the plane of the bulk wiggler motion in the simulation, while the experiment employed a quadrupole magnetic field for this purpose. For this reason, the excellent agreement between the theory and the experiment should not be overstated. However, it does indicate that the essential physics of the interaction is included in the theory, and the simulation will now be turned to the study of harmonic interactions in earnest.

Contributed papers on this work have been presented at the 9th Free Electron Laser Conference in Williamsburg, Virginia (9-13 September, 1987), and at the American Physical Society/Division of Plasma Physics meeting in San Diego, CA (2-6 November, 1987). In addition, recognition of the importance of these contributions to the understanding of the physics of the Ubitron/Free Electron Laser has

resulted in an invited paper presented at the 9th International Free-Electron Laser Conference.

An additional area of study is the configuration based upon electromagnetic wave wigglers. The advantage of this type of configuration is that a higher frequency interaction may be obtained for a given electron beam energy relative to a magnetostatic wiggler. However, one disadvantage of the electromagnetic wave wiggler is that it is more difficult to control (than magnetostatic wigglers) for the purpose of efficiency enhancement through a tapered amplitude or period. In order to circumvent this problem, we have proposed the use of an auxiliary axial guide field. The axial guide field is useful from the standpoint of confining (or focussing) the beam. However, the nonlinear interaction efficiency may be enhanced by tapering the guide field as easily as tapering the wiggler field⁴. As a consequence, we have analyzed the effect of a tapered axial guide field on the electromagnetic wave wiggler configuration, and the results have been published in the IEEE Journal of Quantum Electronics (see Appendix IV). The results indicate that the tapered axial guide field may have important applications to the enhancement of the efficiency in electromagnetic wave wiggler configurations.

REFERENCES

1. R. M. Phillips, IRE Trans. Electron Devices 7, 231 (1960).
2. E. T. Scharlemann, J. Appl. Phys. 58, 2154 (1985).
3. A. K. Ganguly and H. P. Freund, Phys. Rev. A 32, 2275 (1985).
4. H. P. Freund and A. K. Ganguly, Phys. Rev. A. 33, 1060 (1986).
5. H. P. Freund and A. K. Ganguly, Phys. Rev. A 34, 1242 (1986).
6. T. J. Orzechowski, B. Anderson, W. M. Fawley, D. Prosnitz, E. T. Scharlemann, S. Yarema, D. Hopkins, A. C. Paul, A. M. Sessler, and J. Wurtele, Phys. Rev. Lett. 54, 889 (1985).
7. T. J. Orzechowski, B. R. Anderson, J. C. Clark, W. M. Fawley, A. C. Paul, D. Prosnitz, E. T. Scharlemann, S. M. Yarema, D. B. Hopkins, A. M. Sessler, and J. S. Wurtele, Phys. Rev. Lett. 57, 2172 (1986).
8. T. J. Orzechowski, personal communication.

APPENDIX I

THREE-DIMENSIONAL NONLINEAR ANALYSIS
OF FREE-ELECTRON LASER AMPLIFIERS WITH
PLANAR WIGGLERS

Three-dimensional nonlinear analysis of free-electron-laser amplifiers with planar wigglers

H. P. Freund

Science Applications International Corporation, McLean, Virginia 22102

H. Bluem

Department of Electrical Engineering, University of Maryland, College Park, Maryland 20742

C. L. Chang

Science Applications International Corporation, McLean, Virginia 22102

(Received 23 March 1987)

The nonlinear evolution of the free-electron-laser (FEL) amplifier is investigated numerically for a configuration consisting of a planar wiggler with parabolically tapered pole pieces. A set of coupled nonlinear differential equations is derived in three dimensions which governs the self-consistent evolution of the TE and TM modes in a loss-free rectangular waveguide as well as the trajectories of an ensemble of electrons. The initial conditions are chosen to model the injection of a cylindrically symmetric electron beam into the wiggler by means of a region with an adiabatically tapered wiggler amplitude, and the effect of an initial beam momentum spread is included in the formulation. Both self-field and space-charge effects have been neglected, and the analysis is valid for the high-gain Compton regime. In addition, the phase stability of the FEL amplifier against fluctuations in the beam voltage, the enhancement of the efficiency by means of a tapered wiggler amplitude, and harmonic generation are also studied. Numerical simulations are conducted to model a 35-GHz amplifier with an electron beam energy of 3.5 MeV, and good agreement is found between the simulation and an experiment conducted by Orzechowski and co-workers. Significantly, the results indicate that a tapered wiggler configuration is somewhat less sensitive to the beam thermal spread than a uniform wiggler system.

I. INTRODUCTION

The free-electron laser (FEL) and the ubitron¹ have been successfully demonstrated as radiation sources over a broad frequency range from the microwave¹⁻¹³ through the optical¹⁴⁻²¹ spectra. The distinction between the ubitron and the FEL is not well defined in the literature; however, we find it convenient to differentiate between the FEL and the ubitron primarily on the basis of the electron-beam energy. As such, we refer to those devices as ubitrons when the beam energy is below 500 keV. Although this definition is somewhat arbitrary, operation at these energies generally involves frequencies close to the waveguide cutoff of the device, and the ubitron may be thought of as a weakly relativistic FEL operated as a microwave tube. In either case, however, the physical-interaction mechanism is the same, and relies on a periodically rippled magnetic field (referred to as the wiggler field) to induce an oscillatory motion in the electron beam. The interaction between the transverse component of the oscillatory motion and the radiation field results in an axial bunching of the electron beam which is the source of the instability. This axial-bunching mechanism can be thought of as the result of the ponderomotive potential formed by the beating of the wiggler and radiation fields. The precise form for the wiggler field can take a variety of configurations, and ubitrons and FEL's have

been constructed using both helically^{2-8,10-12,14,15} and linearly^{1,9,13,16-21} polarized wiggler fields. In addition, a wiggler configuration has been proposed which makes use of a rotating quadrupole design.²²

The motivation for the present work is to develop a nonlinear theory and simulation code for a ubitron or FEL amplifier based upon a linearly polarized wiggler field. The advantage of a planar wiggler design over that of a helical configuration is ease of construction and modification. Linearly polarized wigglers are readily constructed from permanent magnet arrays which can be easily adjusted to a tapered wiggler configuration. In this paper we derive a fully three-dimensional nonlinear analysis of the FEL and the ubitron for the planar wiggler configuration. The analysis follows that described previously for a helical wiggler configuration,²³⁻²⁷ and involves the derivation of a set of coupled nonlinear differential equations which self-consistently describe the evolution of both an ensemble of electrons and the electromagnetic fields in a rectangular waveguide. Space-charge fields are neglected in the analysis; therefore, the treatment is applicable to the high-gain Compton (or strong-pump) regime. The nonlinear current which mediates the interaction is computed from the microscopic behavior of the electrons by means of an average of the electron phases relative to the ponderomotive wave formed by the beating of the wiggler and radiation fields. The detailed wiggler

model we employ includes the effect of parabolically tapered pole pieces in order to provide for electron focusing in the plane of the bulk wiggler motion. Further, the injection of the electron beam into the wiggler field is modeled by allowing the wiggler amplitude to increase adiabatically from zero to a constant level. The procedure used also permits the inclusion of an arbitrary taper of the wiggler amplitude for the purpose of the enhancement of the interaction efficiency. The overlap between the electron beam and the transverse mode structure of the TE and TM modes is included in a self-consistent manner, so that no arbitrary "filling factor" need be included in the analysis. Since the problem of interest is that of a FEL or ubitron amplifier, only single-frequency propagation is considered. This permits an average over a wave period to be performed which eliminates the fast-time-scale phenomena from the formulation, and results in a great increase in computational efficiency over a full-scale particle-in-cell simulation.

In organization of this paper is as follows. The general equations are derived in Sec. II. The numerical solution to the dynamical equations is given in Sec. IV, in which a particular example is treated in depth which corresponds to a recent experiment by Orzechowski and co-workers.¹³ Three distinct waveguide modes are found to grow in simulation, and we consider each of these modes in detail including the bandwidths and relative growth rates and saturation efficiencies. Also considered are the effects of

(1) variations in the length of the entry region on the saturation efficiency, (2) an initial momentum spread in the electron beam (i.e., prior to the injection into the wiggler), (3) the scaling of the efficiency with beam current, and (4) the enhancement of the interaction efficiency through a linearly tapered wiggler amplitude. These issues are treated in an abstract manner in Sec. III because the analysis does not correspond to all aspects of the experimental configuration. However, a comparison between the simulation and the experiment is made in Sec. IV in which we give a summary and discussion.

II. GENERAL FORMULATION

The configuration we consider is that of a relativistic electron beam propagating through a loss-free rectangular waveguide in the presence of a linearly polarized wiggler magnetic field. The wiggler-field model that we employ is that encountered when the individual magnets in the wiggler have parabolically tapered pole faces, which provides for electron-beam focusing in the plane of the principal wiggler motion. This technique was first employed experimentally by Phillips.¹ A detailed analysis of the magnetic field produced by a wiggler with parabolically tapered pole pieces was undertaken by Scharlemann,¹⁸ who showed that the wiggler field is of the form

$$\mathbf{B}_w(\mathbf{x}) = B_w \left\{ \cos(k_w z) \left[\sinh \left[\frac{k_w x}{\sqrt{2}} \right] \sinh \left[\frac{k_w y}{\sqrt{2}} \right] \hat{e}_x + \cosh \left[\frac{k_w x}{\sqrt{2}} \right] \cosh \left[\frac{k_w y}{\sqrt{2}} \right] \hat{e}_y \right] - \sqrt{2} \cosh \left[\frac{k_w x}{\sqrt{2}} \right] \sinh \left[\frac{k_w y}{\sqrt{2}} \right] \sin(k_w z) \hat{e}_z \right\}, \quad (1)$$

where B_w denotes the wiggler amplitude, and $k_w (\equiv 2\pi/\lambda_w)$ is the wiggler wave number. We model the injection of the electron beam into the wiggler by allowing the wiggler amplitude to increase adiabatically from zero to a constant level over N_w wiggler periods. In addition, since we intend to study efficiency enhancement by means of a tapered wiggler, the wiggler amplitude will be tapered starting at some point z_0 downstream from the entry region in a linear fashion. To this end, we choose

$$B_w(z) = \begin{cases} B_w \sin^4(k_w z / 4N_w), & 0 \leq z \leq N_w \lambda_w \\ B_w, & N_w \lambda_w < z \leq z_0 \\ B_w [1 + \epsilon_w k_w (z - z_0)], & z > z_0 \end{cases} \quad (2)$$

where

$$\epsilon_w \equiv \frac{1}{k_w} \frac{d}{dz} \ln B_w \quad (3)$$

describes the slope of the taper. Since the fringing fields associated with the tapered wiggler amplitude are neglected, this representation is strictly valid only if the slope of the taper is small. Within the entry region this implies that N_w must be large, while for $z > z_0$ we must require

that $|\epsilon_w| \ll 1$.

The boundary conditions at the waveguide wall may be satisfied by expanding the vector potential in terms of the orthogonal basis functions of the vacuum waveguide. Thus, we write the vector potential of the radiation in the form

$$\delta \mathbf{A}(\mathbf{x}, t) = \sum_{l, n=0}^{\infty} \delta A_{ln}(z) \mathbf{e}_{ln}^{(1)}(x, y) \cos \alpha \quad (4)$$

for the TE modes, and

$$\delta \mathbf{A}(\mathbf{x}, t) = \sum_{l, n=1}^{\infty} \delta A_{ln}(z) \left[\mathbf{e}_{ln}^{(2)}(x, y) \cos \alpha + \frac{k_{ln}}{k} \sin \left[\frac{l\pi X}{a} \right] \times \sin \left[\frac{n\pi Y}{b} \right] \sin \alpha \hat{e}_z \right] \quad (5)$$

for the TM modes, where for frequency ω and wave number $k(z)$,

$$\alpha \equiv \int_0^z dz' k'(z') - \omega t. \quad (6)$$

In addition, \sum' indicates that l and n are not both zero, and

$$\mathbf{e}_{\text{in}}^{(1)}(x, y) \equiv \frac{n\pi}{k_{\text{in}}b} \cos\left[\frac{l\pi X}{a}\right] \sin\left[\frac{n\pi Y}{b}\right] \hat{\mathbf{e}}_x - \frac{l\pi}{k_{\text{in}}a} \sin\left[\frac{l\pi X}{a}\right] \cos\left[\frac{n\pi Y}{b}\right] \hat{\mathbf{e}}_y, \quad (7)$$

$$\mathbf{e}_{\text{in}}^{(2)}(x, y) \equiv \frac{l\pi}{k_{\text{in}}a} \cos\left[\frac{l\pi X}{a}\right] \sin\left[\frac{n\pi Y}{b}\right] \hat{\mathbf{e}}_x + \frac{n\pi}{k_{\text{in}}b} \sin\left[\frac{l\pi X}{a}\right] \cos\left[\frac{n\pi Y}{b}\right] \hat{\mathbf{e}}_y \quad (8)$$

are the polarization vectors. In this representation the waveguide is assumed to be centered at the origin and bounded by $-a/2 \leq x \leq a/2$ and $-b/2 \leq y \leq b/2$. As a consequence, $X \equiv x + a/2$, $Y \equiv y + b/2$, and

$$k_{\text{in}} \equiv \pi \left[\frac{l^2}{a^2} + \frac{n^2}{b^2} \right]^{1/2} \quad (9)$$

denotes the cutoff wave vector. It is implicitly assumed

$$\delta \mathbf{J}(\mathbf{x}, t) = -en_b \int d\mathbf{p}_0 v_{z0} F_0(\mathbf{p}) \int_{A_g} dx_0 dy_0 \sigma_1(x_0, y_0) \int_{-T/2}^{T/2} dt_0 \sigma_1(t_0) \mathbf{v}(z; \mathbf{p}_0, x_0, y_0, t_0) \times \delta[\mathbf{x}_1 - \mathbf{x}_1(z; \mathbf{p}_0, x_0, y_0, t_0)] \frac{\delta[t - \tau(z; \mathbf{p}_0, x_0, y_0, t_0)]}{|v_z(z; \mathbf{p}_0, x_0, y_0, t_0)|}, \quad (12)$$

where v_{z0} is the initial axial velocity, $A_g \equiv ab$ is the area of the waveguide, $T \equiv L / \langle v_{z0} \rangle$, and $\sigma_1(x_0, y_0)$, $\sigma_1(t_0)$, and $F_0(\mathbf{p}_0)$ describe the distributions of the initial conditions subject to the normalizations (A_b is the cross sectional area of the beam)

$$\int_{A_g} dx_0 dy_0 \sigma_1(x_0, y_0) = A_b, \quad (13)$$

$$\int_{-T/2}^{T/2} dt_0 \sigma_1(t_0) = T, \quad (14)$$

and

$$\int d\mathbf{p}_0 F_0(\mathbf{p}_0) = 1. \quad (15)$$

Substitution of the microscopic fields and the source current into Maxwell's equations yields the equations which govern the evolution of the radiation amplitude and wave number. The procedure is formally identical to that described previously for the helical wiggler, cylindrical waveguide configuration,²³ and involves a modal orthogonalization in the transverse coordinates. In addition, a quasistatic assumption is made in the sense that particles which enter the interaction region at times t_0 separated by integral multiples of a wave period are assumed to execute identical trajectories. As a result, $\mathbf{v}(z; \mathbf{p}_0, x_0, y_0, t_0 + 2\pi N/\omega) = \mathbf{v}(z; \mathbf{p}_0, x_0, y_0, t_0)$ for the integer N , and a time average over a wave period can be performed which

that both $\delta A_{\text{in}}(z)$ and $k(z)$ vary slowly over a wave period.

The microscopic source current can be written as the following sum over individual particle trajectories:

$$\delta \mathbf{J}(\mathbf{x}, t) = -e \sum_{i=1}^{N_T} \mathbf{v}_i(z; \mathbf{p}_{i0}, x_{i0}, y_{i0}, t_{i0}) \times \delta[\mathbf{x}_1 - \mathbf{x}_{1i}(z; \mathbf{p}_{i0}, x_{i0}, y_{i0}, t_{i0})] \times \frac{\delta[t - \tau_i(z; \mathbf{p}_{i0}, x_{i0}, y_{i0}, t_{i0})]}{|v_{zi}(z; \mathbf{p}_{i0}, x_{i0}, y_{i0}, t_{i0})|}, \quad (10)$$

where L is the length of the interaction region, N_T is the total number of electrons, n_b is the average electron density, $\mathbf{v}_i(z; \mathbf{p}_{i0}, x_{i0}, y_{i0}, t_{i0})$ is the velocity of the i th electron at position z which entered the interaction region (i.e., crossed the $z=0$ plane) at time t_{i0} and transverse position (x_{i0}, y_{i0}) with momentum \mathbf{p}_{i0} , and

$$\tau_i(z; \mathbf{p}_{i0}, x_{i0}, y_{i0}, t_{i0}) \equiv t_{i0} + \int_0^z \frac{dz'}{v_{zi}(z'; \mathbf{p}_{i0}, x_{i0}, y_{i0}, t_{i0})}. \quad (11)$$

This discrete sum over particles can be replaced by an integration over the initial conditions, and we write

permits consideration of a single "beamlet" that includes electrons which enter the interaction region within one ponderomotive (or wave) period.²⁹ This greatly improves the computational efficiency. It should be remarked that the ponderomotive phase of each particle is followed self-consistently in the analysis, so that while the beamlet is initially distributed over one ponderomotive wave, the final state may describe an electron distribution which has become trapped within several ponderomotive buckets. In view of this, the equations which govern the evolution of the TE_{in} mode are

$$\frac{d^2}{dz^2} \delta a_{\text{in}} + \left[\frac{\omega^2}{c^2} - k^2 - k_{\text{in}}^2 \right] \delta a_{\text{in}} = 8 \frac{\omega_b^2}{c^2} F_{\text{in}} \left\langle \frac{\cos \alpha}{|v_z|} \mathbf{e}_{\text{in}}^{(1)} \cdot \mathbf{v} \right\rangle, \quad (16)$$

and

$$2k^{1/2} \frac{d}{dz} (k^{1/2} \delta a_{\text{in}}) = -8 \frac{\omega_b^2}{c^2} F_{\text{in}} \left\langle \frac{\sin \alpha}{|v_z|} \mathbf{e}_{\text{in}}^{(1)} \cdot \mathbf{v} \right\rangle, \quad (17)$$

where $\delta a_{\text{in}} \equiv e \delta A_{\text{in}} / mc^2$, $\omega_b^2 \equiv 4\pi e^2 n_b / m$, \mathbf{v} is the instantaneous velocity, and $F_{\text{in}} \equiv \frac{1}{2}$ when either $l=0$ or $n=0$ and unity otherwise. For the TM_{in} mode we obtain a similar result,

$$\frac{d^2}{dz^2} \delta a_{lm} \left[1 + \frac{k_{lm}^2}{k^2} \right] \left[\frac{\omega^2}{c^2} - k^2 - k_{lm}^2 \right] \delta a_{lm} = 8 \frac{\omega_b^2}{c^2} \left\langle \frac{\cos \alpha}{|v_z|} e_{lm}^{\pm} \cdot \mathbf{v} + \frac{v_z}{|v_z|} \frac{k_{lm}}{k} \sin \left[\frac{l\pi X}{a} \right] \sin \left[\frac{n\pi Y}{b} \right] \sin \alpha \right\rangle, \quad (18)$$

and

$$2 \left[k + \frac{k_{lm}^2}{k} \right] \frac{d}{dz} \left[k + \frac{k_{lm}^2}{k} \right] \delta a_{lm} = -8 \frac{\omega_b^2}{c^2} \left\langle \frac{\sin \alpha}{|v_z|} e_{lm}^{\pm} \cdot \mathbf{v} - \frac{v_z}{|v_z|} \frac{k_{lm}}{k} \sin \left[\frac{l\pi X}{a} \right] \sin \left[\frac{n\pi Y}{b} \right] \cos \alpha \right\rangle. \quad (19)$$

Observe that there is no nontrivial TM mode solution when either $l=0$ or $n=0$.

The averaging operator $\langle \dots \rangle$ is defined over the initial conditions of the beam (note that the instantaneous positions and momenta of the electrons are implicit functions of the initial conditions) and includes the effect of an initial momentum spread by means of the distribution function

$$F_0(\mathbf{p}_0) = A \exp[-(p_{z0} - p_0)^2 / \Delta p_z^2] \delta(p_\perp^2 - p_{\perp 0}^2) H(p_{z0}), \quad (20)$$

where p_0 and Δp_z describe the initial bulk momentum and momentum spread of the beam, $H(x)$ is the Heaviside function, and the normalization constant is

$$A \equiv \left[\pi \int_0^{p_0} dp_{z0} \exp[-(p_{z0} - p_0)^2 / \Delta p_z^2] \right]^{-1}. \quad (21)$$

Observe that the distribution is *monoenergetic*, but contains a pitch angle spread which describes an *axial energy spread* (as well as a transverse energy spread) given approximately by

$$\frac{\Delta \gamma_z}{\gamma_0} \approx 1 - \left[1 + 2(\gamma_0^2 - 1) \frac{\Delta p_z}{p_0} \right]^{-1/2}, \quad (22)$$

where $\gamma_0 \equiv (1 - p_0^2/m^2c^2)^{-1/2}$. There is no fundamental difficulty in the inclusion of an overall energy spread in the analysis; however, the additional degree of freedom requires an increased number of particles in the simulation. The δ function allows us to perform one of the momentum-space integrals analytically, and to write the averaging operator in the form

$$\langle \dots \rangle \equiv \frac{A}{2\pi ab} \int_0^{2\pi} d\phi_0 \int_0^{p_0} dp_{z0} \beta_{z0} \exp[-(p_{z0} - p_0)^2 / \Delta p_z^2] \int_{-\pi}^{\pi} d\psi_0 \int_{-\pi/2}^{\pi/2} dx_0 \int_{-\pi/2}^{\pi/2} dy_0 \sigma_{\perp}(x_0, y_0) \dots, \quad (23)$$

where $\psi_0 (\equiv -\omega t_0)$ is the initial ponderomotive phase, $\phi_0 \equiv \tan^{-1}(p_{y0}/p_{x0})$, and $\beta_{z0} \equiv v_{z0}/c$. It is important to recognize that this average includes the effect of the overlap between the electron beam and the transverse mode structure of the radiation field in a self-consistent way.

The phase variation of each mode can be analyzed by the addition of an equation to integrate the relative phase

$$\Phi(z) \equiv \int_c^z dz' [k(z') - k_0], \quad (24)$$

where $k_0 \equiv (\omega^2/c^2 - k_{lm}^2)^{1/2}$ is the wave number of the vacuum guide. Since the departure of $k(z)$ from the vacuum wave number describes the effect of the wave-particle interaction, $\Phi(z)$ represents a measure of the dielectric effect of the FEL interaction. Thus, we integrate the additional equation

$$\frac{d}{dz} \Phi = k - k_0, \quad (25)$$

for both the TE and TM modes.

In order to complete the formulation, the electron-orbit equations must also be specified. Since we describe an amplifier model, we choose to integrate in z and write the Lorentz force equations in the form

$$m \frac{d}{dz} \mathbf{p} = -e \delta \mathbf{E}_{lm} - \frac{e}{c} \mathbf{v} \times (\mathbf{B}_w + \delta \mathbf{B}_{lm}), \quad (26)$$

where \mathbf{B}_w is given by Eqs. (1) and (2) and the radiation fields are given by the vector potentials

$$\delta \mathbf{E}_{lm} = -\frac{1}{c} \frac{\partial}{\partial t} \delta \mathbf{A}_{lm}, \quad \delta \mathbf{B}_{lm} = \nabla \times \delta \mathbf{A}_{lm}. \quad (27)$$

Finally, the electron coordinates obey the equations

$$v_z \frac{d}{dz} x = v_x, \quad (28)$$

$$v_z \frac{d}{dz} y = v_y, \quad (29)$$

and

$$\frac{d}{dz} \psi = k + k_w - \frac{\omega}{v_z} \quad (30)$$

describes the evolution of ponderomotive phase

$$\psi = \psi_0 + \int_0^z dz' \left[k + k_w - \frac{\omega}{v_z} \right], \quad (31)$$

III. NUMERICAL ANALYSIS

The set of coupled differential equations described in Sec. II is solved for an amplifier configuration in which a single mode of frequency ω is injected into the system at

$z=0$. The dynamical equations [Eqs. (16)–(19) and (25)] for the fields can be reduced to a set of four first-order ordinary differential equations for δa_{in} , $\Gamma_{in}[\equiv k_{in}^{-1}d(\ln\delta a_{in})/dz]$, k , and the relative phase Φ . Hence, the numerical resolution of the problem consists in the simultaneous solution of $6N_T+4$ first-order ordinary differential equations, where N_T is the number of electrons. The algorithm we employ is the fourth-order Runge-Kutta-Gill technique. While this technique is somewhat less stable than the fourth-order Adams-Moulton predictor-corrector scheme, it has the advantage of being less memory intensive. Indeed, the requirements placed on the available size of computer memories represents a critical practical limitation when momentum spread is included. The averages in Eqs. (16)–(19) are performed by means of an N th-order Gaussian quadrature technique in each of the variables $(x_0, y_0, \psi_0, p_{z0}, \phi_0)$.

The initial conditions on the radiation field are chosen such that $\Gamma_{in}(z=0)=0$, $k(z=0)=k_0$, and $\Phi(z=0)=0$ for an arbitrary initial power level. Observe that the time-averaged Poynting flux P_{in} for the waveguide modes is related to the field amplitude by the relation

$$P_{in} = \frac{m^2 c^4}{32e^2} \frac{ab}{\pi F_{in}} \omega k \delta a_{in}^2 \quad (32)$$

for the TE_{in} mode, and

$$P_{in} = \frac{m^2 c^4}{32e^2} \frac{ab}{\pi} \omega \left[k + \frac{k_{in}^2}{k} \right] \delta a_{in}^2 \quad (33)$$

for the TM_{in} mode. The initial state of the electron beam is chosen to model the injection of a continuous, axisymmetric electron beam with a uniform cross section; hence, we choose $\sigma = 1$ for $-\pi \leq \psi_0 \leq \pi$ and $\sigma_z = 1$ for $r_0 \leq R_b$.

The particular example we analyze is that of a 35-GHz amplifier employing an electron beam with an energy of 3.5 MeV, a current of 800 A, and an initial radius of 1.0 cm which propagates through a waveguide characterized by $a=9.8$ cm and $b=2.9$ cm. In order to obtain peak growth rates in the vicinity of 35 GHz we choose a wiggler field with an amplitude of 3.72 kG and a period of 9.8 cm, with an entry taper of $N_w = 5$. For purposes of illustration, the first case we consider is that of a beam with zero momentum spread ($\Delta\gamma_z=0$). For all cases discussed in this work with $\Delta\gamma_z=0$ the choice of a tenth-order Gaussian algorithm in each of the coordinates (ψ_0, r_0, θ_0) was found to provide an accuracy of the order of 0.1%. The initial electron distributions in the axial phase space and beam cross section are shown in Fig. 1. Each dot in the illustration of the axial phase space describes a *phase sheet* composed of 100 electrons distributed throughout the cross section of the electron beam. Each *phase sheet*, therefore, represents a cross-sectional slice of the electron beam, which is chosen initially as shown in Fig. 1(b). Although each phase sheet is initially chosen to be identical, the subsequent evolution of the electron trajectories in the presence of the radiation field is followed self-consistently. It should also be remarked that the distribution shown represents a uniform electron beam. The nonuniformity in the positions of the electrons chosen by means of the

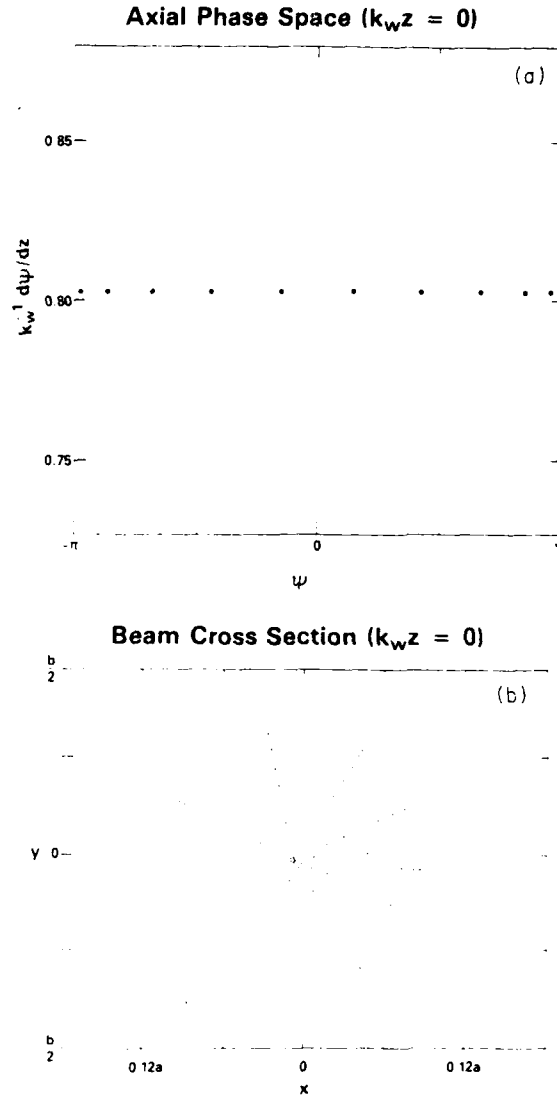


FIG. 1. Initialization of (a) the axial phase space, and (b) the beam cross section. Each point in the axial phase space represents the superposition of 100 particles distributed throughout the cross section of the beam.

Gaussian algorithm is compensated for by a nonuniformity in the weighting of the electrons.

There are three modes which are resonant in the vicinity of 35 GHz; specifically, the TE_{01} , TE_{21} , and TM_{21} modes. The analysis presented in this work deals with wave-particle interactions with single modes, and we shall deal with each of these modes individually. The first mode we treat is the TE_{01} mode which is the lowest-order resonant mode at the frequency of interest. The detailed evolution of the wave power as a function of axial position is shown in Fig. 2 for the injection of a 50-kW signal at a frequency of $\omega/ck_w = 11.3$ (34.6 GHz). As shown in the figure, saturation occurs at $k_w z \approx 115$ (1.79 m) at a power level of approximately 214 MW which corresponds to an efficiency of $\eta \approx 7.75\%$. Wave amplification occurs principally within the uniform

wiggler region ($z > N_w \lambda_w$) which is 1.30 m for this case and yields an average gain of about 28 dB/m. Although this value for the average gain is lower than that observed in some other experiments (a gain of approximately 120 dB/m has been observed by Gold and co-workers³), the average normalized growth rate $\Gamma_{01}/k_w \approx 0.05$ is quite high and is attributable to the relatively high wiggler amplitude and long wiggler period.

One feature of interest shown in Fig. 2 which merits some discussion is the oscillation in the instantaneous power which occurs with a period of $\lambda_w/2$. This is not found for the case of helical wiggler configurations for which the bulk transverse wiggler motion describes a helix with a transverse velocity of relatively constant magnitude. In contrast, a linearly polarized wiggler will induce a bulk wiggler motion in the plane normal to that of the wiggler field characterized by an oscillatory velocity. In order to illustrate this qualitatively, we observe that for the present configuration the bulk transverse wiggler motion is aligned along the x axis and varies approximately as

$$v_x = \frac{\Omega_w}{\gamma_0 k_w} \sin(k_w z) \hat{e}_x. \quad (34)$$

The source terms contained in the dynamical equations (16)-(19) are derived essentially from a calculation of $(\mathbf{J} \cdot \delta \mathbf{E})$; hence, the principal wave-particle coupling is with the x component of the radiation field. If we assume that $\delta E_x \sim \delta E_x \sin(k_w z - \omega t)$, then it is evident that

$$(\mathbf{J} \cdot \delta \mathbf{E}) \sim -\frac{\Omega_w}{2\gamma_0 k_w} \delta E_x (\cos \psi - \cos(2k_w z - \psi)). \quad (35)$$

The interaction occurs when the ponderomotive phase is a slowly varying function of axial position [i.e., $\omega \approx k - k_w$], and the upper beat wave which varies as $\cos \psi$ describes wave amplification. The lower beat wave describes the oscillation at half the wiggler period. Although the spatial average of the contribution of the lower beat wave vanishes and this term provides no contribution to the bulk growth of the wave, the instantaneous values

of the power are affected. Indeed, the instantaneous variation of the relative phase also exhibits an oscillation at half the wiggler period.

A full spectrum of the TE_{01} mode is shown in Fig. 3 in which we plot the saturation efficiency and distance to saturation as a function of frequency within the unstable band. As shown in the figure, wave amplification is found for frequencies extending from $\omega/ck_w \approx 10$ (30.6 GHz) through $\omega/ck_w \approx 14.2$ (43.5 GHz) with a peak efficiency of the order of approximately 9.8%. The peak growth rate (as measured by the distance to saturation) occurs for $\omega/ck_w \approx 12.3$ (37.7 GHz), which is somewhat higher than the targeted 35 GHz. However, the gain bandwidth is sufficiently broad that the growth rate has not decreased significantly from the peak value.

The variation of the relative phase versus axial position is illustrated in Fig. 4 for $\omega/ck_w = 10.4, 10.7, 11.0, 11.3$, and 11.9. As is evident from the figure, the oscillation at one half the wiggler period is also manifested in the relative phase. The bulk variation (i.e., averaged over a wiggler period) shows the same qualitative behavior as that found for a helical wiggler.²⁶ Specifically, for frequencies at the low end of the gain band the relative phase decreases up to a point just short of the position at which the power saturates (indicated in the figure by an arrow) after which the phase remains relatively constant. As the frequency increases, the variation in the relative phase decreases until a critical frequency is reached ($\omega/ck_w \approx 11$ for the particular case under consideration) for which the phase is found to vary little over the course of the interaction. This critical frequency is typically found to be about

TE₀₁ Mode (a = 9.8 cm; b = 2.9 cm; $\omega/ck_w = 11.3$; P_{in} = 50 kW)

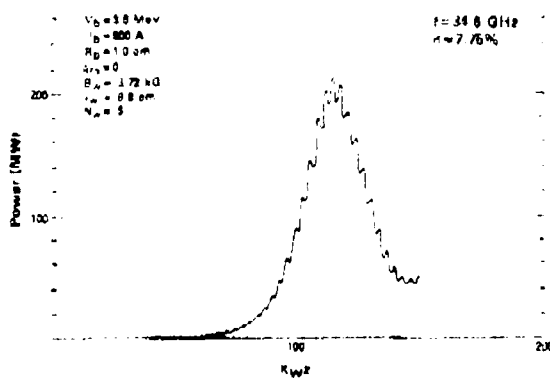


FIG. 2. Plot of the growth of the TE_{01} mode with axial position.

TE₀₁ Mode (a = 9.8 cm; b = 2.9 cm; P_{in} = 50 kW)

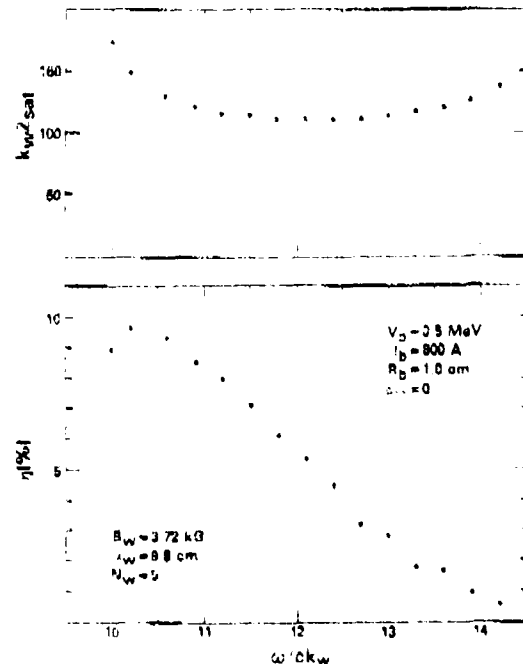


FIG. 3. Graph showing the distance to saturation and the efficiency of the TE_{01} mode as a function of frequency.

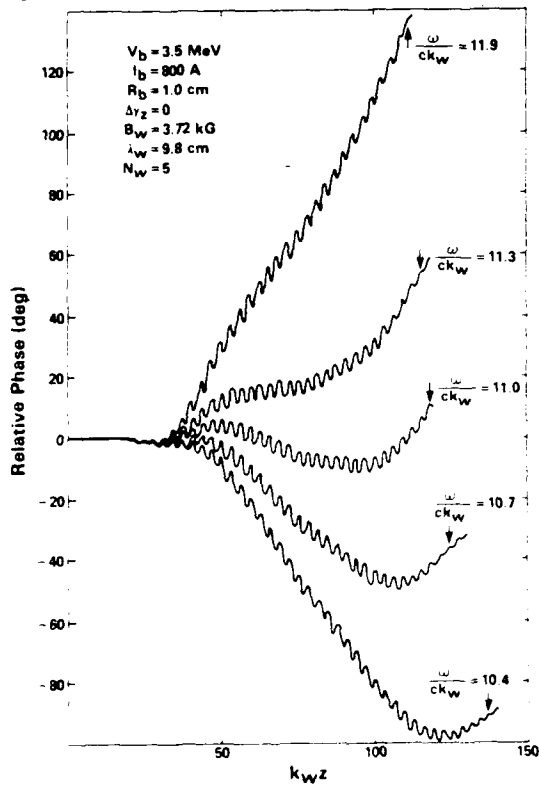
TE₀₁ Mode (a = 9.8 cm; b = 2.9 cm; P_{in} = 50 kW)

FIG. 4. Plot of the relative phase of the TE₀₁ mode vs axial position for $\omega/ck_w = 10.4, 10.7, 11.0, 11.3,$ and 11.9 .

10% below the frequency of peak growth. For frequencies above the critical frequency, the bulk phase increases monotonically. It should be remarked that the gain band under discussion corresponds to the upper frequency intersection between the beam resonance line [$\omega = (k + k_w)v_z$] and the vacuum waveguide dispersion curve. There is also a gain band associated with the lower-frequency intersection which shows a similar variation in the relative phase, except, that there is an inversion in the frequency dependence.²⁶

The question of the effect of the injection process of the electron beam can be addressed by varying the length of the entry taper region. The results of this analysis are shown in Fig. 5 in which we plot the saturation efficiency and the distance to saturation as functions of the length of the entry taper region for $N_w \geq 3$. We have arbitrarily chosen the minimum length of the entry taper region to be three wiggler periods since the fringing fields associated with the tapered wiggler field have been neglected, and we feel that below this value the fringing fields will be important. The results indicate that the saturation efficiency increases markedly as the length of the entry region increases from $3\lambda_w$ to approximately $6\lambda_w$, after which the increase in the efficiency becomes more gradual. We attribute this increase in the efficiency to a decrease in the effective momentum spread induced by the injection of

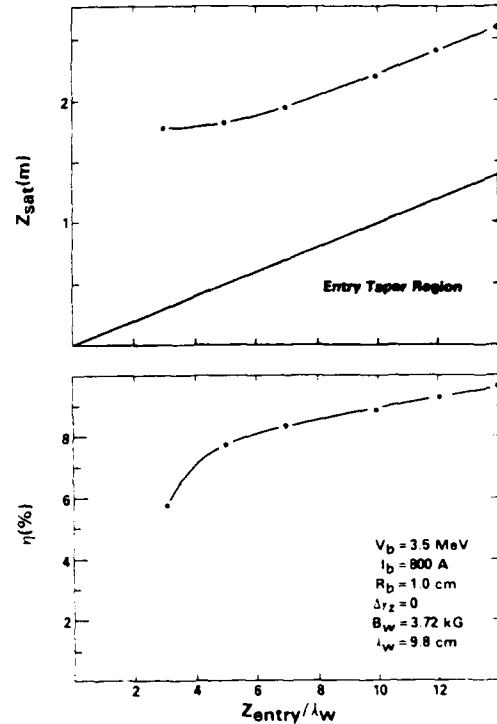
TE₀₁ Mode (a = 9.8 cm; b = 2.9 cm; $\omega/ck_w = 11.3$)

FIG. 5. Plot of the distance to saturation and the efficiency of the TE₀₁ mode as a function of the length of the entry taper region for $\omega/ck_w = 11.3$.

the beam into the increasing wiggler field. It should also be noted that the increase in the distance to saturation is roughly linear for $N_w \geq 5$ and corresponds to the increase in the length of the entry region (i.e., the length of the uniform wiggler region remains relatively constant).

The particle dynamics during the course of the TE₀₁ mode interaction are illustrated in Figs. 6 and 7. In the first place, we remark that saturation proceeds by means of the phase trapping of the beam in the ponderomotive potential. This is shown in Fig. 6 in which we plot the phase-space distribution of the beam at saturation. The dashed line in the figure represents an approximate separatrix calculated for particles at the beam center; hence, many of the electrons which appear outside of the separatrix may instead be on trapped particle orbits at the edge of the beam. The cross-sectional evolution of the beam is shown in Fig. 7. The cross-sectional projection of the beam at the start of the uniform wiggler region (i.e., $k_w z = 31$) is shown in Fig. 7(a). The bulk motion of the beam exhibits four essential features. The first is the primary wiggler-induced oscillatory motion which shifts the center of the beam off axis in the x direction, and this shift is clearly shown in Fig. 7(a). The second feature is that the transverse wiggler gradient introduces a betatron oscillation which causes a macroscopic scalloping of the beam envelope. In addition, on a microscopic level the

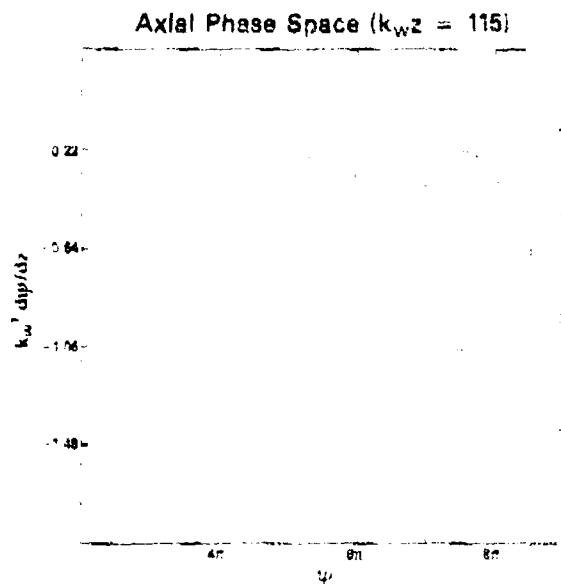


FIG. 6. Plot of the beam distribution in axial phase space at saturation.

individual electrons come into a focus and out again on the opposite side of the beam. This becomes evident in Fig. 7(a) by noticing that the two closely spaced "spokes" are oriented in the negative- x direction while in the initial state [Fig. 1(b)] these same spokes were oriented in the positive- x direction. The third feature is that the transverse wiggler gradient also has a focusing effect on the beam which results in a reduction in the maximum beam radius relative to the initial state. The betatron oscillation occurs over a length of approximately $\Delta z_B \approx 3.08\lambda_w$ (i.e., $k_w \Delta z_B \approx 19.3$), and the evolution of the beam cross section over this distance is shown in Fig. 7 (from $k_w z \approx 31$ –51). Lastly, the geometry of the wiggler and the transverse gradients tends to distort the beam into an elliptical cross section. While this is evident in Fig. 7 at an early stage of the wiggler, it is shown even more dramatically in Fig. 7(b) which shows the cross section at saturation ($k_w z = 115$).

We now consider the TE_{21} mode, and plot the evolution of the wave power versus axial position in Fig. 8 for a 50-kW input signal at $\omega/ck_w = 11.3$ and an electron beam with a zero initial momentum spread. As is evident from the figure, the power saturates at $k_w z \approx 104$ at about 194 MW for an efficiency $\eta \approx 6.85\%$. In comparison with the TE_{01} mode, therefore, we conclude that the average growth rate is somewhat higher and the efficiency lower for the TE_{21} mode at this frequency. A complete spectrum for the TE_{21} mode is shown in Fig. 9 in which we plot the distance to saturation and the efficiency versus frequency. As shown in the figure, gain is found for frequencies ranging from $\omega/ck_w \approx 8.9$ through $\omega/ck_w \approx 14$ with a peak efficiency of approximately 12%. As a result, both the bandwidth and peak efficiency are higher for the TE_{21} mode than for the TE_{01} mode. In addition, while this frequency falls slightly below the frequency of peak

growth rate for the TE_{01} mode, it is close to the frequency of maximum growth rate for the TE_{21} mode.

The evolution of the wave power versus axial position is shown in Fig. 10 for a 50-kW input signal in the TM_{21} mode at $\omega/ck_w = 11.3$ and an electron beam with zero initial momentum spread. As shown in the figure, the power saturates at $k_w z \approx 237$ with approximately 68.5 MW for an efficiency $\eta \approx 2.45\%$. This is a much lower growth rate and efficiency than found for either the TE_{01} or TE_{21} modes, despite the fact that the cutoff frequency and dispersion curves are degenerate for the TM_{21} and TE_{21} modes. The difference between the two modes lies in the transverse mode structure. As mentioned previously, the principal component of the wiggler-induced motion is aligned with the x axis; hence, the wave-particle interaction is governed largely by the x component of the electric field. Comparison of the mode structures for the TE_{21} and TM_{21} modes given by Eqs. (4) and (5) shows that for a given mode amplitude (δA_{21}) the ratio of the x component of the electric field of the TM_{21} to that of the TE_{21} mode is approximately $2b/a \approx 0.59$. As a result, the wave-particle coupling is weaker for the TM_{21} mode. Note that this conclusion would be reversed if the configuration were altered such that the principal component of the wiggler motion were aligned with the y axis. However, one effect arising from the degeneracy of the dispersion curves is that the frequency of interest ($\omega/ck_w = 11.3$) lies near to peak growth for both TE_{21} and TM_{21} modes. This is shown clearly in Fig. 11 in which we plot the distance to saturation and the saturation efficiency as a function of frequency for the TM_{21} mode. As might be expected, the reduced wave-particle coupling and growth rates for the TM_{21} mode result in a narrower bandwidth for instability, and we obtain wave growth for frequencies ranging from $\omega/ck_w \approx 10.2$ –12.

The question of the variation in the phase of FEL amplifiers has important implications for many of the potential applications of these devices. Since high powers and efficiencies have been demonstrated experimentally,¹³ one such application may be as a high-power microwave source for the next generation of radio-frequency electron accelerators. However, one requirement for such an application is good phase stability of the output radiation against fluctuations in the electron-beam voltage. Examination of Fig. 4 shows that the relative phase at saturation varies rapidly with frequency. Since there is a correspondence between variations in the frequency at fixed voltage and variations in the voltage at fixed frequency, we might expect the phase at saturation to vary rapidly with beam voltage. This is indeed the case as shown in Fig. 12, in which we plot the relative phase at a fixed axial position (chosen to correspond to the saturation point for a beam voltage of 3.5 MeV) versus beam voltage for the TE_{01} , TE_{21} , and TM_{21} modes. The variation in the relative phase is approximately $51^\circ/1\%$ variation in the beam voltage for the TE_{01} mode, $43^\circ/1\%$ variation in the beam voltage for the TE_{21} mode, and $89^\circ/1\%$ variation in the beam voltage for the TM_{21} mode. Such rapid variations in the phase are consistent with results obtained previously for

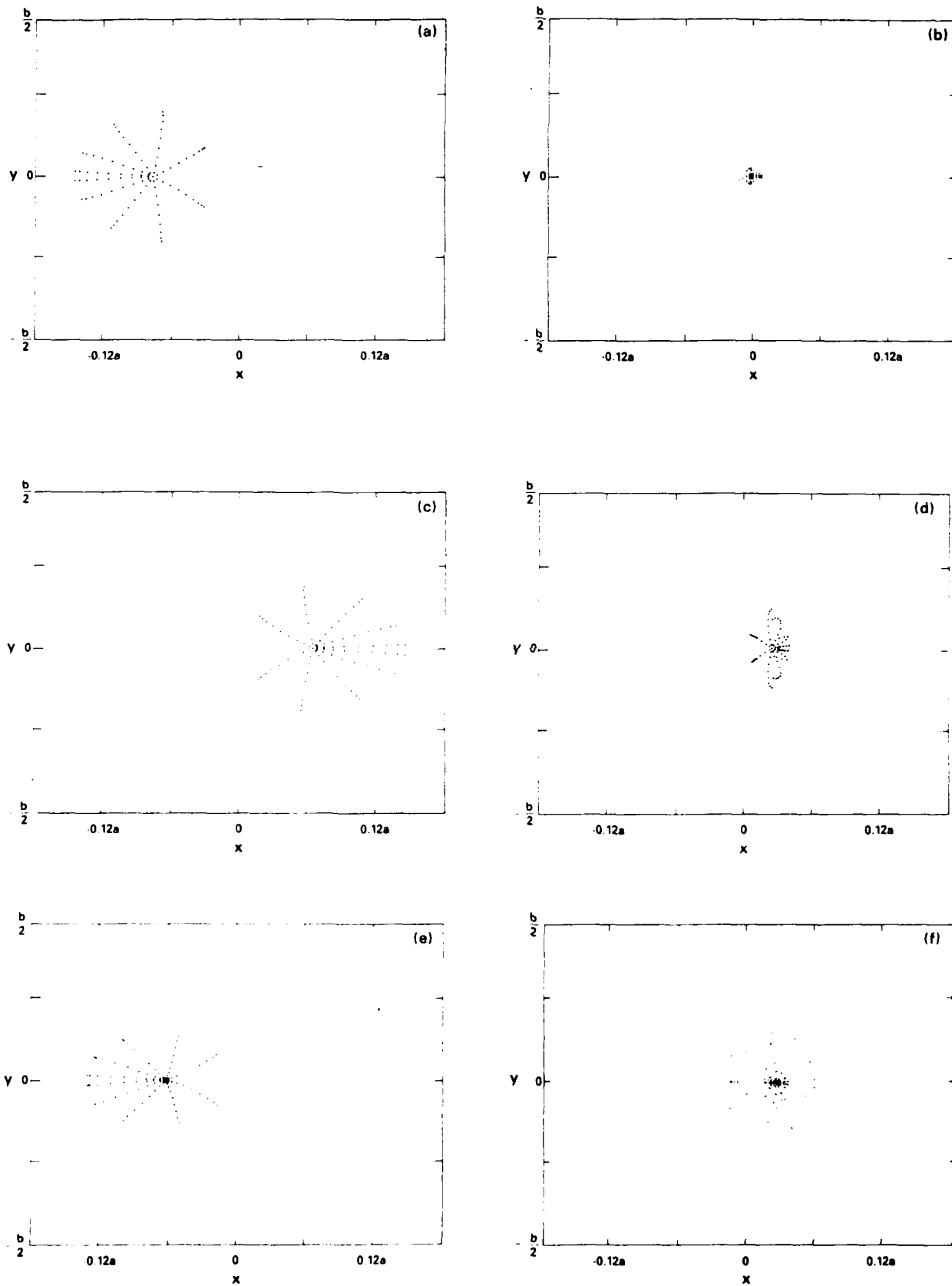


FIG. 7. Plot of the beam cross section at (a) the end of the entry taper region ($k_w z = 31$), (b) $k_w z = 36$, (c) $k_w z = 41$, (d) $k_w z = 46$, (e) $k_w z = 51$, and (f) $k_w z = 115$.

TE₂₁ Mode (a = 5.8 cm; b = 2.9 cm; $\omega/ck_w = 11.3$; P_{in} = 50 kW)

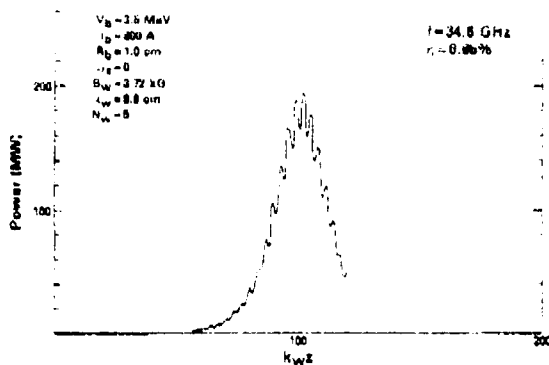


FIG. 8. Plot of the growth of the TE₂₁ mode with axial position

TM₂₁ Mode (a = 9.8 cm; b = 2.9 cm; $\omega/ck_w = 11.3$; P_{in} = 50 kW)

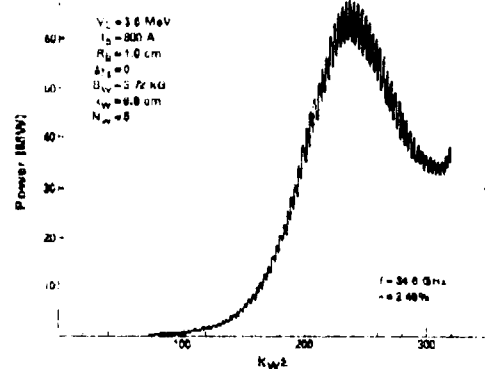


FIG. 10. Plot of the growth of the TM₂₁ mode with axial position.

a helical wiggler, cylindrical waveguide configuration,²⁵ and contrasts with 8%/1% variation in beam voltage for a typical Stanford Linear Accelerator (SLAC) klystron.³⁰ We conclude, therefore, that applications which require an extremely phase-stable microwave source will also require an electron-beam source with a very low level of voltage fluctuations.

The effect of an initial momentum spread is shown in Fig. 13 in which we plot the efficiency versus $\Delta\gamma_z/\gamma_0$ for the TE₀₁, TE₂₁, and TM₂₁ modes. From the beam-

resonance condition, it is apparent that the transition to a thermally dominated regime occurs when $\Delta v_z/v_0 \sim \Gamma_{in}/(k+k_0)$. Making use of Eq. (22) we find that this transition occurs at about $\Delta\gamma_z/\gamma_0 \approx 18\%$ for the TE₀₁ and TE₂₁ modes, and $\Delta\gamma_z/\gamma_0 \approx 8\%$ for the TM₂₁ mode. As a consequence, the cases shown in Fig. 19 are well short of the thermal-beam regime. The efficiency is found to decrease in an approximately linear fashion with increasing $\Delta\gamma_z$ for each of these modes, which corresponds with results ob-

TE₂₁ Mode (a = 9.8 cm; b = 2.9 cm; P_{in} = 50 kW)

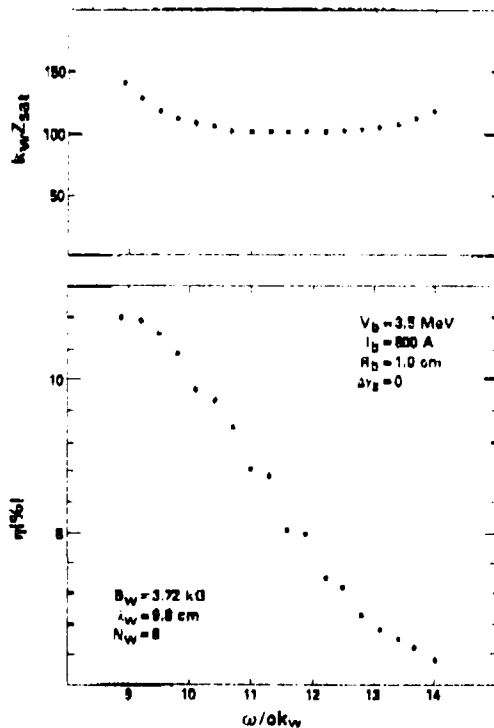


FIG. 9. Graph showing the distance to saturation and the efficiency of the TE₂₁ mode as a function of frequency.

TM₂₁ Mode (a = 9.8 cm; b = 2.9 cm; P_{in} = 50 kW)

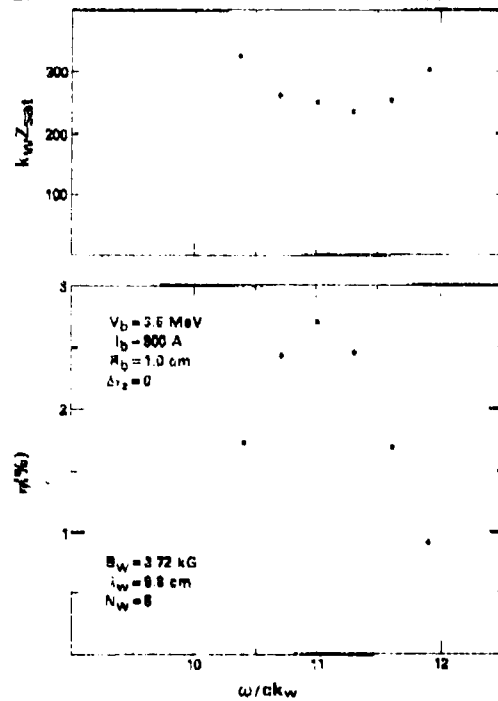


FIG. 11. Graph showing the distance to saturation and the efficiency of the TM₂₁ mode as a function of frequency.

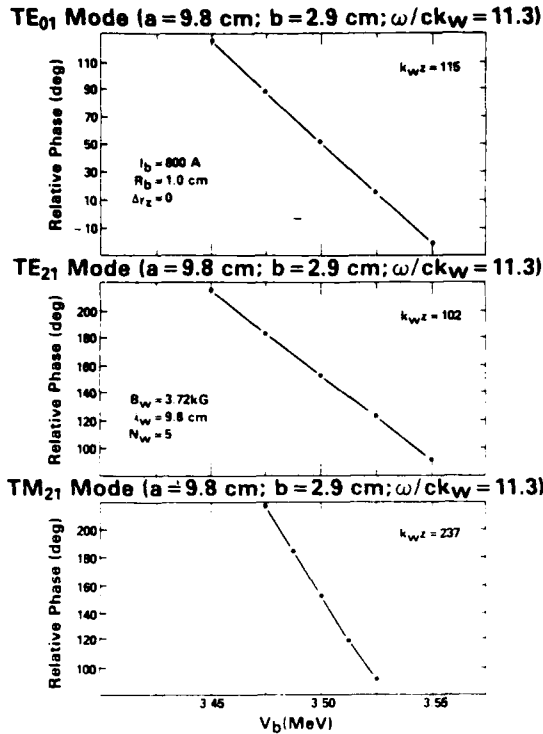


FIG. 12. Graph showing the variation in the relative phase at saturation (for $V_b = 3.5$ MeV) vs beam voltage.

tained for a helical wiggler configuration.²⁵ Note, however that the present results were obtained with the same model distribution (20) as for the helical wiggler, and the detailed variation in the efficiency with momentum spread can be expected to vary with the choice of distribution. Be that as it may, we find that the efficiency drops from $\eta \approx 7.75\%$ to $\eta \approx 4.98\%$ for the TE₀₁ mode as $\Delta\gamma_z/\gamma_0$ increases to about 2.3%. For the TE₂₁ mode, the efficiency drops from $\eta \approx 6.85\%$ to $\eta \approx 3.76\%$ as $\Delta\gamma_z/\gamma_0$ increases to 2.3%. The efficiency of the TM₂₁ mode decreases from $\eta \approx 2.45\%$ to $\eta \approx 1.27\%$ as $\Delta\gamma_z/\gamma_0$ increases to 1%. This is more rapid than for the TE₀₁ and TE₂₁ modes, and occurs because the transition to the thermal-beam regime is found for a lower value of the momentum spread for the TM₂₁ mode.

The scaling of the saturation efficiency with beam current for the TE₀₁, TE₂₁, and TM₂₁ modes is shown in Figs. 14–16, respectively, for $\Delta\gamma_z = 0$ and $\Delta\gamma_z/\gamma_0 = 1\%$. On the basis of an idealized one-dimensional model,²⁹ it has been shown that the saturation efficiency should scale as $\eta \sim I_b^{1/3}$ for frequencies corresponding to peak growth rates. As shown in Fig. 14, this type of scaling law is obtained for the TE₀₁ mode over a range of currents extending from approximately 300–1000 A. Observe that the dielectric effect of the electron beam on the waveguide mode is included in the formulation, and the bandwidth of the interaction shifts with the beam current. As a consequence, the increasing divergence between the simulation results and the scaling law for currents below 300 A is attributed to a shift in the frequency of peak growth away from $\omega/ck_w \approx 11.3$. It should also be noted that the curve for $\Delta\gamma_z/\gamma_0 = 1\%$ increases with current only slightly faster than that obtained for $\Delta\gamma_z = 0$ and, other parameters being equal, the $I_b^{1/3}$ scaling law seems to be relatively in-

a = 9.8 cm; b = 2.9 cm; $\omega/ck_w = 11.3$; $P_{in} = 50$ kW

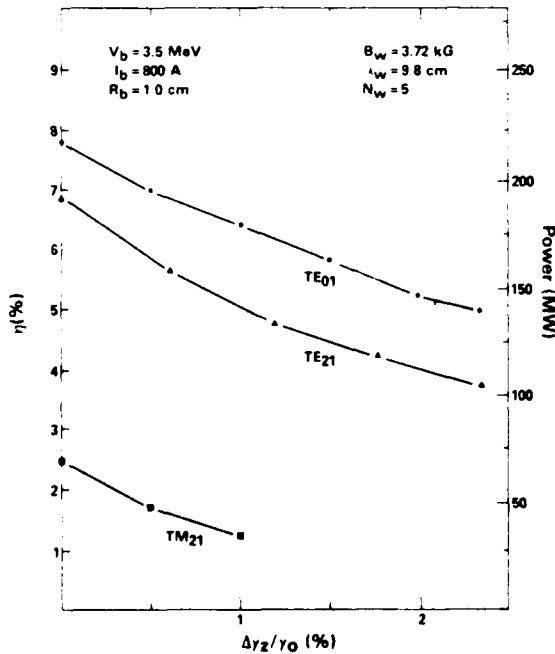


FIG. 13. Plot of the saturation efficiencies of the TE₀₁, TE₂₁, and TM₂₁ modes vs axial energy spread for $\omega/ck_w = 11.3$.

TE₀₁ Mode (a = 9.8 cm; b = 2.9 cm; $\omega/ck_w = 11.3$; $P_{in} = 50$ kW)

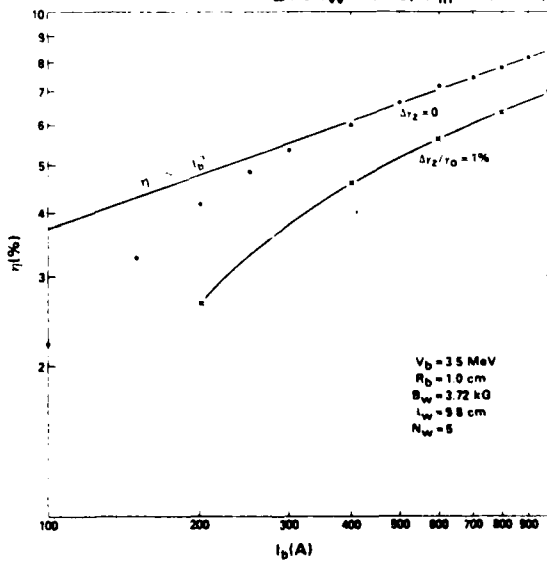


FIG. 14. Graph of the saturation efficiency of the TE₀₁ mode vs beam current for $\omega/ck_w = 11.3$.

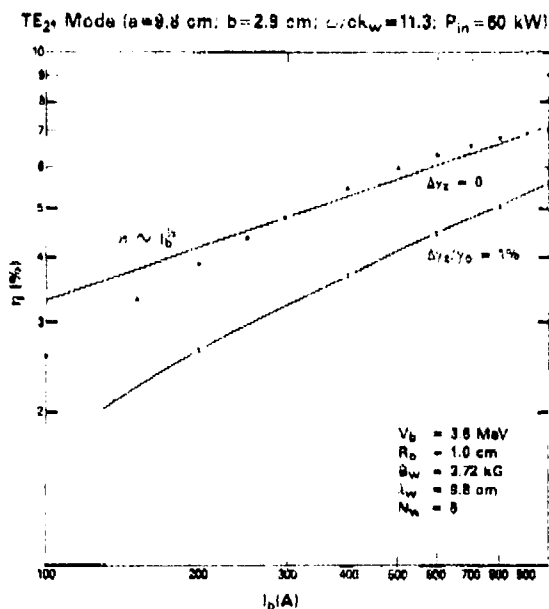


FIG. 15. Graph of the saturation efficiency of the TE_{21} mode vs beam current for $\omega/ck_w = 11.3$.

dependent of the momentum spread. However, one point of caution is worth noting in regard to these conclusions. Specifically, if the variation in current were accompanied by variations in the momentum spread and/or beam radius (as might be expected if the beam were held at constant brightness), then the scaling law might differ. The $I_b^{1/3}$ scaling law is also approximately found for the TE_{21}

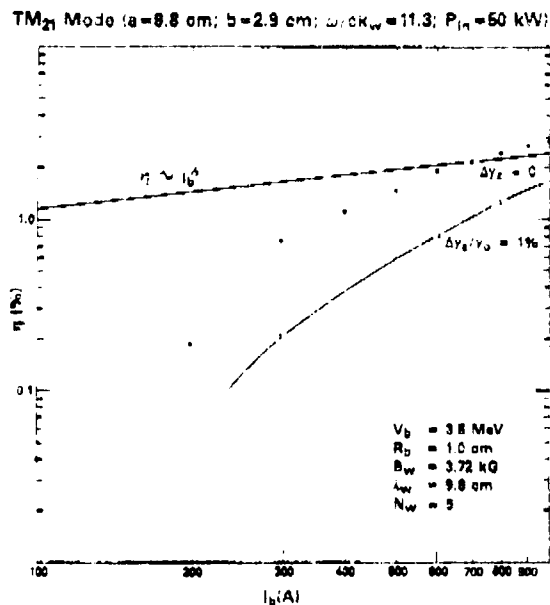


FIG. 16. Graph of the saturation efficiency of the TM_{21} mode vs beam current for $\omega/ck_w = 11.3$.

mode for currents ranging from about 200–1000 A. The slightly larger range of currents over which the scaling law seems to hold for the TE_{21} mode is attributed to the previously mentioned result that $\omega/ck_w = 11.3$ is closer to the frequency of peak growth rate for this mode than for the TE_{01} mode. As a consequence, this frequency remains in the vicinity of the maximum growth rate over a broader range of currents for the TE_{21} mode. Although the expected scaling law is approximately obtained for the TE_{01} and TE_{21} modes, three-dimensional effects involved in the beam propagation and the coupling between the beam and the transverse mode structure do modify the scaling. This is most evident for the TM_{21} mode shown in Fig. 16 for which we find the efficiency increasing somewhat faster than $I_b^{1/3}$.

We now address the issue of efficiency enhancement by means of a tapered wiggler field, and concentrate on the TE_{01} mode. The fundamental theory of the efficiency enhancement mechanism has been amply discussed in the literature.^{31–38} In order to understand the physical basis of the process, we observe that the wave-particle resonance condition which gives rise to amplification is extremely sensitive to the axial electron velocity. However, the axial velocity decreases as the wave is amplified until, ultimately, the resonance condition is broken and the amplification ceases. The purpose of the tapered wiggler field is to reduce the transverse velocity induced by the wiggler which, in turn, results in an axial acceleration that maintains the resonance condition. Thus, the tapered field is a means of “tapping” the transverse kinetic energy of the beam. This can be accomplished by a tapering of either the wiggler amplitude or period; however, in the present work we shall confine ourselves to a tapered amplitude configuration. The results of the simulation are in qualitative agreement with those obtained for a helical wiggler configuration,²⁴ and indicate that the efficiency enhancement is extremely sensitive both to the point at which the taper is begun and to the slope of the taper. The optimal position at which to begin the taper is, typically, at a point shortly prior to saturation (for the untapered system) which corresponds to the trapping of the bulk of the electron beam in the ponderomotive potential formed by the beating of the wiggler and radiation fields.

For the case corresponding to the TE_{01} mode shown in Fig. 2, the optimal point at which to begin the taper occurs for $k_w z_0 \approx 110$. In order to accelerate the beam in the axial direction the wiggler field must be decreased, and the evolution of the wave power versus axial position is shown in Fig. 17 for a taper of $\epsilon_w = -0.007$. The efficiency enhancement (as measured by the growth in the wave power) continues for as long as the taper is maintained, and a maximum efficiency of $\eta_{\max} \approx 34.0\%$ is obtained if the wiggler field is tapered to zero at $k_w z \approx 253$ (i.e., 3.95 m). The effect of different choices for the wiggler taper is shown in Fig. 18, in which we plot the maximum efficiency found by tapering the wiggler field to zero versus ϵ_w . As shown in the figure, optimal results are found for $\epsilon_w \approx -0.002$ at which point $\eta_{\max} \approx 44\%$ and the interaction region extends to $k_w z \approx 610$ (i.e., 9.5 m). The variation in the relative phase for a tapered wiggler interaction is shown in Fig. 19, in which we plot the rela-

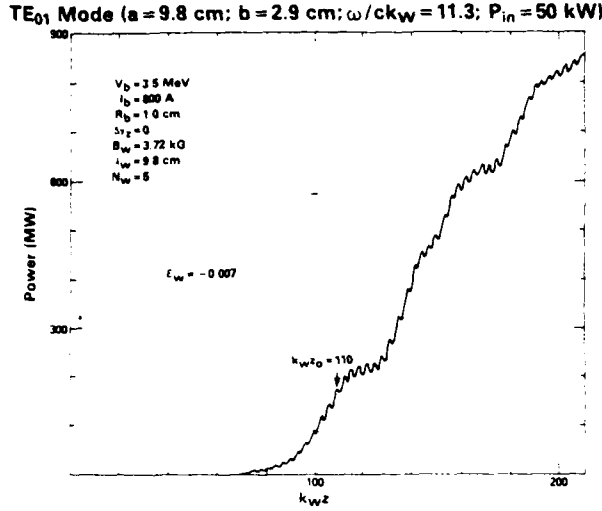


FIG. 17. Plot of the evolution of the TE₀₁ mode for a tapered wiggler interaction with $\epsilon_w = -0.007$ and $k_w z_0 = 110$.

tive phase versus axial position for $\epsilon_w = -0.007$, and $\omega/ck_w = 10.7, 11.0$, and 11.3 . Note that the start taper point is chosen to be the optimum value for each frequency, and is indicated in the figure by the arrow. Three features are readily apparent from the figure. The first is that the variation in the relative phase subsequent to the start-taper point is approximately the same for each of the three frequencies shown, and the spacing between the curves remains approximately constant. Second, while the phase variation within the tapered wiggler region initially increases immediately after the start-taper position, the phase variation appears to saturate and remain relatively constant over an extended interaction length. Third, the oscillations at one-half the wiggler appear to decrease in amplitude over the course of the tapered wiggler region.

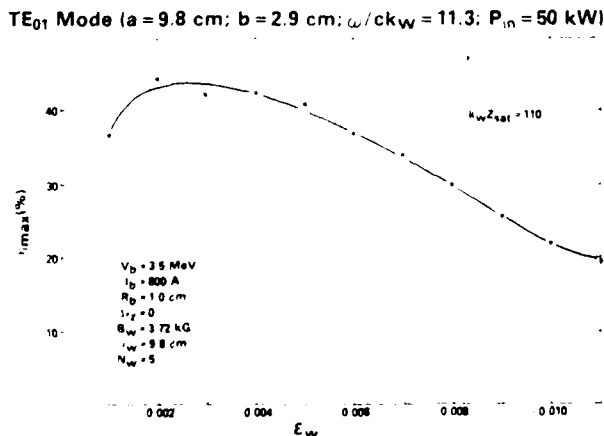


FIG. 18. Graph of the maximum efficiency of the TE₀₁ mode vs wiggler taper (ϵ_w).

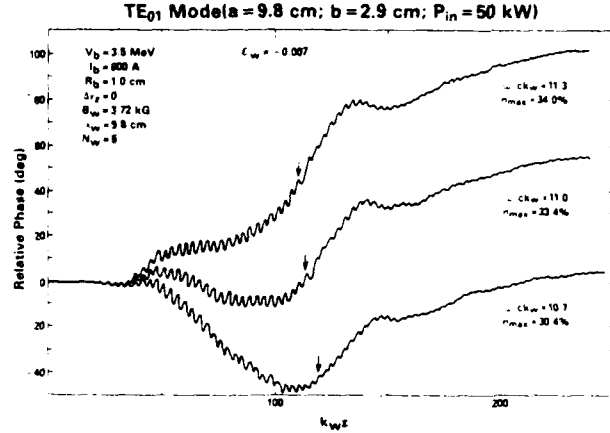


FIG. 19. Plot of the evolution of the relative phase during the course of the tapered wiggler interaction for $\omega/ck_w = 10.7, 11.0$, and 11.3 .

The effect of an initial beam momentum spread on the tapered wiggler-efficiency enhancement process has also been investigated, and the results are summarized in Fig. 20 in which we plot the maximum realizable efficiency (if the wiggler field is tapered to zero) versus $\Delta\gamma_z/\gamma_0$. The maximum efficiency at a fixed start-taper point ($k_w z_0 = 110$) chosen to correspond to the optimum position for $\Delta\gamma_z = 0$ is shown in Fig. 20(a) versus the axial

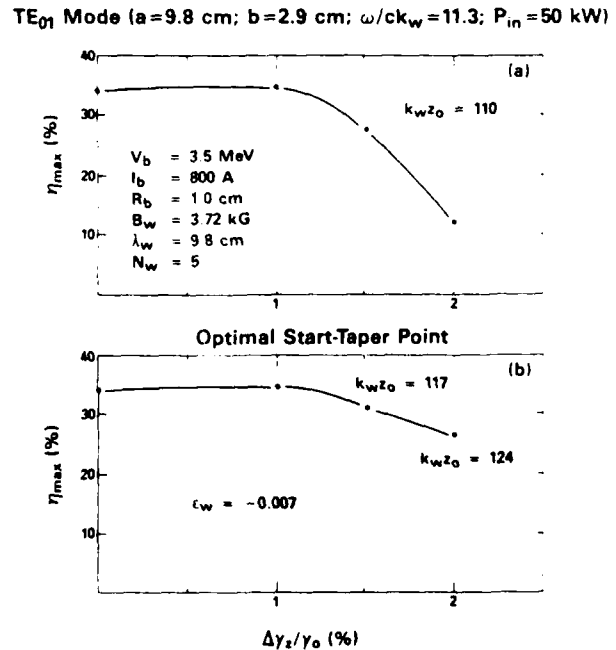


FIG. 20. Illustration of the effect of beam momentum spread on the tapered wiggler interaction at (a) fixed z_0 , and (b) variable z_0 . Observe that in (b) the optimal start-taper points correspond to $k_w z_0 = 110$ for $\Delta\gamma_z/\gamma_0 \leq 1\%$, $k_w z_0 = 117$ for $\Delta\gamma_z/\gamma_0 = 1.5\%$, and $k_w z_0 = 124$ for $\Delta\gamma_z/\gamma_0 = 2\%$.

momentum spread. As is evident from the figure, the efficiency-enhancement process is unaffected by the momentum spread for $\Delta\gamma_z/\gamma_0 \leq 1\%$, but decreases rapidly for axial energy spreads above this value. There are two principal reasons for this decrease in η_{\max} . The first is that the phase-trapping mechanism becomes less effective as the momentum spread increases because a proportionally greater fraction of the beam remains outside the trapped orbit region of the axial phase space. The second reason is that the increase in the momentum spread results in a decrease in the growth rate and a longer distance to saturation. Because of this, the optimum start-taper point is an increasing function of the momentum spread. Thus, if we determine the optimum start-taper point versus $\Delta\gamma_z$, then the maximum efficiency can be expected to decrease less rapidly with axial energy spread than is shown in Fig. 20(a). This is indeed the case, as shown in Fig. 20(b) in which we plot η_{\max} versus $\Delta\gamma_z$ for the optimum start-taper points. Note that for $\Delta\gamma_z/\gamma_0 \leq 1\%$ this point coincides with that for $\Delta\gamma_z = 0$ (for the current choice of parameters). As seen in the figure, $\eta_{\max} \approx 26.6\%$ for $\Delta\gamma_z/\gamma_0 = 2\%$ and a start-taper point of $k_w z_0 = 124$. This contrasts with an $\eta_{\max} \approx 11.8\%$ (and $\Delta\gamma_z/\gamma_0 = 2\%$) when $k_w z_0 = 110$. As a consequence, we conclude that although the untapered efficiency decreases relatively quickly with increasing momentum spread, the tapered-wiggler interaction can accept a small level of momentum spread without suffering a significant degradation in the interaction efficiency. However, the upper limit on the allowable momentum spread must be determined by the particular choice of experimental parameters, and the value of $\Delta\gamma_z/\gamma_0 \leq 1\%$ should not be construed to be a general result.

IV. SUMMARY AND DISCUSSION

In this paper a fully self-consistent nonlinear theory and numerical simulation has been developed for the FEL amplifier in three dimensions. The particular configuration of interest consists of a cylindrically symmetric electron beam of arbitrary cross section (on entry at $z = 0$) injected into a loss-free rectangular waveguide in the presence of a linearly polarized wiggler magnetic field. The wiggler-field model is that generated by a magnet stack in which the individual magnets have parabolically tapered pole pieces in order to provide for electron focusing in the plane of the bulk wiggler-induced motion. In addition, the adiabatic injection of the electron beam is modeled by the inclusion of an initial taper of the wiggler amplitude. The system of equations derived is a generalization of a previously described analysis of a helical wiggler-cylindrical waveguide configuration²³⁻²⁷ which treats the self-consistent evolution of the trajectories of an ensemble of electrons and the radiation fields. The analysis includes both the TE and TM modes, and includes the overlap of the transverse mode structure and the electron beam (i.e., the filling factor) in a self-consistent way. Space-charge fields have been neglected; hence, the analysis is restricted to the high-gain Compton (strong-pump) regime of operation. Since the problem of interest is the FEL amplifier, only single-frequency propa-

gation is considered, which permits an average over a wave period to be performed that eliminates the fast-time-scale phenomena formulation. This results in a great increase in computational efficiency over a full-scale particle-in-all simulation code, and allows the application of the technique to short (i.e., optical) wavelengths given an appropriate mode structure.

The electron trajectories are integrated using the complete Lorentz-force equations, so we are able to study the detailed orbital dynamics in the combined wiggler-radiation field structure. The overall bulk motion of the electron beam exhibits a dominant oscillation at the wiggler period, as well as a slow-time-scale betatron oscillation due to the transverse inhomogeneity in the wiggler field. The dynamics of the adiabatic injection of the electron beam were studied by means of a comparison of the saturation efficiency with the length of the entry taper region. The results indicate that the saturation efficiency increases relatively quickly with the length of the entry taper region for $N_w \leq 6$, and more slowly thereafter. The reason for this is that the injection process itself in a realistic (i.e., three-dimensional) wiggler field introduces a effective momentum spread on the beam which decreases as the axial wiggler gradient becomes more gradual. For practical purposes $N_w \geq 5$ appears to be an adequate compromise between the minimization of the overall wiggler length and the maximization of the interaction efficiency, and this is the regime in which many microwave FEL's have been operated.^{4-8,10-12} In addition, the effect of a tapered wiggler amplitude on the enhancement of the interaction efficiency can be included in a straightforward manner.

The numerical analysis has been performed for the case of a 35-GHz FEL amplifier which employs a 3.5-MeV, 800-A electron beam with an initial radius of 1.0 cm. The beam propagates through a rectangular waveguide with dimensions $a = 9.8$ cm and $b = 2.9$ cm in the presence of a wiggler field with a 3.72-kG amplitude and 9.8-cm period. Three distinct waveguide modes are found to be amplified: the TE₀₁, TE₂₁, and TM₂₁ modes. For this choice of frequency, the TE₀₁ mode exhibits the highest (untapered) efficiency, while the TE₂₁ mode has the highest growth rate. The wave-particle coupling for the TM₂₁ mode is the weakest of the three modes and has the lowest growth rate and efficiency as well as the narrowest bandwidth. The effect of an initial momentum spread is investigated for axial energy spreads $\Delta\gamma_z/\gamma_0 \leq 2\%$ which, for this choice of parameters, is well within the cold-beam regime. Results indicate that over this range of $\Delta\gamma_z$ the efficiency decreases in an approximately linear fashion with increasing axial energy spread. This is in substantial agreement with the results obtained for a helical wiggler configuration;²⁵ however, it should be remarked that the same distribution has been used for both the planar and helical wiggler configurations. Thus, while the planar and helical wigglers behave in substantially the same manner, the detailed scaling of the efficiency with the momentum spread can be expected to vary with the detailed choice of distribution.

The phase variation of the planar wiggler configuration discussed herein is also in qualitative agreement with that

found for helical wiggler configurations.²⁶ The principal difference is that an oscillation at one-half the wiggler period is superimposed on the bulk variation in the phase due to details of the wave-particle coupling with a planar wiggler. Specifically, for the gain band associated with the upper (high-frequency) intersection between the beam-resonance line and the waveguide-dispersion curve, we observe that the bulk variation of the relative phase decreases with axial position up to a point short of that at which the power saturates for frequencies at the low end of the band. As the frequency increases, the phase variation decreases until a critical frequency is reached for which the phase remains relatively constant over the course of the interaction. This critical frequency has been found to occur at approximately 10% below the frequency of peak growth rate for all parametric cases studied for both the helical and planar wigglers. Above this critical frequency the average relative phase tends to increase with axial position. In view of the high power potential of the FEL amplifier, applications such as microwave sources for the next generation of radio-frequency electron accelerators are natural considerations and the question of the phase stability of these devices against fluctuations in the electron-beam voltage is of importance. Again, we find qualitative agreement on this issue between simulations of helical and planar wiggler configurations. The results indicate a much poorer phase stability than the current generation of SLAC klystrons, and we conclude that applications of FEL amplifiers which require an extremely phase-stable microwave source will also require an electron beam with a very low level of voltage fluctuations.

The enhancement of the interaction efficiency by means of a tapered wiggler amplitude shows maximum efficiencies of the order of 35–45% are possible for this choice of parameters. This brings maximum power levels into the GW range. The simulation results also indicate that the tapered wiggler-efficiency-enhancement mechanism is relatively less sensitive to the effect of momentum spread than the uniform-wiggler case, and no degradation in the maximum efficiency is found for $\Delta\gamma_z/\gamma_0 \leq 1\%$ in the present case. Examination of the phase variation during the tapered wiggler interaction shows similar results over the entire gain band (Fig. 19), and there is no decrease in the phase separation for the various frequencies observed in the tapered wiggler region. Since variations in the frequency at fixed beam voltage are fundamentally equivalent to a variation in the voltage at fixed frequency (i.e., both processes *sweep* through the gain band), we find that our conclusion regarding the phase stability of FEL amplifiers is unaltered for the case of tapered wiggler interactions.

Indeed, the bulk features of the FEL interaction mechanism are found to be in substantial agreement for both helical and planar wiggler configurations. The most evident distinction is the rapid oscillation in both the power and relative phase which appears for planar wigglers at half the wiggler period. While the bulk wave amplification is unaffected by this oscillation, it may introduce an uncertainty in the measurement of the gain and/or power from planar wiggler configurations which is of the order of 10% (apart from systematic instrumental

errors). In addition, the relative phase also exhibits this oscillation, which indicates a periodic modulation in wave refraction also occurs. It is, therefore, an open question whether this may affect the focusing (i.e., optical guiding) of the radiation, and this will be addressed in a future work by the inclusion of multiple modes in the formulation. However, this question may be moot for tapered wiggler configurations since the oscillation appears to be attenuated (Fig. 19).

Although the configuration described in this paper does not precisely coincide with the experiment conducted by Orzechowski and co-workers,^{9,13} the parameters chosen for the numerical analysis coincide with those of the experiment and it is useful to compare the simulation with the experiment. The fundamental differences between the experimental configuration and the analytical model are that in the experiment (1) the beam was injected into the wiggler by means of an entry taper region one wiggler period in length, (2) a quadrupole field was used to provide electron focusing instead of parabolically shaped pole pieces, and (3) in the tapered wiggler experiment¹³ the amplitude was tapered nonlinearly. A 50-kW 34.6-GHz (i.e., $\omega/ck_w = 11.3$) magnetron was used to drive the FEL amplifier, and the signal was injected in such a way as to couple primarily to the TE_{01} mode. As a result, the TE_{01} mode was the predominant component of the output signal; however, significant power levels were also detected in the TE_{21} and TM_{21} modes. The detailed experimental parameters we choose to compare with the experiment involve a 3.5-MeV, 850-A electron beam used in the tapered wiggler experiment. Although the beam is thought to exhibit a slightly elliptical cross section, the average of the semimajor and semiminor radii is about 1.0 cm and we choose this value for the beam radius in the numerical simulation. The waveguide and wiggler parameters are those used previously in Sec. III, and we note that since the fringing fields are not included in our model of the entry taper region the choice of $N_w = 5$ is a compromise. The evolution of the wave power in the TE_{01} mode as a function of axial position for these parameters is shown in Fig. 21 for a uniform wiggler ($\epsilon_w = 0$), and for $\epsilon_w = -0.007$. The results are similar to those described in the preceding section for an 800-A beam, and the best fit with the experiment is found for an axial energy spread of $\Delta\gamma_z/\gamma_0 \approx 1\%$. As shown in the figure, the untapered wiggler results give a saturated power of 194 MW over a uniform wiggler-interaction region (i.e., $Z_{sat} = 5\lambda_w$) of 1.4 m in length. This compares well with the experimental measurement of 180 MW over an interaction length of 1.3 m, and the discrepancies are within the experimental uncertainty. We remark, however, that the simulation results may be affected by as much as 20% by the choice of the length of the entry taper region. It is more difficult to compare the simulation (with a linear wiggler taper) and the experiment (with a nonlinear taper) in such a detailed fashion. It is certainly reasonable to expect that a nonlinear taper might be more efficient than a linear one in the sense that the efficiency enhancement can be accomplished over a shorter interaction region. Thus, in the comparison of the tapered wiggler results we interpret the simulation as an indication of limits on the energy extrac-

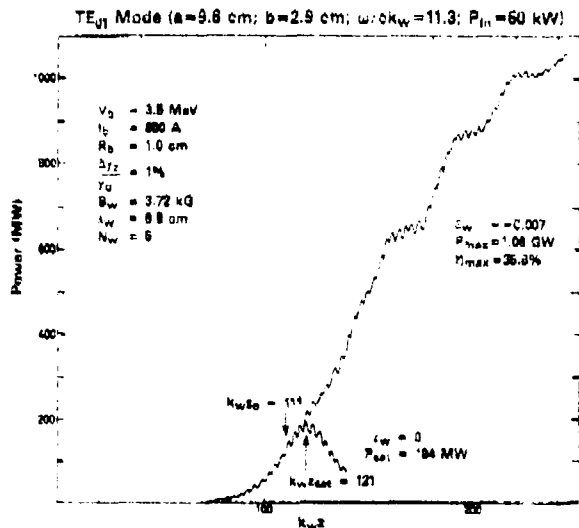


FIG. 21 Plot showing the evolution of the TE_{01} mode vs axial position for a uniform and tapered wiggler interaction.

tion. With this in mind we observe that the optimal start-taper point is at $k_w z_0 \approx 111$ (slightly more than one wiggler period short of the saturation point for a uniform wiggler). We choose the slope of the taper to correspond roughly with the *average* taper in the experiment, and find a maximum efficiency of about $\eta_{\max} \approx 35.6\%$ at a power level of 1.06 GW. This differs by only about 8% from that found in the experiment, and we interpret this as good agreement within the uncertainty introduced by the differences in the slope of the taper. We conclude, therefore, that the simulation is consistent with the interpretation of a 1% axial beam energy spread, which is supported by an electron-spectrometer measurement indicating an upper limit on the energy spread of 2%.³⁹ Furthermore, in view of the relative insensitivity of the tapered wiggler interaction (see Fig. 20), we conclude that the performance of the tapered wiggler experiment would not be markedly improved by a further improvement in beam quality (i.e., a decrease in the momentum spread).

It is useful to compare the analysis and simulation described herein with other models in order to assess the relative merits of the various formulations of the problem. To this end, we consider the simulation code FRED in use at the Lawrence Livermore National Laboratory^{28,40} because this code has been used extensively to model and in-

terpret the experiment. It is important to recognize that simulational models and computer codes undergo rapid development which renders an accurate description difficult; hence, I will confine my remarks to fundamental properties which include the particle dynamics and the treatment of the radiation field. The particle dynamics in FRED are treated in a reduced form by averaging the orbit equations over a wiggler period. The transverse motion is described in terms of the bulk wiggler and betatron oscillations by means of an analytical approximation, and the self-consistent effect of the radiation field on the transverse motion is not included. The dynamics in the axial direction are handled by integration of equations for the particle phase and energy. This is the most common approach used in the simulation of free-electron lasers and, as shown by the comparison between FRED and the experimental results,^{9,13} it works well. However, certain effects are excluded from this formulation. First, we observe that the rapid oscillation at the second wiggler harmonic is lost entirely due to the averaging of the orbit equations over a wiggler period. Second, the injection of the electron beam into the wiggler is excluded from the simulation, and must be described explicitly. Third, because the self-consistent effect of the radiation field on the transverse electron motion is not included, the initial transients associated with the injection of the radiation into the amplifier are not properly handled. As a result, launching losses cannot be described by FRED, and the wave power must be initialized at a lower value than that actually injected into the amplifier.⁹ Thus, it is our opinion that the approach to the particle dynamics described in this paper is superior to that employed in FRED. The advantage of FRED over the single-mode analysis we have described is that the radiation field is treated by means of a field solver which implicitly handles multiple modes and, thus, describes the optical guiding (i.e., focusing) of the radiation due to the electron-beam interaction. However, optical guiding can be treated via a multimode formulation of the present analysis as well. Indeed, such an analysis is now under study, and the results will be presented in the forthcoming work.

ACKNOWLEDGMENTS

This research was supported by the Office of Naval Research and the Office of Naval Technology. The authors would like to thank Dr. A. K. Ganguly, Dr. R. K. Parker, Dr. R. Sprangle, and Dr. R. H. Jackson for helpful discussions.

¹R. M. Phillips, IRE Trans. Electron Dev. 7, 231 (1960).

²V. L. Granatstein, S. P. Schlesinger, M. Herndon, R. K. Parker, and J. A. Pasour, Appl. Phys. Lett. 30, 384 (1977).

³D. B. McDermott, T. C. Marshall, S. P. Schlesinger, R. K. Parker, and V. L. Granatstein, Phys. Rev. Lett. 41, 1368 (1978).

⁴R. K. Parker, R. H. Jackson, S. H. Gold, H. P. Freund, V. L. Granatstein, P. C. Efthimion, M. Herndon, and A. K. Kinkead, Phys. Rev. Lett. 48, 238 (1982).

⁵J. Fajans, G. Bekefi, Y. Z. Yin, and B. Lax, Phys. Rev. Lett. 53, 246 (1984).

⁶J. A. Pasour, R. F. Lucey, and C. W. Roberson, in Free-Electron Generators of Coherent Radiation, edited by C. A. Brau, S. F. Jacobs, and M. O. Scully [Proc. Soc. Photo. Opt.-Instrum. Eng. 453, 328 (1984)].

⁷J. A. Pasour, R. F. Lucey, and C. A. Kapetanakis, Phys. Rev. Lett. 53, 1728 (1984).

⁸S. H. Gold, D. L. Hardesty, A. K. Kinkead, L. R. Barnett, and

- V. L. Granatstein, Phys. Rev. Lett. **52**, 1218 (1984).
- ⁹T. J. Orzechowski, B. Anderson, W. M. Fawley, D. Prosnitz, E. T. Scharlemann, S. Yarema, D. Hopkins, A. C. Paul, A. M. Sessler, and J. Wurtele, Phys. Rev. Lett. **54**, 889 (1985).
- ¹⁰J. Fajans, G. Bekefi, Y. Z. Yin, and B. Lax, Phys. Fluids **28**, 1995 (1985).
- ¹¹J. Masud, T. C. Marshall, S. P. Schlesinger, and F. G. Yee, Phys. Rev. Lett. **56**, 1567 (1986).
- ¹²J. Fajans, J. Wurtele, G. Bekefi, D. S. Knowles, and K. Xu, Phys. Rev. Lett. **57**, 579 (1986).
- ¹³T. J. Orzechowski, B. Anderson, J. C. Clark, W. M. Fawley, A. C. Paul, D. Prosnitz, E. T. Scharlemann, S. Yarema, D. B. Hopkins, A. M. Sessler, and J. Wurtele, Phys. Rev. Lett. **57**, 2172 (1986).
- ¹⁴L. R. Elias, W. M. Fairbanks, J. M. J. Madey, H. A. Schwettman, and T. I. Smith, Phys. Rev. Lett. **36**, 717 (1976).
- ¹⁵D. A. G. Deacon, L. R. Elias, J. M. J. Madey, G. J. Ramian, H. A. Schwettman, and T. I. Smith, Phys. Rev. Lett. **38**, 892 (1977).
- ¹⁶R. W. Warren, B. E. Newnam, J. G. Winston, W. E. Stein, L. M. Young, and C. A. Brau, IEEE J. Quantum Electron. **QE-19**, 391 (1983).
- ¹⁷M. Billandon, P. Ellaume, J. M. Ortega, C. Bazin, M. Bergher, M. Velghe, Y. Petroff, D. A. G. Deacon, K. E. Robinson, and J. M. J. Madey, Phys. Rev. Lett. **51**, 1652 (1983).
- ¹⁸J. M. Slater, J. L. Adamski, D. C. Quimby, T. L. Churchill, L. Y. Nelson, and R. E. Center, IEEE J. Quantum Electron. **QE-19**, 374 (1983).
- ¹⁹J. A. Edighoffer, G. R. Neil, C. E. Hess, T. I. Smith, S. W. Fornaca, and H. A. Schwettman, Phys. Rev. Lett. **52**, 344 (1984).
- ²⁰B. E. Newnam, R. W. Warren, R. L. Sheffield, W. E. Stein, M. T. Lynch, J. S. Fraser, J. C. Goldstein, J. E. Sollid, T. A. Swann, J. M. Watson, and C. A. Brau, IEEE J. Quantum Electron. **QE-21**, 867 (1985).
- ²¹C. R. Pidgeon, S. D. Smith, W. J. Firth, D. A. Jorosynski, D. M. Trait, J. S. Mackay, M. F. Kimmitt, J. M. Reid, M. G. Kelliher, M. W. Poole, G. Saxon, R. P. Walker, W. A. Gillespie, and P. F. Martin, IEEE J. Quantum Electron. **QE-21**, 1083 (1985).
- ²²B. Levush, W. M. Manheimer, T. Antonsen, and P. Sprangle, Phys. Fluids **28**, 2273 (1985).
- ²³A. K. Ganguly, and H. P. Freund, Phys. Rev. A **32**, 2275 (1985).
- ²⁴H. P. Freund and A. K. Ganguly, Phys. Rev. A **33**, 1060 (1986).
- ²⁵H. P. Freund and A. K. Ganguly, Phys. Rev. A **34**, 1242 (1986).
- ²⁶H. P. Freund and A. K. Ganguly, IEEE J. Quantum Electron. (to be published).
- ²⁷A. K. Ganguly and H. P. Freund (unpublished).
- ²⁸E. T. Scharlemann, J. Appl. Phys. **58**, 2154 (1985).
- ²⁹P. Sprangle, C. M. Tang, and W. M. Manheimer, Phys. Rev. A **21**, 302 (1980).
- ³⁰R. W. Pierce, J. Jasberg, and J. V. Lebaqz, in *The Stanford Two-Mile Accelerator*, edited by R. B. Neal (Benjamin, New York, 1968), Chap. 10, p. 307.
- ³¹P. Sprangle, C. M. Tang, and W. M. Manheimer, Phys. Rev. Lett. **43**, 1932 (1979).
- ³²N. M. Kroll, P. L. Morton, and M. N. Rosenbluth, in *Physics of Quantum Electronics: Free-Electron Generators of Coherent Radiation*, edited by S. F. Jacobs, H. S. Pilloff, M. Sargent, M. O. Scully, and R. Spitzer (Addison-Wesley, Reading, MA, 1980), Vol. 7, Chaps. 4 and 5.
- ³³A. Szoke, V. K. Neil, and D. Prosnitz, in Ref. 32, Chap. 7, p. 175.
- ³⁴D. Prosnitz, A. Szoke, and V. K. Neil, in Ref. 32, Chap. 21, p. 575.
- ³⁵S. A. Mani, in Ref. 32, Chap. 22, p. 589.
- ³⁶C. A. Brau and R. K. Cooper, in Ref. 32, Chap. 24, p. 647.
- ³⁷J. M. Slater, J. Adamski, D. C. Quimby, W. M. Grossman, T. L. Churchill, and R. E. Center, in *Proceedings of the International Conference on Lasers '82*, edited by R. C. Powell (STS Press, McLean, VA, 1982), p. 212.
- ³⁸P. Sprangle and C. M. Tang, Appl. Phys. Lett. **39**, 677 (1981).
- ³⁹T. J. Orzechowski (private communication).
- ⁴⁰W. M. Fawley, D. Prosnitz, S. Doss, and R. Galinas, in *Free-Electron Generators of Coherent Radiation*, edited by C. A. Brau, S. F. Jacobs, and M. O. Scully [Proc. Soc. Photo. Opt.-Instrum. Eng. **453**, 212 (1984)].

APPENDIX II

HARMONIC GENERATION IN
FREE-ELECTRON LASERS

Harmonic generation in free-electron lasers

H. P. Freund and C. L. Chang

Science Applications International Corporation, McLean, Virginia 22102

H. Bluem

Department of Electrical Engineering, University of Maryland, College Park, Maryland 20742

(Received 22 May 1987)

A nonlinear formulation of the free-electron-laser amplifier with a linearly polarized wiggler magnetic field is used to study harmonic generation. Substantial emission is found to occur at the harmonics for a cold beam; however, the harmonics are far more sensitive to beam thermal effects than is the fundamental.

The question of harmonic generation in free-electron lasers (FEL's) has become increasingly important in recent years. The operation of an FEL oscillator at visible wavelengths driven by the ACO (les Anneaux de Collisions de l'Accélérateur Linéaire d'Orsay) storage ring¹ has shown that the generation of harmonics at uv wavelengths can limit performance due to severe degradation of the optical system. In contrast, there is interest in the generation of harmonics in an effort to achieve ever shorter wavelengths without the necessity of ever higher electron beam energies. In order to address these questions, we have developed a fully three-dimensional formulation of the FEL amplifier for a configuration which consists of an electron beam propagating through a rectangular waveguide in the presence of a linearly polarized wiggler magnetic field. A set of nonlinear differential equations is derived which self-consistently describes the evolution of both an ensemble of electrons and the electromagnetic fields. The issue of harmonic generation [i.e., $\omega \approx (k + lk_w)v_z$ for $l > 1$] has been addressed previously for the case of an electron beam propagating through a cylindrical waveguide in the presence

of a helical wiggler field,² and emission was shown to occur at all harmonics of the resonant frequency. However, due to the modulation of the axial electron velocity in linearly polarized wiggler fields, only the odd harmonics are excited. In this paper we study both the linear growth rates and nonlinear saturation efficiencies at the odd harmonics, as well as the effect of thermal spread on harmonic generation.

The configuration we consider is that of a relativistic electron beam propagating through a loss-free rectangular waveguide in the presence of a linearly polarized wiggler magnetic field. The wiggler-field model we employ is that encountered when the individual magnets in the wiggler have parabolically tapered pole faces. The wiggler field generated in this way provides for electron beam focusing in the plane of the principal wiggler motion, and was first employed experimentally by Phillips.³ A detailed analysis of the magnetic field produced by a wiggler with parabolically tapered pole pieces was undertaken by Scharlemann,⁴ who showed that the wiggler field is of the form

$$B_w(x) = B_w \left\{ \cos(k_w z) \left[\sinh \left[\frac{k_w x}{\sqrt{2}} \right] \sinh \left[\frac{k_w y}{\sqrt{2}} \right] \hat{e}_x + \cosh \left[\frac{k_w x}{\sqrt{2}} \right] \cosh \left[\frac{k_w y}{\sqrt{2}} \right] \hat{e}_y \right] - \sqrt{2} \cosh \left[\frac{k_w x}{\sqrt{2}} \right] \sinh \left[\frac{k_w y}{\sqrt{2}} \right] \sin(k_w z) \hat{e}_z \right\}, \tag{1}$$

where B_w denotes the wiggler amplitude and k_w ($\equiv 2\pi/\lambda_w$) is the wiggler wave number. In addition, we model the injection of an electron beam into the wiggler by allowing the wiggler amplitude to increase adiabatically from zero to a constant level over N_w wiggler periods as follows:

$$B_w(z) = \begin{cases} B_w \sin^2 \left[\frac{k_w z}{4N_w} \right], & 0 \leq z \leq N_w \lambda_w \\ B_w, & z > N_w \lambda_w \end{cases} \tag{2}$$

Note, however, that fringing fields associated with the tapered wiggler amplitude are neglected, and this representation (for $z < N_w \lambda_w$) is valid only for large N_w . For the purposes of the present analysis, we choose $N_w = 10$.

The boundary conditions at the waveguide wall may be satisfied by expanding the vector potential in terms of the orthogonal basis functions of the TE modes, and we write the vector potential of the radiation field in the form

$$\delta A(x, t) = \sum_{\substack{n=0 \\ n=0}}^{\infty} \delta A_{mn}(z) e_{mn}(x, y) \cos \alpha, \tag{3}$$

where for frequency ω and wave number $k(z)$

$$\alpha \equiv \int_0^z dz' k(z') - \omega t, \quad (4)$$

Σ' indicates that m and n are not both zero, and

$$\begin{aligned} \mathbf{e}_{mn}(x, y) \equiv & \frac{\pi n}{k_{mn} b} \cos \left[\frac{m \pi X}{a} \right] \sin \left[\frac{n \pi Y}{b} \right] \hat{\mathbf{e}}_x \\ & - \frac{\pi m}{k_{mn} a} \sin \left[\frac{m \pi X}{a} \right] \cos \left[\frac{n \pi Y}{b} \right] \hat{\mathbf{e}}_y \end{aligned} \quad (5)$$

is the polarization vector. In this representation the waveguide is assumed to be centered at the origin and bounded by $-a/2 \leq x \leq a/2$ and $-b/2 \leq y \leq b/2$. As a consequence, $X \equiv x + a/2$, $Y \equiv y + b/2$, and

$$k_{mn} \equiv \pi \left[\frac{m^2}{a^2} + \frac{n^2}{b^2} \right]^{1/2} \quad (6)$$

denotes the cutoff wave number. It is implicitly assumed that both the mode amplitudes $\delta A_{mn}(z)$ and the wave number $k(z)$ vary slowly over a wave period.

A detailed derivation of the equations which describe the evolution of the mode amplitudes and wave number has been presented⁵ for both the TE and TM modes; however, the method follows that employed for a helical wiggler.² Here we note that substitution of the fields (3) into Maxwell's equations yields

$$\begin{aligned} \frac{d^2}{dz^2} \delta a_{mn} + \left[\frac{\omega^2}{c^2} - k^2 - k_{mn}^2 \right] \delta a_{mn} \\ = \frac{\omega_b^2}{c^2} F_{mn} \beta_{z0} \left\langle \frac{\cos \alpha}{|v_z|} \mathbf{e}_{mn} \cdot \mathbf{v} \right\rangle \end{aligned} \quad (7)$$

and

$$2k^{1/2} \frac{d}{dz} (k^{1/2} \delta a_{mn}) = - \frac{\omega_b^2}{c^2} F_{mn} \beta_{z0} \left\langle \frac{\sin \alpha}{|v_z|} \mathbf{e}_{mn} \cdot \mathbf{v} \right\rangle \quad (8)$$

upon orthogonalization in x and y , and an average over the wave period. In Eqs. (7) and (8), $\delta a_{mn} = e \delta A_{mn} / mc^2$, ω_b is the ambient plasma frequency, $\beta_{z0} \equiv v_{z0} / c$ (where v_{z0} is the initial axial beam velocity), \mathbf{v} is the instantaneous velocity, and $F_{mn} = 4$ (8) when either $m = 0$ or $n = 0$ ($m \neq 0$ and $n \neq 0$). The averaging operator $\langle (\dots) \rangle$ describes the source current and includes the effect of an initial (i.e., at $z = 0$) thermal spread in the beam by means of the distribution function

$$\begin{aligned} F_0(\mathbf{p}_0) = A \exp[-(p_{z0} - p_0)^2 / \Delta p_z^2] \\ \times \delta(p_0^2 - p_{i0}^2 - p_{z0}^2) \Theta(p_{z0}), \end{aligned} \quad (9)$$

where p_0 and Δp_z describe the initial bulk momentum and the momentum spread of the beam, $\Theta(x)$ is the Heaviside function, and the normalization constant is

$$A = \left[\pi \int_0^{p_0} dp_{z0} \exp[-(p_{z0} - p_0)^2 / \Delta p_z^2] \right]^{-1}. \quad (10)$$

This distribution describes an initially monoenergetic beam with a pitch-angle spread. The average is over the initial conditions and defined as

$$\begin{aligned} \langle \dots \rangle \equiv & \frac{A}{2\pi ab} \int_0^{2\pi} d\phi_0 \int_0^{p_0} dp_{z0} \frac{p_{z0}}{p_0} \exp[-(p_{z0} - p_0)^2 / \Delta p_z^2] \\ & \times \int_{-\pi}^{\pi} d\alpha_0 \sigma_{\parallel}(\alpha_0) \int_{-a/2}^{a/2} dx_0 \int_{-b/2}^{b/2} dy_0 \sigma_{\perp}(x_0, y_0) \langle \dots \rangle, \end{aligned} \quad (11)$$

where $\alpha_0 (\equiv -\omega t_0$ and t_0 is the time the electron crosses the $z = 0$ plane) is the initial phase, $\phi_0 \equiv \tan^{-1}(p_{y0}/p_{x0})$, and $\sigma_{\parallel}(\alpha_0)$ and $\sigma_{\perp}(x_0, y_0)$ describe the electron distributions in initial phase and initial cross section. For simplicity, we assume the beam to be uniformly distributed in phase ($\sigma_{\parallel} = 1$) and cross section for an initially cylindrical beam (i.e., $\sigma_{\perp} = 1$ for $r_0 \leq R_b$). In order to complete the formulation, the electron trajectories are followed by means of the Lorentz force equations in the combined wiggler and radiation fields. It should be remarked that although the fast-time-scale behavior of Maxwell's equations have been eliminated by means of the average over a wave period, no average of the Lorentz force equations is undertaken. This is important in order to resolve the interaction at higher harmonics.

Equations (7) and (8) can be reduced to a set of three first-order differential equations describing the evolution of the amplitude δa_{mn} , the growth rate Γ_{mn} ($\equiv d \ln \delta a_{mn} / dz$), and the wave number. Hence, includ-

ing the orbit equations, we solve an initial-value problem composed of a set of $6N + 3$ coupled nonlinear differential equations, where N is the number of particles. The field quantities are initialized such that $\delta a_{mn}(z = 0)$ describes an arbitrary input power level, $\Gamma_{mn}(z = 0) = 0$, and $k(z = 0) = (\omega^2 / c^2 - k_{mn}^2)^{1/2}$. Thus, while the initial state describes a vacuum mode, the system evolves into a dielectrically loaded waveguide mode in the presence of the beam.

The particular example we consider involves a 3.3-MeV, 100-A electron beam with an initial radius of 0.2 cm propagating through a rectangular waveguide ($a = 10$ cm, $b = 3$ cm) in the presence of a wiggler with a 4.2-kG amplitude and a 9.8-cm period. A spectrum of the efficiency, η , of the TE₀₁ mode is shown in Fig. 1 as a function of frequency for the fundamental through the ninth harmonic in the absence of any thermal spread (i.e., $\Delta p_z = 0$). The doublet at the fundamental corresponds to the upper and lower intersections between the waveguide dispersion curve and the beam-resonance line

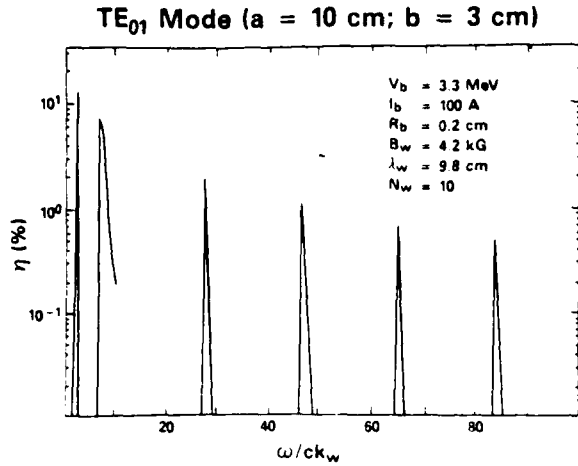


FIG. 1. Plot of the efficiency vs frequency at the fundamental, third, fifth, seventh, and ninth harmonics.

$[\omega \approx (k + k_w)v_z]$. It is evident from the figure that there is a sharp drop in the efficiency between the fundamental and the third harmonic. However, the subsequent decrease of the efficiency with harmonic number is rather slow, and substantial power may be found at the higher harmonics. In addition, the decrease in the growth rates with harmonic number is relatively slow. Because of variations in the launching loss associated with the various harmonics, as well as oscillations in the growth rate over the course of the interaction, it is difficult to obtain estimates of the average growth rates. However, the distance to saturation (z_{sat}) for a fixed input signal of 6 kW provides a measure of the average growth rate. For example, the peak growth rate is obtained at $\omega/ck_w \approx 7.25$ for the fundamental (upper intersection), and saturation occurs at $k_w z_{\text{sat}} \approx 184$ with an efficiency $\eta \approx 5.57\%$. At the third harmonic, peak growth is found for $\omega/ck_w \approx 27.25$, and saturation occurs at $k_w z_{\text{sat}} \approx 172$ with an efficiency $\eta \approx 0.81\%$. In view of the shorter saturation length and lower efficiency at the harmonic, it is clear that the third-harmonic growth rate is a substantial fraction of that at the fundamental. A similar conclusion is obtained at the seventh harmonic which displays a peak growth rate at $\omega/ck_w \approx 65.5$ and a saturation length $k_w z_{\text{sat}} \approx 172$ with $\eta \approx 0.39\%$.

The effect of the thermal spread is shown in Fig. 2 in which we plot the normalized efficiency η/η_0 (η_0 is the efficiency for $\Delta p_z = 0$) versus the axial energy spread $\Delta\gamma_z/\gamma_0$. Observe that since the initial distribution is monoenergetic

$$\frac{\Delta\gamma_z}{\gamma_0} \approx 1 - \left[1 + 2(\gamma_0^2 - 1) \frac{\Delta p_z}{p_0} \right]^{-1/2}, \quad (12)$$

where $\gamma_0^2 \equiv 1 + p_0^2/m^2c^2$. The principal conclusion to be drawn from the figure is that the harmonic emission is far more sensitive to the effect of the thermal spread than the fundamental. While the efficiency decreases by an order of magnitude for $\Delta\gamma_z/\gamma_0 \geq 2\%$ at the fundamental, a corresponding decrease occurs for

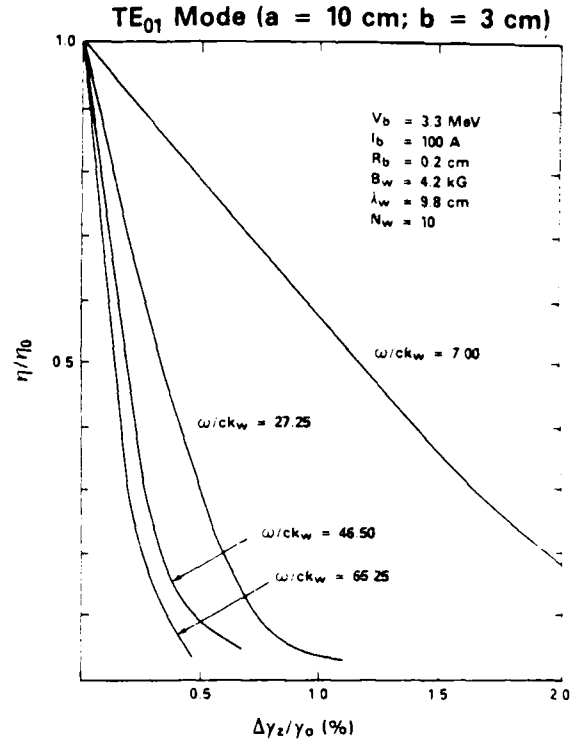


FIG. 2. Thermal effect on the efficiency.

$\Delta\gamma_z/\gamma_0 \approx 0.7\%$ at the third harmonic. At higher harmonics the decrease is even more rapid. In addition, as found by Davidson,⁶ the growth rates are also more sensitive to the thermal spread at the harmonics than at the fundamental. While the saturation length increases from $k_w z_{\text{sat}} \approx 199$ to $k_w z_{\text{sat}} \approx 209$ at $\omega/ck_w = 7.0$ (fundamental) as the thermal spread increases to $\Delta\gamma_z/\gamma_0 \approx 1\%$, the decrease is more rapid at the third harmonic. For this case, the saturation length increases from $k_w z_{\text{sat}} \approx 205$ to $k_w z_{\text{sat}} \approx 241$ at $\omega/ck_w \approx 27.25$ as the axial energy spread increases to $\Delta\gamma_z/\gamma_0 \approx 0.5\%$. At $\omega/ck_w = 65.25$ (seventh harmonic) the saturation length increases from $k_w z_{\text{sat}} \approx 205$ to $k_w z_{\text{sat}} \approx 257$ as the thermal spread increases to $\Delta\gamma_z/\gamma_0 \approx 0.27\%$.

The question of the effect of the thermal spread on harmonic generation has been addressed in an analytic model of the low-gain, single-particle regime by Coisson and de Martini.⁷ The results of the analytic model also showed that the sensitivity of the interaction to the beam thermal spread increased with the harmonic number. The reason for this can be understood by consideration of the resonance condition $\omega - (k + ik_w)v_z \approx 0$, so that the transition to the thermally dominated regime occurs when $(\text{Re}k + ik_w)\Delta v_z \approx (\text{Im}k)\bar{v}_z$ where Δv_z is the axial velocity spread, \bar{v}_z is the bulk axial velocity of the beam, $\text{Re}k$ is the wave number, and $\text{Im}k$ is the growth rate. Since the growth rate typically decreases with increasing harmonic number⁶ while the wave number increases (i.e., it is a higher-frequency interaction), it is clear that the transition to the thermally dominated regime occurs for progressively lower values of $\Delta v_z/\bar{v}_z$ as

the harmonic number increases.

The issue of beam propagation through the wiggler can also be addressed with this formulation. Results indicate that while the entire beam propagates through the system in the absence of a thermal spread, a substantial fraction of the beam can be lost to the wall for even moderate thermal spreads (i.e., $\Delta\gamma_z/\gamma_0 \geq 1\%$) at this beam energy.

In summary, the results indicate that substantial growth rates and efficiencies at the higher harmonics are obtainable at the cost of more stringent requirements on beam quality. It should also be remarked that while the difficulties harmonic emission posed for the optical FEL

oscillator at ACO were due to spontaneous (rather than coherent) emission, the higher beam currents obtainable on the forthcoming super-ACO storage ring could lead to coherent harmonic generation. Such problems are due, in large part, to the excellent beam quality (i.e., $\Delta\gamma_z/\gamma_0 \approx 0.1\%$) obtainable with a storage ring.

This work was supported by the Office of Naval Research and the Office of Naval Technology. The authors would like to thank Dr. A. K. Ganguly, Dr. R. K. Parker, Dr. A. T. Drobot, and Dr. R. H. Jackson for helpful discussions.

¹M. Billardon, P. Ellaume, J. M. Ortega, C. Bazin, M. Bergher, M. Velghe, Y. Petroff, D. A. G. Deacon, K. E. Robinson, and J. M. J. Madey, *Phys. Rev. Lett.* **51**, 1652 (1983).

²A. K. Ganguly and H. P. Freund, *Phys. Rev. A* **32**, 2275 (1985).

³R. M. Phillips, *IRE Trans. Electron Devices* **7**, 231 (1960).

⁴E. T. Scharlemann, *J. Appl. Phys.* **58**, 2154 (1985).

⁵H. P. Freund, H. Bluem, and C. L. Chang, *Phys. Rev. A* **36**,

2182 (1987).

⁶R. C. Davidson, *Phys. Fluids* **29**, 267 (1986).

⁷R. Coisson and F. de Martini, in *Physics of Quantum Electronics: Free-Electron Generators of Coherent Radiation*, edited by S. F. Jacobs, G. T. Moore, H. S. Pilloff, M. Sargent, M. O. Scully, and R. Spitzer (Addison-Wesley, Reading, Mass., 1982), Vol. 9, p. 939.

APPENDIX III

MULTI-MODE NONLINEAR ANALYSIS OF
FREE-ELECTRON LASER AMPLIFIERS IN
THREE-DIMENSIONS

A-III

MULTI-MODE NONLINEAR ANALYSIS OF FREE-ELECTRON LASER AMPLIFIERS IN THREE-DIMENSIONS

H.P. Freund

Science Applications International Corporation

McLean, VA 22102

ABSTRACT

The nonlinear evolution of a Free-Electron Laser (FEL) amplifier is investigated for a configuration in which an electron beam propagates through an overmoded rectangular waveguide in the presence of a planar wiggler with parabolically tapered pole pieces. The analysis is fully three-dimensional and describes the evolution of an arbitrary number of resonant TE and/or TM modes of the rectangular guide as well as the trajectories of an ensemble of electrons. Numerical simulations are conducted for parameters consistent with the 35-GHz amplifier experiment performed by Orzechowski and coworkers, in which the TE_{01} , TE_{21} , and TM_{21} modes were observed. The theory is found to be in good agreement with the experiment. Surprisingly, comparison with a single-mode analysis shows that the enhancement of the efficiency of the TE_{01} mode obtained by means of a tapered wiggler is significantly greater (as well as being in substantial agreement with the experiment) when the TE_{21} and TM_{21} modes are included in the simulation.

I. INTRODUCTION

The Free-Electron Laser (FEL) has been shown to be a high power radiation source over a broad spectrum extending from microwave¹⁻¹³ through optical¹⁴⁻²¹ wavelengths. For operation at relatively low beam energies (typically below about 500 keV) and long wavelengths, the device is termed a Ubitron¹ and the interaction occurs in the vicinity of the lowest order waveguide cutoff. As a consequence, the system can be designed in such a way that the beam is resonant only with the lowest order waveguide mode, and a single-mode analysis is sufficient to describe many aspects of the interaction. However, at higher energies and shorter wavelengths, the interaction is overmoded in the sense that the electron beam can be resonant with several (perhaps many) modes, and the competition between the modes has important consequences for the interaction.

The motivation for the present work is to develop a multi-mode nonlinear theory and simulation code for a Ubitron/FEL amplifier. The analysis is based on previously described single-mode analyses of helical wiggler/axial guide field²²⁻²⁵ and planar wiggler²⁶ configurations. The development of a multi-mode analysis represents a straightforward generalization of the single-mode theories, and involves the calculation of $\mathbf{J} \cdot \mathbf{E}$ for each mode as well as the integration of electron trajectories in the aggregate field composed of the sum of all the resonant modes. The particular configuration considered in the present work is that of a planar wiggler geometry in which the electron beam propagates through a rectangular waveguide. The detailed wiggler model we employ includes the effect of parabolically shaped pole pieces in order to provide for electron focussing in the plane of the bulk wiggler motion,^{1,27} and we model the injection of the electron beam into the wiggler by allowing the wiggler amplitude to increase adiabatically from zero to a constant level. In addition, we consider the effect of a tapered wiggler amplitude on efficiency enhancement in overmoded systems. As in the case of the single-mode analysis,²⁶ the overlap between the electron beam and the transverse mode structure of either TE or TM modes is included in a self-consistent

way, and no arbitrary "filling-factor" is necessary. Although the problem of interest is that of an overmoded FEL amplifier which requires a multi-mode treatment, only single-frequency propagation need be considered. As a result, Maxwell's equations may be averaged over a wave period which results in the elimination of the fast-time-scale phenomena from the formulation.

The organization of the paper is as follows. The general formulation is described in Sec. II, and allows for the inclusion of an arbitrary number of modes of TE and/or TM polarization, subject to the restriction that all are propagating modes at the same frequency. A direct application of the multi-mode analysis is to the description of a recent experiment by. and coworkers,^{9,13} in which the TE_{01} , TE_{21} , and TM_{21} modes of a rectangular waveguide were observed. Numerical examples appropriate to this experiment are discussed in Sec. III, and good agreement with the experiment is found. A summary and discussion is given in Sec. IV.

II. GENERAL FORMULATION

The configuration we employ is that of an electron beam propagating through an overmoded rectangular waveguide in the presence of a planar wiggler field generated by a magnet array with parabolically tapered pole pieces.^{1,27} As a result, the wiggler field is assumed to be of the form:

$$\begin{aligned} \mathbf{B}_w(\mathbf{x}) = B_w \{ & \cos k_w z \left(\sinh\left[\frac{k_w x}{\sqrt{2}}\right] \sinh\left[\frac{k_w y}{\sqrt{2}}\right] \hat{\mathbf{e}}_z + \cosh\left[\frac{k_w x}{\sqrt{2}}\right] \cosh\left[\frac{k_w y}{\sqrt{2}}\right] \hat{\mathbf{e}}_y \right) \\ & - \sqrt{2} \cosh\left[\frac{k_w x}{\sqrt{2}}\right] \sinh\left[\frac{k_w y}{\sqrt{2}}\right] \sin k_w z \hat{\mathbf{e}}_z \} \end{aligned} \quad (1)$$

where B_w denotes the wiggler amplitude, and $k_w (\equiv 2\pi/\lambda_w)$ is the wiggler wavenumber. The injection of the beam into the wiggler is modeled by an adiabatic increase in the wiggler amplitude over N_w periods. In addition, since the enhancement of the efficiency by means of a tapered wiggler is also studied, the wiggler amplitude will be tapered downward starting at some point z_0 downstream from the entry region in a linear fashion. For this purpose we choose

$$B_w(z) = \begin{cases} B_w \sin^2(k_w z/4N_w) & ; 0 \leq z \leq N_w \lambda_w \\ B_w & ; N_w \lambda_w < z \leq z_0 \\ B_w [1 + \epsilon_w k_w (z - z_0)] & ; z > z_0 \end{cases} \quad (2)$$

where

$$\epsilon_w \equiv \frac{1}{k_w} \frac{d}{dz} \ell n B_w \quad (3)$$

describes the slope of the taper. Since the fringing fields associated with the tapered wiggler amplitude are neglected, this representation requires the slopes of the taper to be small (i.e., N_w must be large and $|\epsilon_w| \ll 1$).

The boundary conditions at the waveguide wall may be satisfied by expanding the vector potential in terms of the orthogonal basis functions of the vacuum waveguide. Thus, we write the vector potential of the radiation in the form

$$\delta \mathbf{A}(\mathbf{x}, t) = \sum_{\ell, n=0}^{\infty \prime} \delta A_{\ell n}(z) \mathbf{e}_{\ell n}^{(1)}(x, y) \cos \alpha \quad (4)$$

for the TE modes, and

$$\delta \mathbf{A}(\mathbf{x}, t) = \sum_{\ell, n=1}^{\infty} \delta A_{\ell n}(z) \left[\mathbf{e}_{\ell n}^{(2)}(x, y) \cos \alpha + \frac{k_{\ell n}}{k} \sin\left(\frac{\ell \pi X}{a}\right) \sin\left(\frac{n \pi Y}{b}\right) \sin \alpha \hat{\mathbf{e}}_z \right] \quad (5)$$

for the TM modes, where for frequency ω and wavenumber $k(z)$

$$\alpha \equiv \int_0^z dz' k(z') - \omega t \quad (6)$$

In addition, \sum' indicates that ℓ and n are not both zero, and

$$\hat{\mathbf{e}}_{\ell, n}^{(1)}(x, y) \equiv \frac{n \pi}{k_{\ell n} b} \cos\left(\frac{\ell \pi X}{a}\right) \sin\left(\frac{n \pi Y}{b}\right) \hat{\mathbf{e}}_z - \frac{\ell \pi}{k_{\ell n} a} \sin\left(\frac{\ell \pi X}{a}\right) \cos\left(\frac{n \pi Y}{b}\right) \hat{\mathbf{e}}_y \quad (7)$$

$$\mathbf{e}_{\ell n}^{(2)}(x, y) \equiv \frac{\ell\pi}{k_{\ell n} a} \cos\left(\frac{\ell\pi X}{a}\right) \sin\left(\frac{n\pi Y}{b}\right) \hat{\mathbf{e}}_x + \frac{n\pi}{k_{\ell n} b} \sin\left(\frac{\ell\pi X}{a}\right) \cos\left(\frac{n\pi Y}{b}\right) \hat{\mathbf{e}}_y \quad (8)$$

are the polarization vectors. In this representation, the waveguide is assumed to be centered at the origin and bounded by $-a/2 \leq x \leq a/2$ and $-b/2 \leq y \leq b/2$. As a consequence, $X \equiv x + a/2, Y \equiv y + b/2$, and

$$k_{\ell n} \equiv \pi \left(\frac{\ell^2}{a^2} + \frac{n^2}{b^2} \right)^{1/2} \quad (9)$$

denotes the cutoff wavevector. It is implicitly assumed that both $\delta A_{\ell n}(z)$ and $k(z)$ vary slowly over a wave period.

The multi-mode treatment includes an arbitrary number of propagating modes of *TE* and/or *TM* polarization. The detailed equations which describe the evolution of the amplitudes and wavenumbers of these modes are identical to those derived in the single-mode analysis,²⁶ and we merely restate the results here. The equations which govern the evolution of the *TE* _{ℓn} mode are

$$\frac{d^2}{dz^2} \delta a_{\ell n} + \left(\frac{\omega^2}{c^2} - k^2 - k_{\ell n}^2 \right) \delta a_{\ell n} = 8 \frac{\omega_b^2}{c^2} F_{\ell n} \left\langle \frac{\cos \alpha}{|v_x|} \mathbf{e}_{\ell n}^{(1)} \cdot \mathbf{v} \right\rangle, \quad (10)$$

and

$$2k^{1/2} \frac{d}{dz} (k^{1/2} \delta a_{\ell n}) = -8 \frac{\omega_b^2}{c^2} F_{\ell n} \left\langle \frac{\sin \alpha}{|v_x|} \mathbf{e}_{\ell n}^{(1)} \cdot \mathbf{v} \right\rangle, \quad (11)$$

where $\delta a_{\ell n} \equiv e \delta A_{\ell n} / mc^2$, $\omega_b^2 \equiv 4\pi n_b e^2 / m$ (where n_b is the bulk density of the beam), \mathbf{v} is the instantaneous electron velocity, and $F_{\ell n} \equiv 1/2$ when either $\ell = 0$ or $n = 0$ and unity otherwise. For the *TM* _{ℓn} mode we obtain a similar result

$$\frac{d^2}{dz^2} \delta a_{\ell n} + \left(1 + \frac{k_{\ell n}^2}{k^2}\right) \left(\frac{\omega^2}{c^2} - k^2 - k_{\ell n}^2\right) \delta a_{\ell n} = 8 \frac{\omega_b^2}{c^2} \times \left\langle \frac{\cos \alpha}{|v_x|} e_{\ell n}^{(2)} \cdot \mathbf{v} + \frac{v_x}{|v_x|} \frac{k_{\ell n}}{k} \sin\left(\frac{\ell \pi X}{a}\right) \sin\left(\frac{n \pi Y}{b}\right) \sin \alpha \right\rangle, \quad (12)$$

and

$$2 \left(k + \frac{k_{\ell n}^2}{k}\right)^{1/2} \frac{d}{dz} \left[\left(k + \frac{k_{\ell n}^2}{k}\right)^{1/2} \delta a_{\ell n}\right] = -8 \frac{\omega_b^2}{c^2} \times \left\langle \frac{\sin \alpha}{|v_x|} e_{\ell n}^{(2)} \cdot \mathbf{v} - \frac{v_x}{|v_x|} \frac{k_{\ell n}}{k} \sin\left(\frac{\ell \pi X}{a}\right) \sin\left(\frac{n \pi Y}{b}\right) \cos \alpha \right\rangle \quad (13)$$

where we note that there is no nontrivial *TM* mode solution when both $\ell = 0$ and $n = 0$.

Equations (10) - (13) are equivalent to a calculation of $\mathbf{J} \cdot \delta \mathbf{E}_{\ell n}$ for each mode. The averaging operator $\langle \dots \rangle$ is defined over the initial conditions of the beam, and includes the effect of an initial momentum spread by means of the distribution function

$$F_o(\mathbf{p}_o) = A \exp[-(p_{x_o} - p_o)^2 / \Delta p_x^2] \delta(p_o^2 - p_{\perp o}^2 - p_{x_o}^2) H(p_{x_o}) \quad (14)$$

where p_o and Δp_x describe the initial bulk momentum and momentum spread, $H(x)$ is the Heaviside function; and the normalization constant is

$$A \equiv \left(\pi \int_0^{p_o} dp_{x_o} \exp[-(p_{x_o} - p_o)^2 / \Delta p_x^2]\right)^{-1} . \quad (15)$$

Observe that this distribution is monoenergetic, but contains a pitch angle spread which describes an axial energy spread given approximately by

$$\frac{\Delta\gamma_z}{\gamma_o} \simeq 1 - [1 + 2(\gamma_o^2 - 1) \frac{\Delta p_x}{p_o}]^{-1/2} , \quad (16)$$

where $\gamma_o \equiv (1 + p_o^2/m^2c^2)^{1/2}$. As a result, the averaging operator takes the form

$$\begin{aligned} \langle(\dots)\rangle &\equiv \frac{A}{2\pi ab} \int_0^{2\pi} d\phi_o \int_0^{p_o} dp_{x_o} \beta_{x_o} \exp[-(p_{x_o} - p_o)^2/\Delta p_x^2] \\ &\times \int_{-\pi}^{\pi} d\psi_o \sigma_{\parallel}(\psi_o) \int_{-a/2}^{a/2} dx_o \int_{-b/2}^{b/2} dy_o \sigma_{\perp}(x_o, y_o) (\dots) \end{aligned} \quad (17)$$

where $\psi_o (\equiv -\omega t_o)$ is the initial ponderomotive phase, $\phi_o \equiv \tan^{-1}(p_{y_o}/p_{z_o})$, $\beta_{x_o} \equiv v_{x_o}/c$, and $\sigma_{\parallel}(\psi_o)$ and $\sigma_{\perp}(x_o, y_o)$ describe the initial beam distributions in phase and cross section.

The phase variation of each mode can be analyzed by the addition of an equation to integrate the relative phase.

$$\Phi(z) \equiv \int_0^z dz' (k(z') - k_o) , \quad (18)$$

where $k_o \equiv (\omega^2/c^2 - k_{z_n}^2)^{1/2}$ is the wavenumber of the vacuum guide. Since the departure of $k(z)$ from the vacuum wavenumber describes the effect of the wave-particle interaction, $\Phi(z)$ represents a measure of the dielectric effect of the FEL interaction. Thus, we integrate the additional equation

$$\frac{d}{dz} \Phi = k - k_0, \quad (19)$$

for each *TE* and *TM* mode.

Each mode will interact resonantly with the electrons and be coupled through the electron motion in the combined wiggler and bulk radiation fields. Thus in order to complete the formulation, the electron orbit equations must also be specified. Since we describe an amplifier model, we choose to integrate in *z*, and write the Lorentz force equations in the form

$$v_z \frac{d}{dz} \mathbf{p} = -e\delta\mathbf{E} - \frac{e}{c} \mathbf{v} \cdot (\mathbf{B}_w + \delta\mathbf{B}) \quad (20)$$

where \mathbf{B}_w is given by Eq. (1) and the radiation fields are given by

$$\delta\mathbf{E} = -\frac{1}{c} \frac{\partial}{\partial t} \sum_{\text{all modes}} \delta\mathbf{A}_{\ell n}, \quad (21)$$

and

$$\delta\mathbf{B} = \nabla \times \sum_{\text{all modes}} \delta\mathbf{A}_{\ell n}. \quad (22)$$

Finally, the electron coordinates obey the equations

$$v_z \frac{d}{dz} x = v_x \quad (23)$$

$$v_z \frac{d}{dz} y = v_y \quad (24)$$

and

$$\frac{d}{dz}\psi = k + k_w - \frac{\omega}{v_x} , \quad (25)$$

which describes the evolution of ponderomotive phase

$$\psi = \psi_0 + \int_0^z dz' \left(k + k_w - \frac{\omega}{v_x} \right) . \quad (26)$$

III. NUMERICAL ANALYSIS

The dynamical equations for the particles and fields described in Sec II are now solved for an overmoded amplifier configuration in which several modes may be in resonance with the beam at a fixed frequency ω . The numerical problem involves the solution of a set of $6N_T + 4N_M$ ordinary differential equations (where N_T is the number of particles, and N_M is the number of modes) as an initial value problem. Observe that equations for the amplitude, growth rate, wavenumber, and phase are integrated for each mode. The integration is accomplished by means of a fourth order Runge-Kutta-Gill technique, and the particle average described in Eq. (17) is performed by an N^{th} order Gaussian quadrature in each of the initial variables. The initial conditions on the fields are chosen to model the injection of an arbitrary power level of each mode, and the initial wavenumbers correspond to the vacuum state (i.e., $k(z=0) = k_0$). Further, the initial value of the relative phase of each mode is zero, and both the wiggler field and growth rate are initially zero. The initial state of the electron beam is chosen to model the injection of a continuous, axisymmetric electron beam with a uniform cross section so that $\sigma_{\parallel} = 1$ for $-\pi \leq \psi_0 \leq \pi$, and $\sigma_{\perp} = 1$ for $r_0 \leq R_b$. A more detailed description of the procedure is to be found in refs. 22 and 26.

The particular example we consider is that of a 35-GHz amplifier employing an electron beam with an energy of 3.5 MeV, a current of 850A, and an initial radius of 1.0 cm propagating through a waveguide characterized by $a = 9.8\text{cm}$ and $b = 2.9\text{cm}$. Wave-particle resonance is obtained in the vicinity of 35-GHz for a wiggler field of 3.72 kG amplitude and 9.8 cm period, and beam injection is accomplished over an entry length of five wiggler periods. For this choice of parameters three wave modes are resonant; specifically, the TE_{01} , TE_{21} , and TM_{21} modes. The multi-mode results described herein will be compared with a previous single-mode treatment. In addition, the parameters correspond with an experiment conducted by Orzechowski and coworkers,^{9,13} and a comparison of the simulation with the experiment will be given in Sec. IV.

The detailed evolution of the total wave power as a function of axial position is shown in Fig. 1 for an axial energy spread of $\Delta\gamma_s/\gamma_0 = 1.5\%$ on the beam and the injection of a signal at $\omega/ck_w = 11.3(34.6GHz)$ composed of the TE_{01} mode at 50 kW, the TE_{21} mode at 500 W, and the TM_{21} mode at 100 W. As shown in the figure, saturation of the total signal occurs at $k_w z = 96(1.5m)$ at a power level of 201 MW for a total efficiency of $\eta \simeq 6.87\%$. It is also evident that although the TE_{01} mode was the overwhelming dominant mode upon injection, it comprises only about 60% of the signal at saturation. The remaining power is composed primarily of the TE_{21} (at 37% of the signal) with only a relatively small contribution of the TM_{01} mode. As discussed in ref. 26, the reason for this is that at this frequency the growth rate of the TE_{21} mode exceeds that of the TE_{01} mode, and compensates for the lower initial power level. Due to the polarization of the TM_{21} mode, the growth rate and efficiency are smaller than for the TE modes, and the TM_{21} mode never accounts for more than about 7 MW. The rapid oscillation shown in the figure has a period of approximately $\lambda_w/2$ and occurs because the evolution of $\mathbf{J} \cdot \mathbf{E}$ for a planar wiggler exhibits both a slow variation corresponding to the ponderomotive phase and a rapid oscillation at $\lambda_w/2$.²⁶ Observe that the single-mode analysis showed a saturated power of 162 MW for the TE_{01} mode, 126 MW for the TE_{21} mode, and 25 MW for the TM_{21} mode. Thus, while the total power of the signal in the multi-mode analysis somewhat exceeds that shown in the single-mode cases (for the TE modes), the power levels of the individual modes are lower.

The phase variation of each of these modes is shown in Fig. 2 as a function of axial position, where the arrow denotes the point at which the total power saturates. Of these modes, the TE_{01} behaves in qualitatively the same way as in the single-mode case. Specifically, the bulk phase at this frequency (apart from the rapid oscillation at $\lambda_w/2$) increases monotonically with axial position through, and beyond, the saturation point. In contrast, the relative phases of both the TE_{21} and TM_{21} modes are decidedly not monotonic and exhibit a decrease with axial position starting at a point somewhat beyond saturation. This is a multi-mode effect since the relative phases of the TE_{21}

and $TM_{2,1}$ modes also exhibit a monotonic increase with axial position at this frequency in the single-mode analysis. Finally, we observe that the curves of relative phase for the $TE_{2,1}$ and $TM_{2,1}$ modes are almost identical. The reason for this is that the dispersion curves for the $TE_{\ell,n}$ and $TM_{\ell,n}$ modes are degenerate in a rectangular waveguide.

The effect of an initial momentum spread on the saturation efficiency of the total signal and the $TE_{0,1}$ and $TE_{2,1}$ mode components is shown in Fig. 3. The $TM_{2,1}$ mode is excluded from the figure because it composes such a small fraction of the signal. As shown in the figure, the saturation efficiency is relatively insensitive to the axial energy spread over the range $\Delta\gamma_z/\gamma_0 \lesssim 2.5\%$, and decreases from $\eta \simeq 8.6\%$ at $\Delta\gamma_z \simeq 0$ to $\eta \simeq 5.9\%$ at $\Delta\gamma_z/\gamma_0 \simeq 2.5\%$. The reason for this is that the coupling coefficient (and, hence, the growth rate) depends upon the product of the wiggler amplitude and period. Since this product is large for the present choice of parameters, the growth rate is large and the interaction can accept a relatively large axial energy spread without suffering a severe degradation.

The saturation efficiency is known to scale as the cube root of the beam current at the frequency of peak growth from the idealized one-dimensional theory of the high-gain Compton (i.e., the strong-pump) regime, and this type of scaling law was also found from the three-dimensional single-mode simulation of this configuration. The scaling of the total power as a function of beam current for the multi-mode analysis is shown in Fig. 4 for $\Delta\gamma_z = 0$ and $\Delta\gamma_z/\gamma_0 = 1\%$, the efficiency is found to scale approximately as $\eta \sim I_b^{1/3}$.

Turning to the question of the enhancement of the efficiency by means of a tapered wiggler, we plot the evolution of the power with axial position in Fig. 5 for parameters corresponding to those shown in Fig. 1. The optimal start-taper point for this case is $k_w z_0 = 86$, and we choose a slope of $\epsilon_w = -0.007$ which was also studied for the single-mode analysis. The central conclusion to be drawn from the figure is that it is possible to selectively enhance the $TE_{0,1}$ mode. The uniform wiggler interaction for this example yields a total efficiency of 6.8%, of which the $TE_{0,1}$ mode comprises only 60%

of the signal. By contrast, careful choice of both the start-taper point and the slope of the taper show that the efficiency can be enhanced to $\eta_{max} \simeq 41.29\%$ (if the wiggler field is tapered to zero) with 99% of the power in the TE_{01} mode. Both the TE_{21} and TM_{21} (not shown in the figure) ultimately decay to extremely low intensities. One surprising result of the present multi-mode analysis is that the maximum efficiency to be obtained by tapered wiggler fields is enhanced relative to the single-mode analysis. By comparison, the single-mode analysis for these parameters yields a maximum efficiency of $\eta_{max} \simeq 34\%$ which is substantially lower than the 41.29% found in the multi-mode simulation. The phase variation of the TE_{01} mode for this example is shown in Fig. 6, and exhibits the same qualitative variation as in the single-mode analysis. Another characteristic of the tapered wiggler interaction observed in the single-mode treatment is that the overall efficiency appears to be relatively insensitive to the axial energy spread. As shown in Fig. 7, in which we plot the maximum obtainable efficiency versus $\Delta\gamma_z/\gamma_0$, this is also found to be the case in the multi-mode analysis. As shown in the figure, the maximum efficiency decreases from 43.6% at $\gamma_z = 0$ to as much as 39.4% at $\Delta\gamma_z/\gamma_0 = 2\%$. This is a much lower proportional sensitivity to the axial energy spread than is illustrated in Fig. 3 for the uniform wiggler case.

Finally, we address the question of the sensitivity of the tapered wiggler interaction to fluctuations in the bulk energy of the beam. The reason for concern with this issue is that the tapered wiggler interaction is known to be sensitive to the start-taper point. In particular, the taper should begin at a point shortly prior to saturation (for the untapered wiggler) corresponding to the trapping of the bulk of the beam in the ponderomotive potential. Changes, or fluctuations, in the beam energy at fixed frequency are equivalent to variation of the frequency at fixed energy, and result in shifts in the growth rate and saturation point. For this reason, it might be expected that the tapered wiggler interaction is sensitive to fluctuations in the bulk energy of the beam. In order to address this question, the variation in the efficiency has been studied as a function of beam energy, and the results are shown in Fig. 8. For convenience, this figure has been generated for the limiting case of zero axial energy spread for which the

optimal start-taper point is $k_w z_o = 83$ at a beam energy of 3.5 MeV. Hence, choosing $\epsilon_w = -0.007$ and the aforementioned start-taper point, Fig. 8 describes the variation in the efficiency with beam energy when (1) the wiggler is tapered to zero ($\Delta B_w / B_w = 1$), and (2) when the wiggler is tapered to half its ambient level ($\Delta B_w / B_w = 0.5$). As shown in the figure, there is a sharp decline in the efficiency above approximately 3.55 MeV. In contrast, there is a more gradual decrease in the efficiency for energies down to 3.3 MeV, below which the resonant interaction at $\omega / ck_w = 11.3$ is lost. As a result, the tapered wiggler interaction will tolerate a bulk energy fluctuation of the order of 8.6 % for these parameters without severe degradation in performance for these parameters.

IV. SUMMARY AND DISCUSSION

In this paper, a multi-mode analysis and simulation of FEL amplifiers in three-dimensions has been given for a configuration in which a relativistic electron beam propagates through an overmoded rectangular waveguide in the presence of a planar wiggler generated by means of an array of magnets with tapered pole pieces. The multi-mode analysis is accomplished by expansion of the radiation field in terms of the vacuum waveguide modes, and an arbitrary number of propagating TE and/or TM modes is included in the analysis. Although multiple modes are included in the analysis, the problem of interest is that of an amplifier and single frequency propagation is considered. As a result, the field equations are averaged over a wave period in order to eliminate the fast-time scale phenomena. However, no average of the orbit equations was performed, and the electron dynamics were treated by means of the fully three-dimensional Lorentz force equations. As a result, the effects of the adiabatic injection process, bulk wiggler motion, Betatron oscillations, velocity shear, beam focussing due to the wiggler gradients, and phase trapping of the beam in the ponderomotive potential formed by the beating of the wiggler and radiation fields, are all included in a self-consistent manner.

The numerical example describes a 35-GHz amplifier which employs a 3.5 MeV/850A electron beam with a 1.0 cm initial radius propagating through a rectangular waveguide with dimensions $a = 9.8\text{cm}$ and $b = 2.9\text{cm}$ in the presence of a wiggler field with a 3.72 kG amplitude and 9.8cm period. Three distinct wave modes are found to be resonant; specifically, the TE_{01} , TE_{21} , and TM_{21} modes. The simulation is carried out under the assumption that the injected signal consists primarily of the TE_{01} mode at a 50kW power level, the TE_{21} mode at 500W, and the TM_{21} mode at 100W. Results indicate that although the TE_{21} mode was at a relatively low initial power level, it comprises upwards of 37% of the saturated signal. The coupling between the beam and the TM_{21} mode was weaker than for the TE modes, and never accounted for more than a few percent of the total signal. Comparison with a previous single-mode

analysis²⁶ indicates that the efficiency of the total signal is somewhat higher than that found for single modes in the case of a uniform wiggler. A more dramatic difference between the multi-mode and single-mode treatments is found for a tapered wiggler interaction. In this case, it is found that the selective enhancement of the TE_{01} mode is possible and, indeed, has been experimentally observed.¹³ However, the power levels to be obtained in the TE_{01} mode through the multi-mode tapered wiggler interaction were found to be substantially higher than found in the single-mode simulation. This constitutes an important question for future study.

The configuration and parameters described in this paper nominally correspond to the experiment performed by Orzechowski and coworkers.^{9,13} The principal differences between the analytical configuration and the experiment are that in the experiment (1) the beam was injected into the wiggler through an entry taper region one wiggler period long, and (2) a quadrupole field was used to provide additional electron focussing instead of parabolically tapered pole pieces. Since the fringing fields associated with the wiggler field in the entry taper region are not included in the analytical model, it would be invalid to apply the analysis for $N_w = 1$. However, the choice of $N_w = 5$ is made as a compromise and gives good agreement with experiment subject to the additional assumption of an axial energy spread of $\Delta\gamma_z/\gamma_0 = 1.5\%$. This is within an upper bound of 2% on the axial energy spread established by means of an electron spectrometer measurement.²⁸ The experimental measurement for a uniform wiggler interaction resulted in a saturated power level of 180 MW over a length of 1.3m. As shown by Fig. 1, the simulation gives a peak power of 204MW which, if we average over the fast $\lambda_w/2$ oscillation, is reduced to 185 MW. Given the experimental uncertainties in high power measurements, the latter figure is more relevant for comparison and is in substantial agreement with the experiment. The saturation length found from simulation (that is, the length of the uniform wiggler region plus one wiggler period to account for the entry taper region) is 1.1m, which is also in good agreement with the experiment. Note that rapid oscillation in the power and relative phase at a period of $\lambda_w/2$ is likely to introduce a 10-20% uncertainty in the measurement of these quantities.

A comparison can also be made with the tapered wiggler experiment¹³ in which the wiggler field was decreased by 55% ($\Delta B_w/B_w = 0.55$) over a length of 1.1m (i.e., $\epsilon_w = -0.0078$) and the efficiency was found to increase to 34% for a total power of 1 GW. The evolution of the total signal power, and that of the TE modes, is shown in Fig. 9 for parameters consistent with the tapered wiggler experiment (the optimal start-taper point found in simulation was $k_w z_o = 86$). As shown in the figure, the maximum efficiency obtained by tapering the wiggler field to zero is approximately 40.6%, of which more than 95% of the power is contained in the TE_{01} mode. However, over a length of only 1.1m beyond the start-taper point (i.e., $k_w z - k_w z_o = 70.5$) the efficiency is 34%, of which approximately 90% of the power is in the TE_{01} mode. The evolution of the relative phase for this case is shown in Fig. 10, in which the relative phase saturates at a value in the neighborhood of 120° downstream from the start-taper point. This is in good agreement with reported measurements of the evolution of the relative phase in the tapered wiggler experiment.²⁹ Thus, within the uncertainties imposed by the choices of N_w and $\Delta\gamma_z$, the nonlinear analysis is found to be in good agreement with the experimental measurements for both uniform and tapered wiggler interactions.

ACKNOWLEDGMENTS

This research was supported by the Office of Naval Research and the Office of Naval Technology. The author would like to thank Dr. A.K. Ganguly, Dr. R.K. Parker and Dr. R.H. Jackson for helpful discussions.

REFERENCES

1. R.M. Phillips, IRE Trans. Electron Devices 7, 231 (1960).
2. V.L. Granatstein, S.P. Schlesinger, M. Herndon, R.K. Parker, and J.A. Pasour, Appl. Phys. Lett. 30, 384 (1977).
3. D.B. McDermott, T.C. Marshall, S.P. Schlesinger, R.K. Parker, and V.L. Granatstein, Phys. Rev. Lett. 41, 1368 (1978).
4. R.K. Parker, R.H. Jackson, S.H. Gold, H.P. Freund, V.L. Granatstein, P.C. Efthimion, M. Herndon, and A.K. Kinkead, Phys. Rev. Lett. 48, 238 (1982).
5. J. Fajans, G. Bekefi, Y.Z. Yin, and B. Lax, Phys. Rev. Lett. 53, 246 (1984).
6. J.A. Pasour, R.F. Lucey, and C.W. Roberson, in Free-Electron Generators of Coherent Radiation, edited by C.A. Brau, S.F. Jacobs, and M.O. Scully [Proc. SPIE 453, 328 (1984)].
7. J.A. Pasour, R.F. Lucey, and C.A. Kzpetanakos, Phys. Rev. Lett. 53, 1728 (1984).
8. S.H. Gold, D.L. Hardesty, A.K. Kinkead, L.R. Barnett, and V.L. Granatstein, Phys. Rev. Lett. 52, 1218 (1984).
9. T.J. Orzechowski, B. Anderson, W.M. Fawley, D. Prosnitz, E.T. Scharlemann, S. Yarema, D. Hopkins, A.C. Paul, A.M. Sessler, and J. Wurtele, Phys. Rev. Lett. 54, 889 (1985).
10. J. Fajans, G. Bekefi, Y.Z. Yin, and B. Lax, Phys. Fluids 28, 1995 (1985).
11. J. Masud, T.C. Marshall, S.P. Schlesinger, and F.G. Yee, Phys. Rev. Lett. 56, 1567 (1986).

12. J. Fajans, J. Wurtele, G. Bekefi, D.S. Knowles, and K. Xu, Phys. Rev. Lett. 57, 579 (1986).
13. T.J. Orzechowski, B. Anderson, J.C. Clark, W.M. Fawley, A.C. Paul, D. Prosnitz, E.T. Scharlemann, S. Yarema, D.B. Hopkins, A.M. Sessler, and J. Wurtele, Phys. Rev. Lett. 57, 2172 (1986).
14. L.R. Elias, W.M. Fairbanks, J.M.J. Madey, H.A. Schwettman, and T.I. Smith, Phys. Rev. Lett. 36, 717 (1976).
15. D.A.G. Deacon, L.R. Elias, J.M.J. Madey, G.J. Ramian, H.A. Schwettman, and T.I. Smith, Phys. Rev. Lett. 38, 892 (1977).
16. R.W. Warren, B.E. Newnam, J.G. Winston, W.E. Stein, L.M. Young, and C.A. Brau, IEEE J. Quantum Electron. QE-19, 391 (1983).
17. M. Billandon, P. Ellaume, J.M. Ortega, C. Bazin, M. Bergher, M. Velghe, Y. Petroff, D.A.G. Deacon, K.E. Robinson, and J.M.J. Madey, Phys. Rev. Lett. 51, 1652 (1983).
18. J.M. Slater, J.L. Adamski, D.C. Quimby, T.L. Churchill, L.Y. Nelson, and R.E. Center, IEEE J. Quantum Electron. QE-19, 374 (1983).
19. J.A. Edighoffer, G.R. Neil, C.E. Hess, T.I. Smith, S.W. Fornaca, and H.A. Schwettman, Phys. Rev. Lett. 52, 344 (1984).
20. B.E. Newnam, R.W. Warren, R.L. Sheffield, W.E. Stein, M.T. Lynch, J.S. Fraser, J.C. Goldstein, J.E. Sollid, T.A. Swann, J.M. Watson, and C.A. Brau, IEEE J. Quantum Electron. QE-21, 867 (1985).
21. C.R. Pidgeon, S.D. Smith, W.J. Firth, D.A. Jorosynski, D.M. Tratt, J.S. Mackay, M.F. Kimmitt, J.M. Reid, M.G. Kelliher, M.W. Poole, G. Saxon, R.P. Walker, W.A. Gillespie, and P.F. Martin, IEEE J. Quantum Electron. QE-21, 1083 (1985).

22. A.K. Ganguly and H.P. Freund, Phys. Rev. A 32, 2275 (1985).
23. H.P. Freund and A.K. Ganguly, Phys. Rev. A 33, 1060 (1986).
24. H.P. Freund and A.K. Ganguly, Phys. Rev. A 34, 1242 (1986).
25. H.P. Freund and A.K. Ganguly, IEEE J. Quantum Electron. QE-23, 1657, (1987).
26. H.P. Freund, H. Bluem, and C.-L. Chang, Phys. Rev. A 36, 2182 (1987).
27. E.T. Scharlemann, J. Appl. Phys. 58, 2154 (1985).
28. T.J. Orzechowski, personal communication.
29. T.J. Orzechowski, E.T. Scharlemann, and D.B. Hopkins, Phys. Rev. A 35, 2184 (1987).

FIGURE CAPTIONS

- Fig. 1 The evolution of the wave power (both total and TE_{01} mode) with axial position.
- Fig. 2 Plots of the evolution of the relative phase versus axial position for (a) the TE_{01} mode, (b) the TE_{21} mode, and (c) the TM_{21} mode.
- Fig. 3 Variations of the saturation efficiencies of the total signal and the TE modes versus axia. energy spread.
- Fig. 4 Graph showing the scaling of the efficiency of the total signal with beam current for $\Delta\gamma_z/\gamma_0 = 0$ and 1%.
- Fig. 5 Plot showing the evolution of the total signal and the TE modes for a tapered wiggler interaction characterized by $\epsilon_w = -0.007$ and $k_w z_0 = 86$.
- Fig. 6 Graph of the evolution of the relative phase of the TE_{01} mode during the course of the tapered wiggler interaction.
- Fig. 7 Illustration of the effect of an axial energy spread on the tapered wiggler interaction. Observe that each point corresponds to the optimal start-taper point of the associated $\Delta\gamma_z$.
- Fig. 8 The variation in the efficiency of the tapered wiggler interaction with fluctuations in the bulk energy of the beam.
- Fig. 9 Plot of the evolution of the total signal and the TE modes for a tapered wiggler characterized by $\epsilon_w = -0.0078$ and $k_w z_0 = 86$.
- Fig. 10 Graph of the evolution of the relative phase for a tapered wiggler interaction characterized by $\epsilon_w = -0.0078$ and $k_w z_0 = 86$.

(a = 9.8 cm; b = 2.9 cm; $\omega/ck_w = 11.3$)

$V_b = 3.5 \text{ MeV}$
 $I_b = 850 \text{ A}$
 $R_b = 1.0 \text{ cm}$
 $\frac{\Delta Y_z}{Y_0} = 1.5\%$
 $B_w = 3.72 \text{ kG}$
 $\lambda_w = 9.8 \text{ cm}$
 $N_w = 5$

Mode	$P_{in}(W)$
TE ₀₁	50,000
TE ₂₁	500
TM ₂₁	100

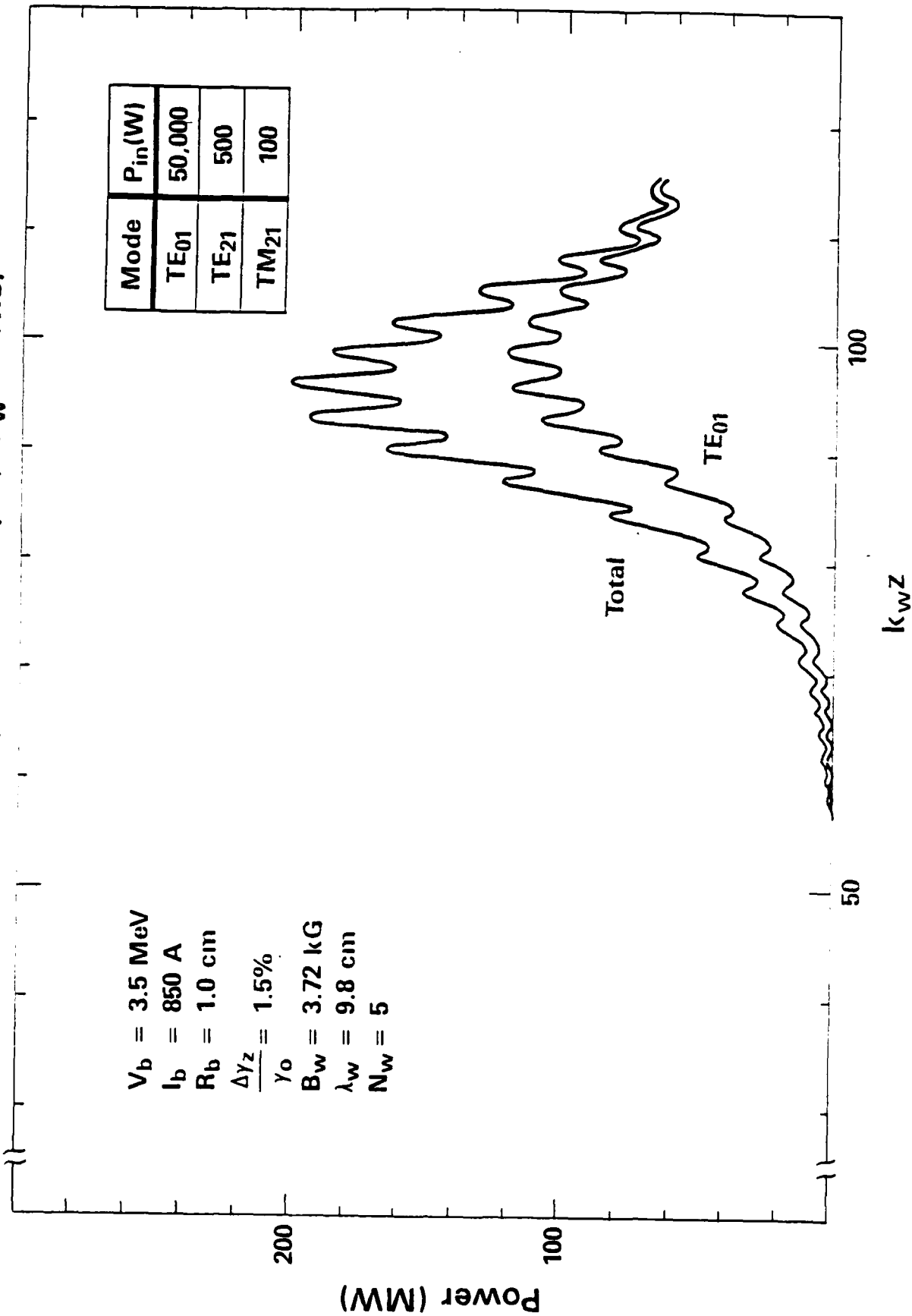


Fig. 1

(a = 9.8 cm; b = 2.9 cm; $\omega/ck_w = 11.3$)

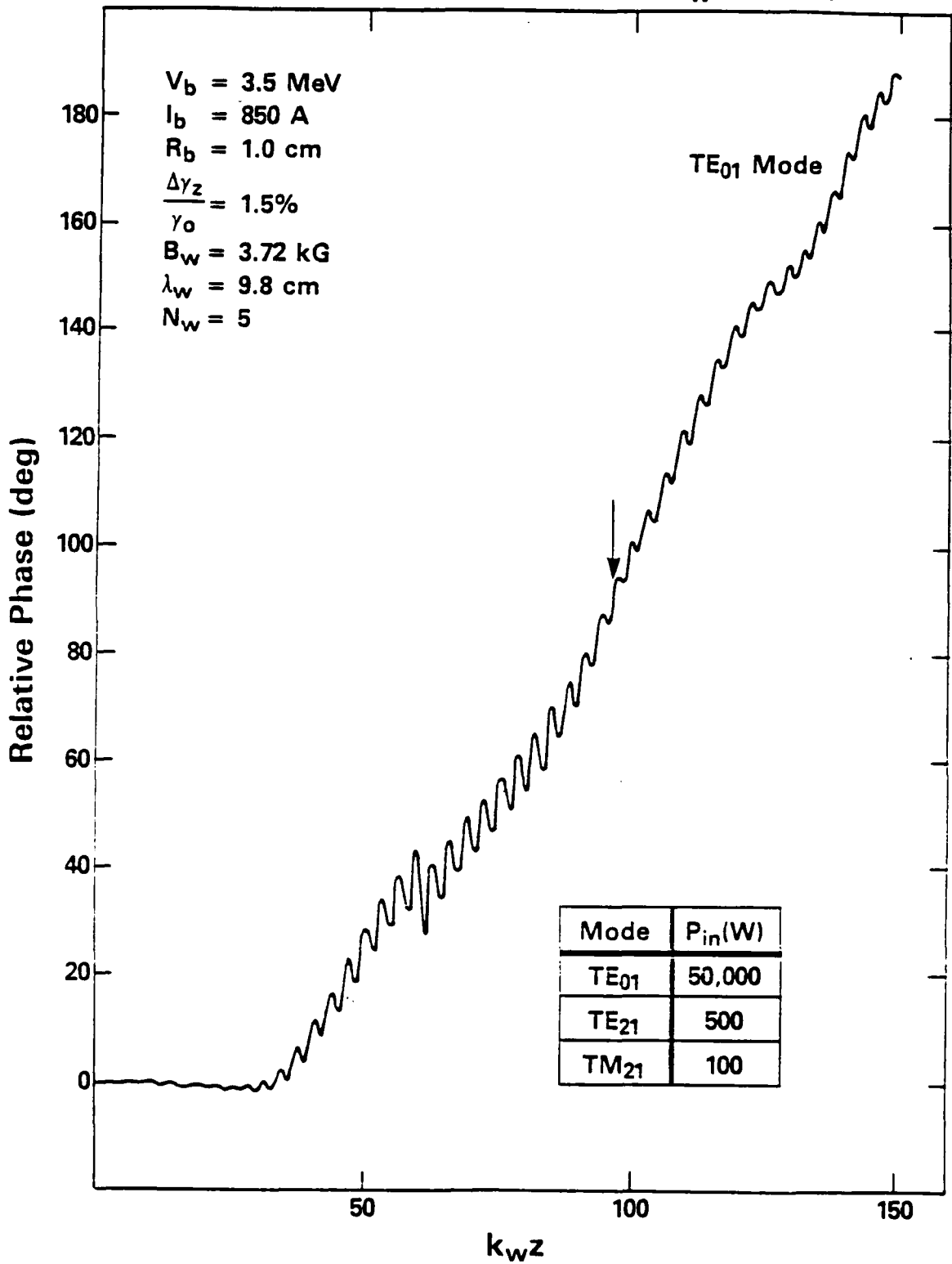


Fig. 2a

(a = 9.8 cm; b = 2.9 cm; $\omega/ck_w = 11.3$)

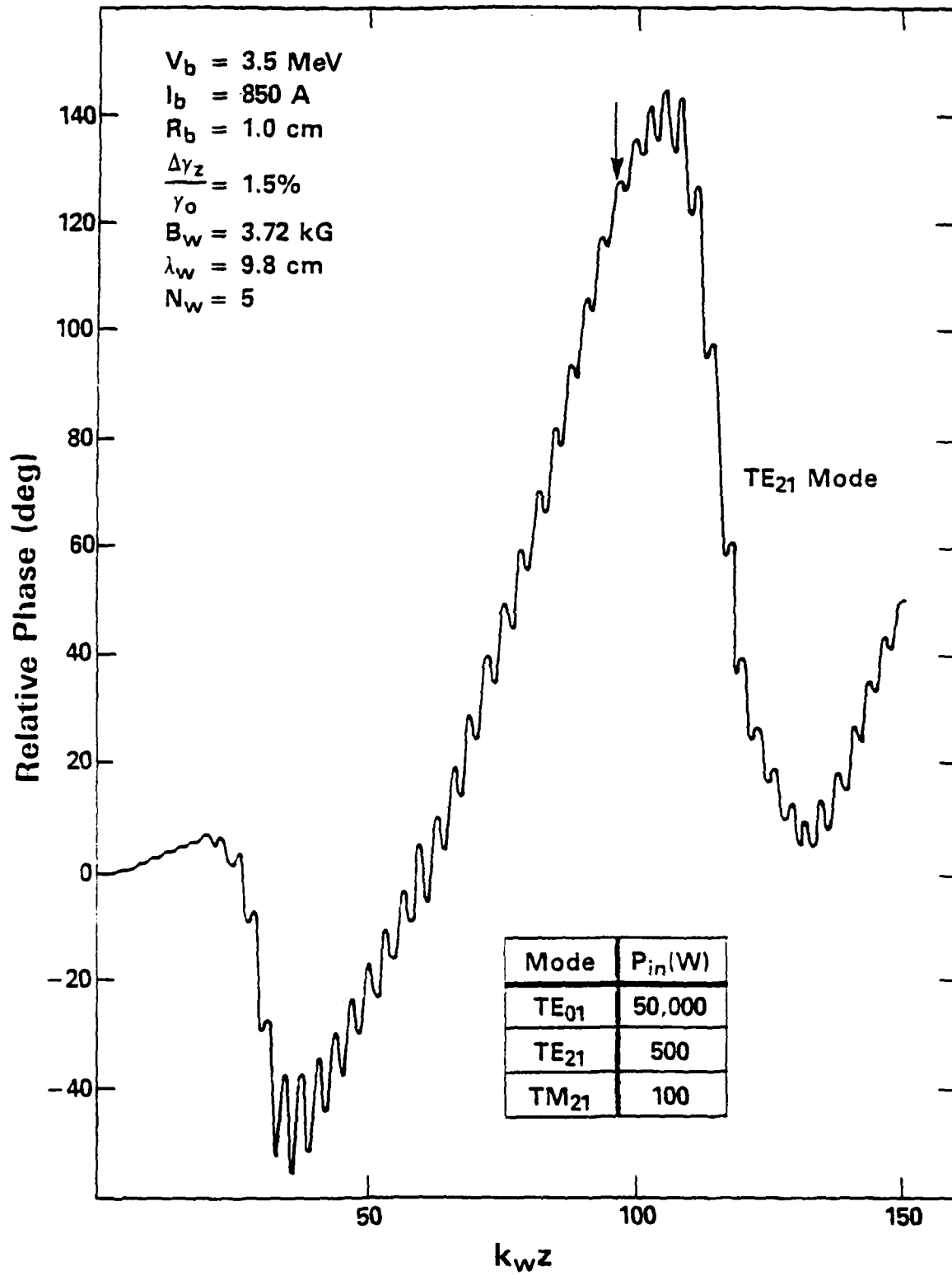


Fig. 2b

(a = 9.8 cm; b = 2.9 cm; $\omega/ck_w = 11.3$)

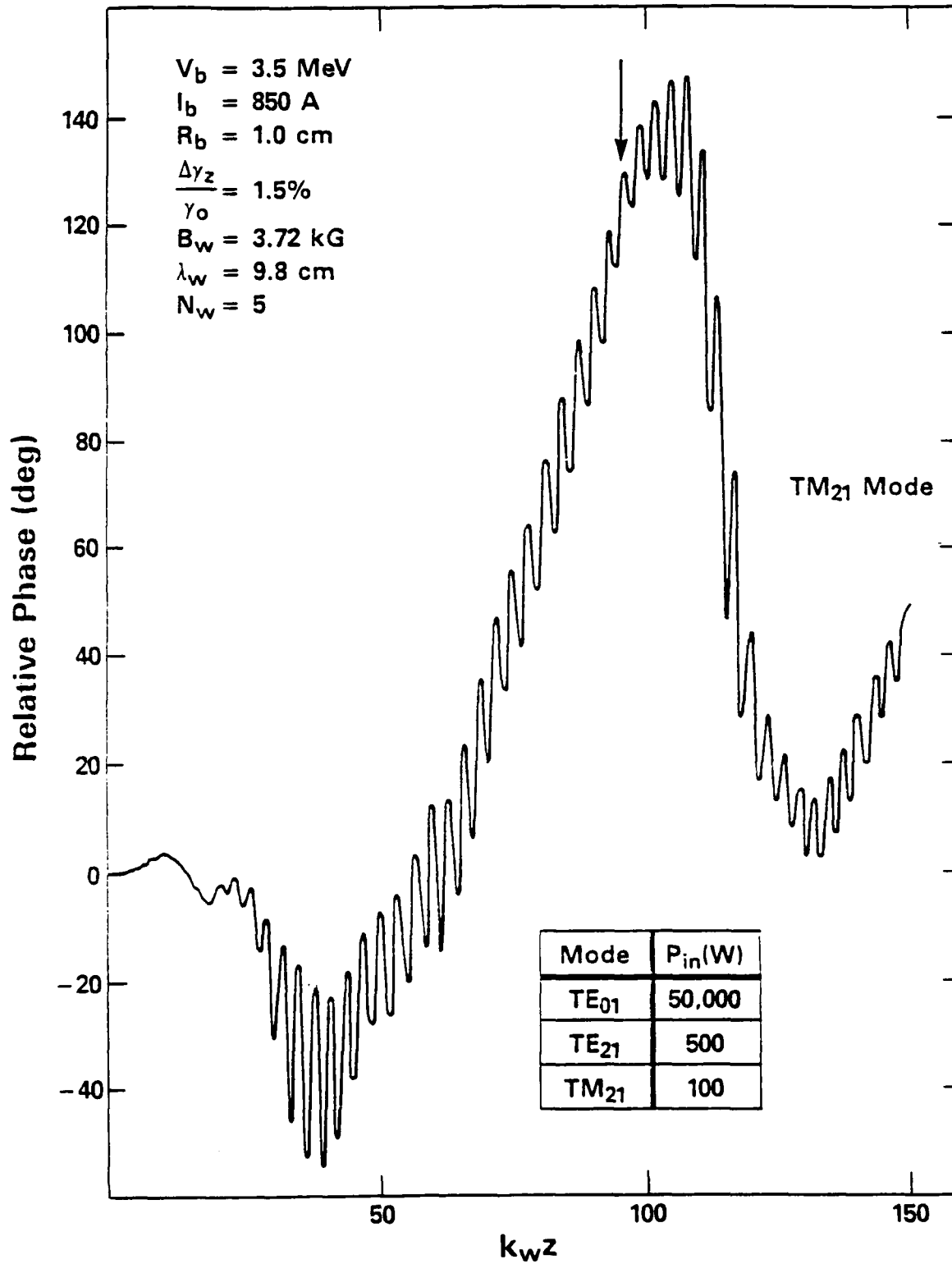


Fig. 2c

(a = 9.8 cm; b = 2.9 cm; $\omega/ck_w = 11.3$)

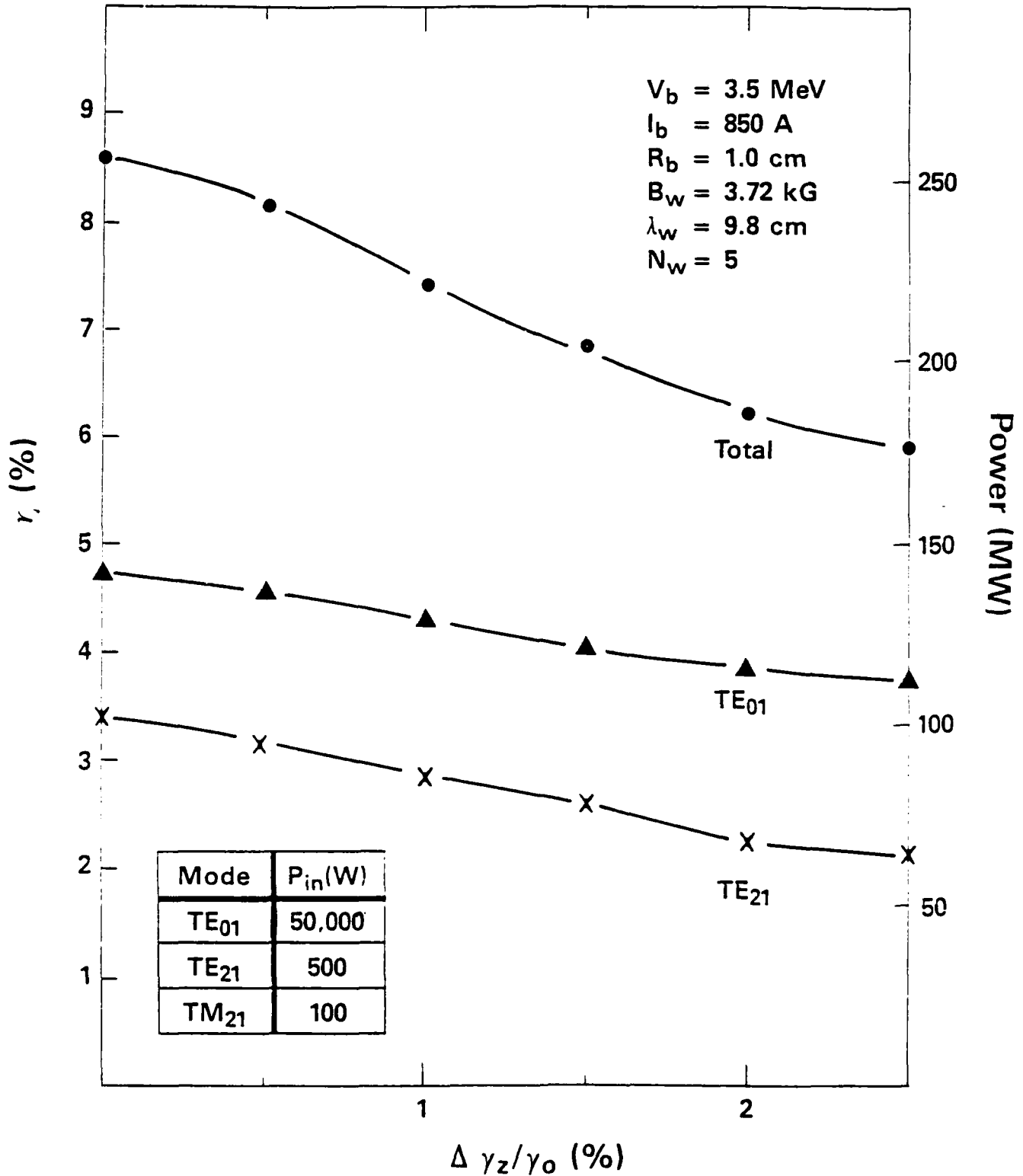


Fig. 3

(a = 9.8 cm; b = 2.9 cm; $\omega/ck_w = 11.3$)

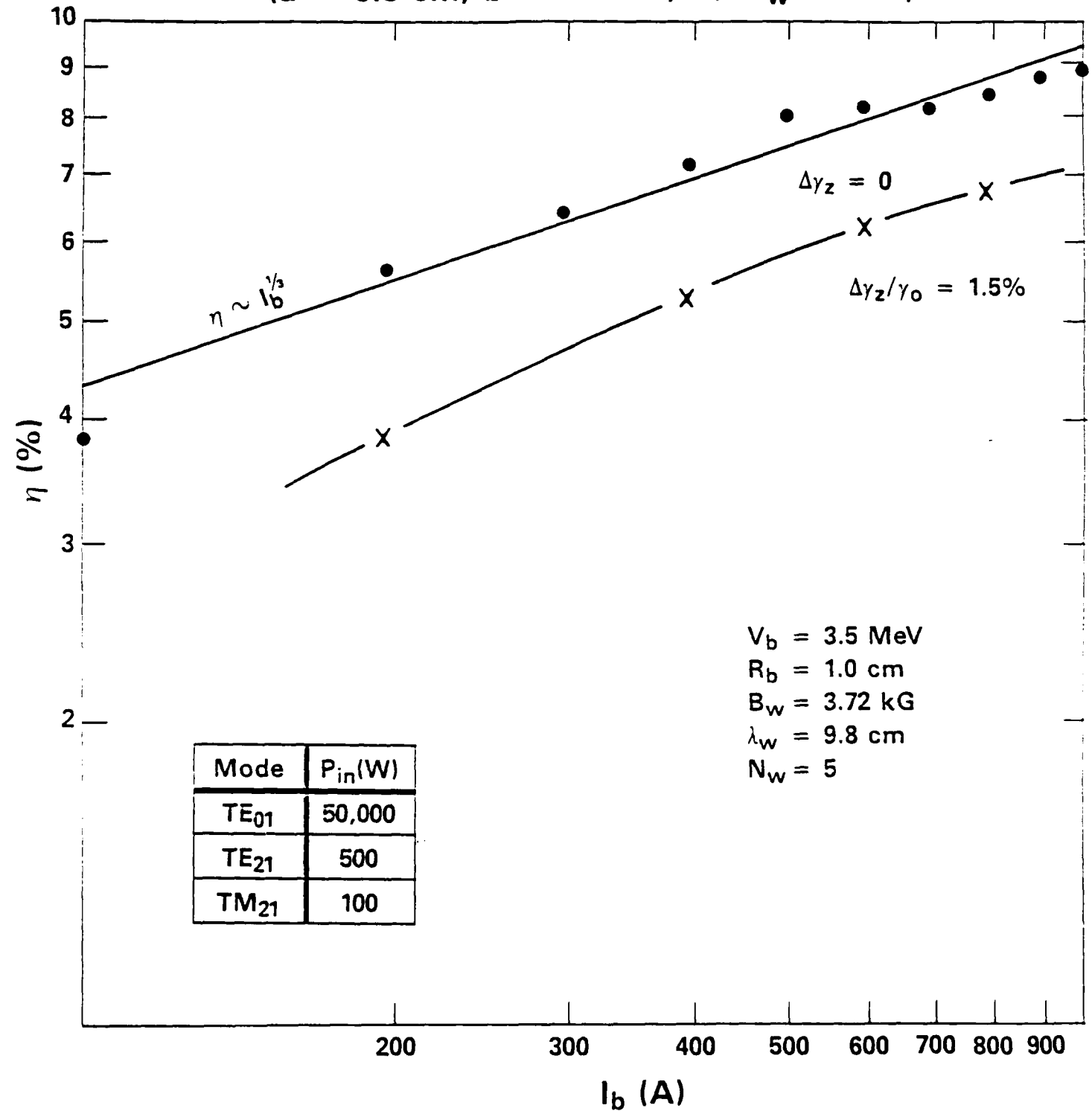


Fig. 4

$a = 9.8 \text{ cm}; b = 2.9 \text{ cm}; \omega/ck_w = 11.3 \text{ (34.6 GHz)}$

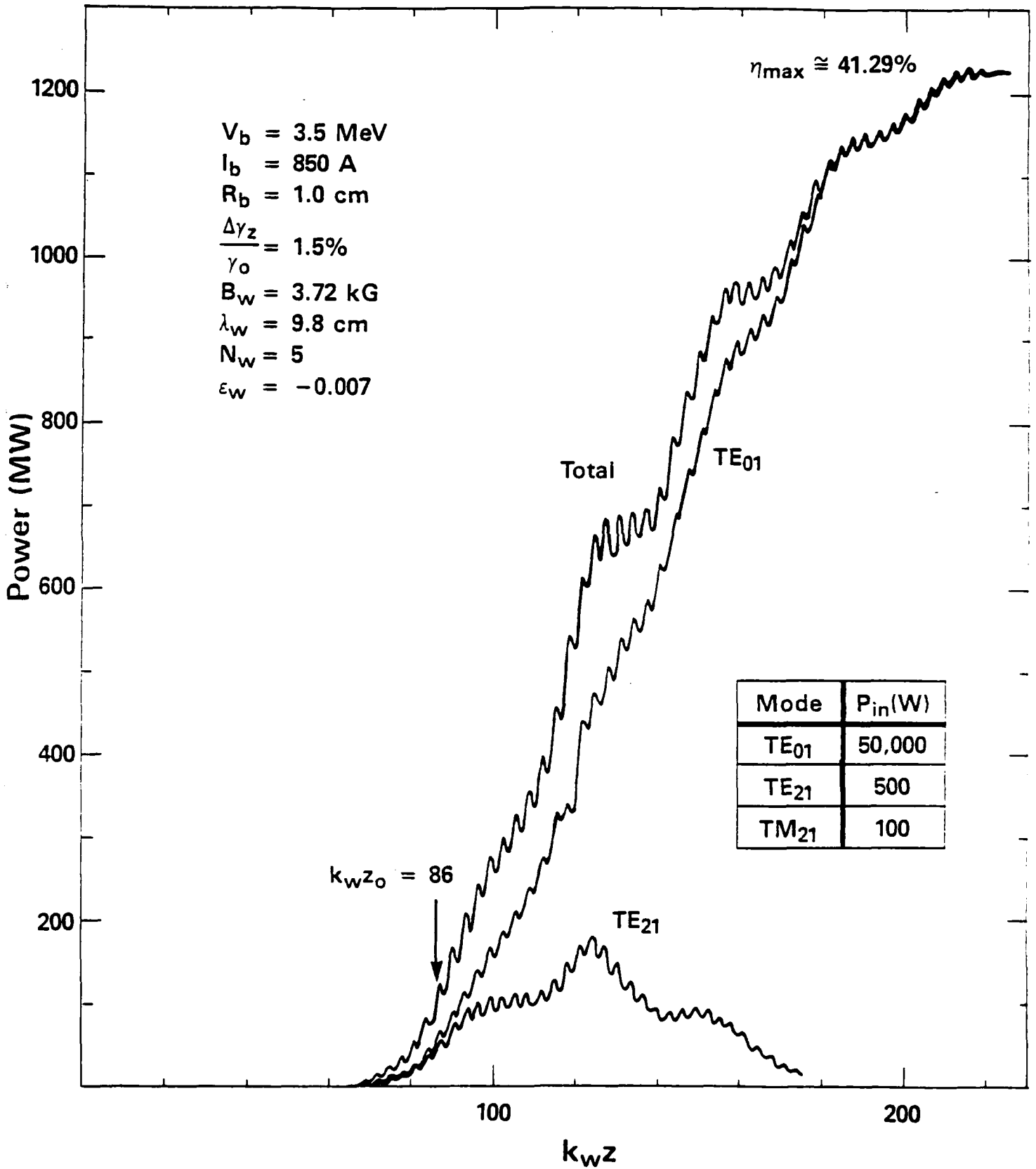
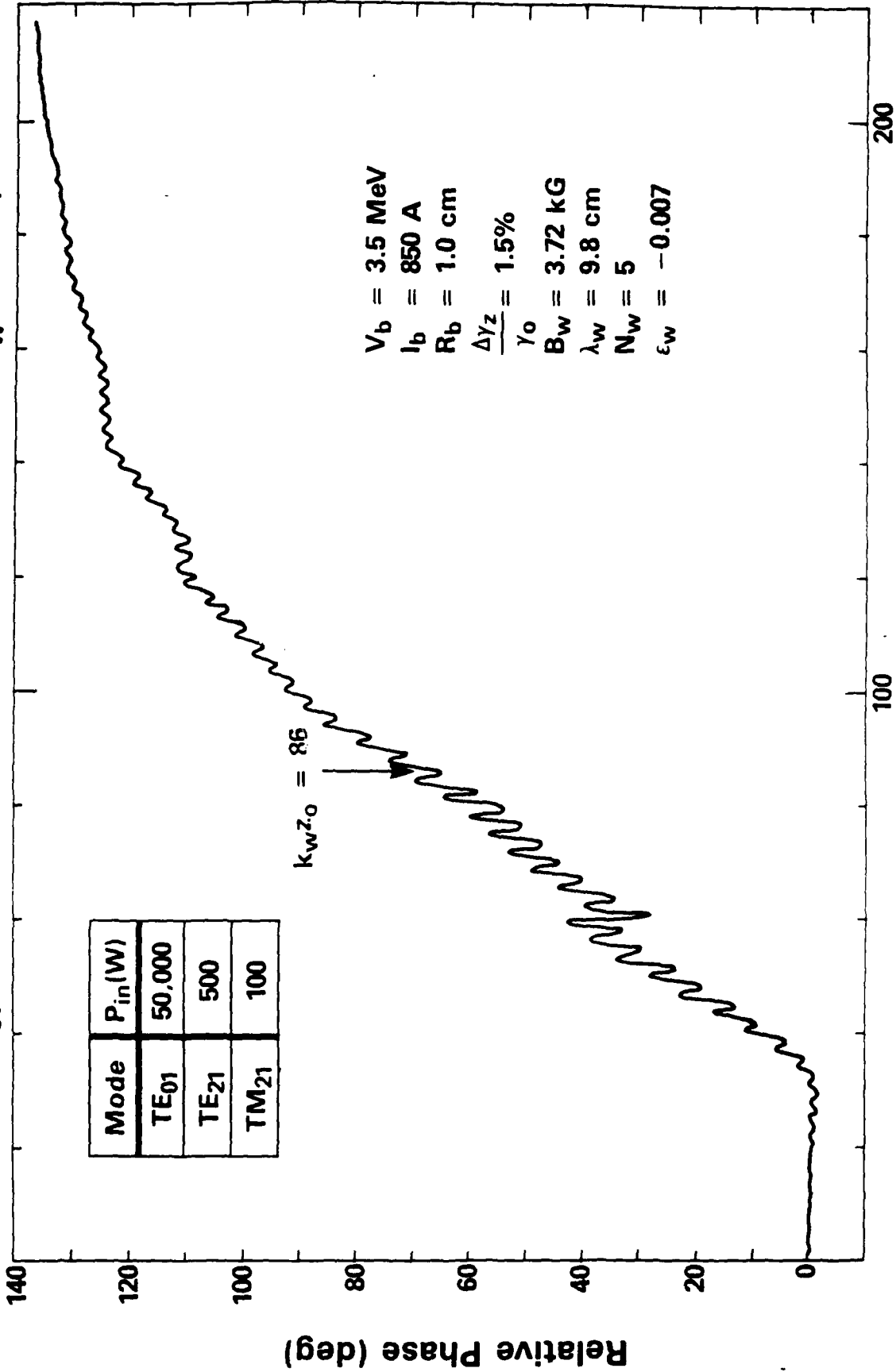


Fig. 5

TE₀₁ Mode (a = 9.8 cm; b = 2.9 cm; $\omega/ck_w = 11.3$)



Mode	$P_{in}(W)$
TE ₀₁	50,000
TE ₂₁	500
TM ₂₁	100

$V_b = 3.5 \text{ MeV}$
 $I_b = 850 \text{ A}$
 $R_b = 1.0 \text{ cm}$
 $\frac{\Delta Y_z}{\gamma_0} = 1.5\%$
 $B_w = 3.72 \text{ kG}$
 $\lambda_w = 9.8 \text{ cm}$
 $N_w = 5$
 $\epsilon_w = -0.007$

$k_w z$

Fig. 6

TE₀₁ Mode (a = 9.8 cm; b = 2.9 cm; $\omega/ck_w = 11.3$)

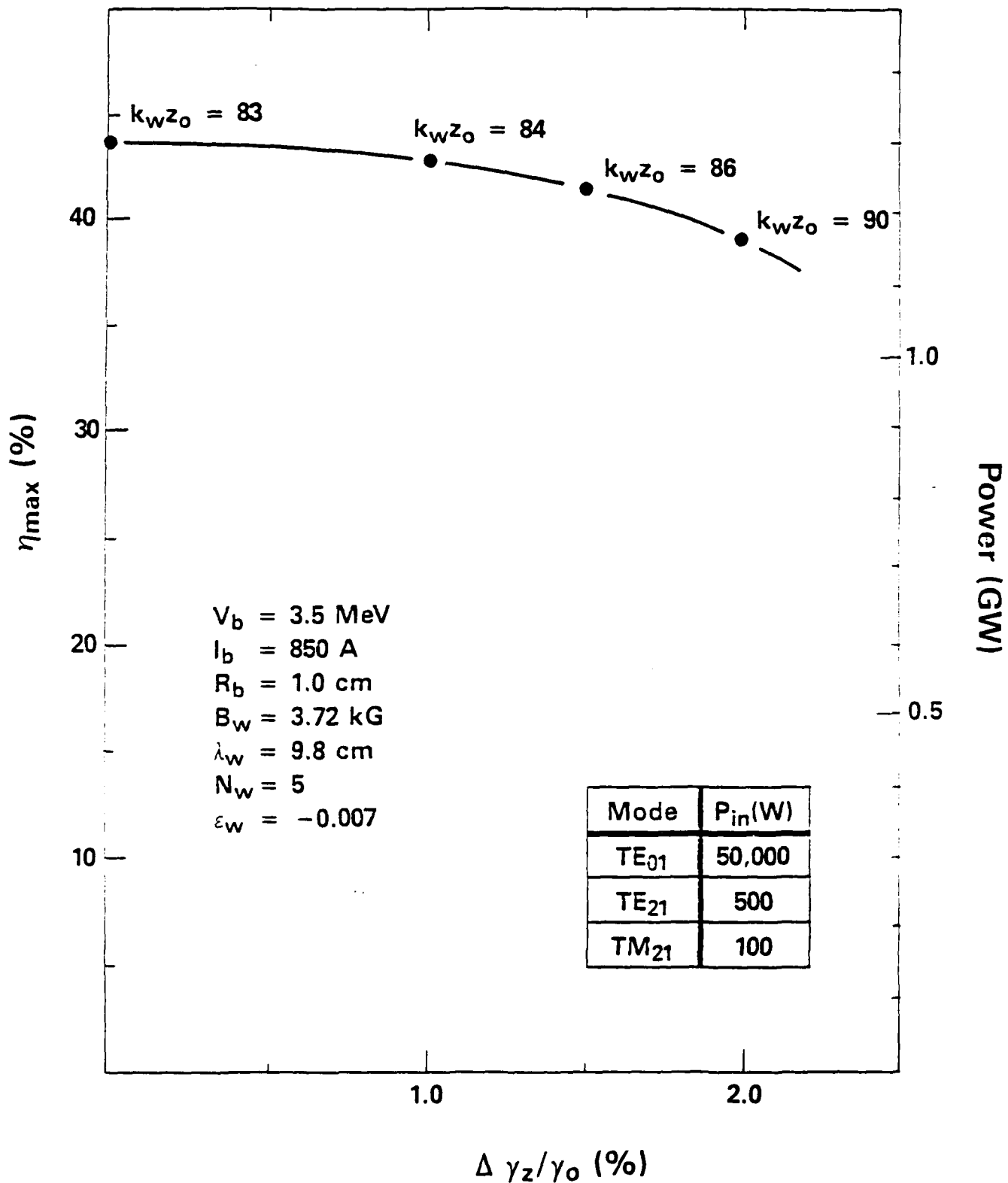


Fig. 7

(a = 9.8 cm; b = 2.9 cm; $\omega/ck_w = 11.3$)

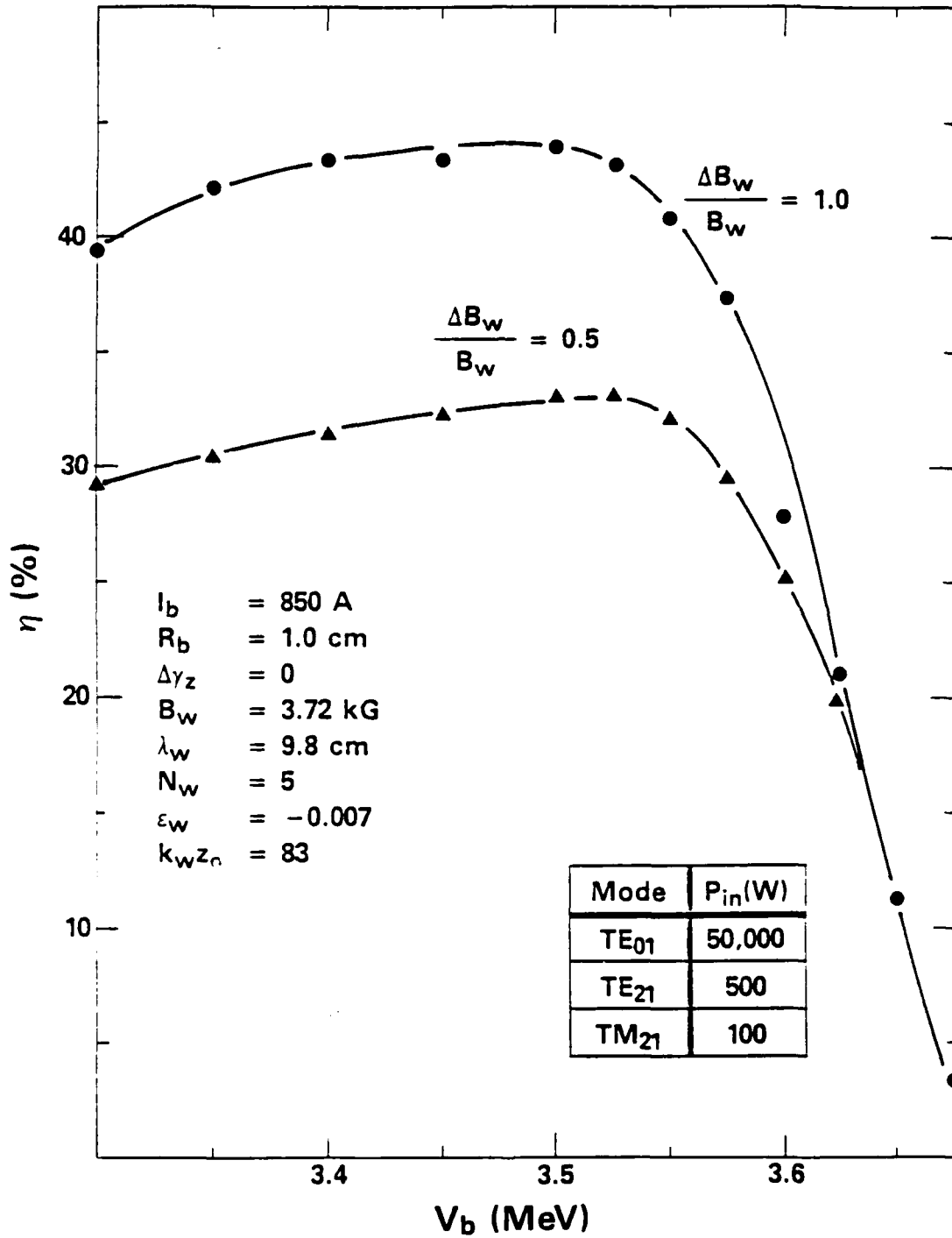


Fig. 8

$a = 9.8 \text{ cm}; b = 2.9 \text{ cm}; \omega/ck_w = 11.3 (34.6 \text{ GHz})$

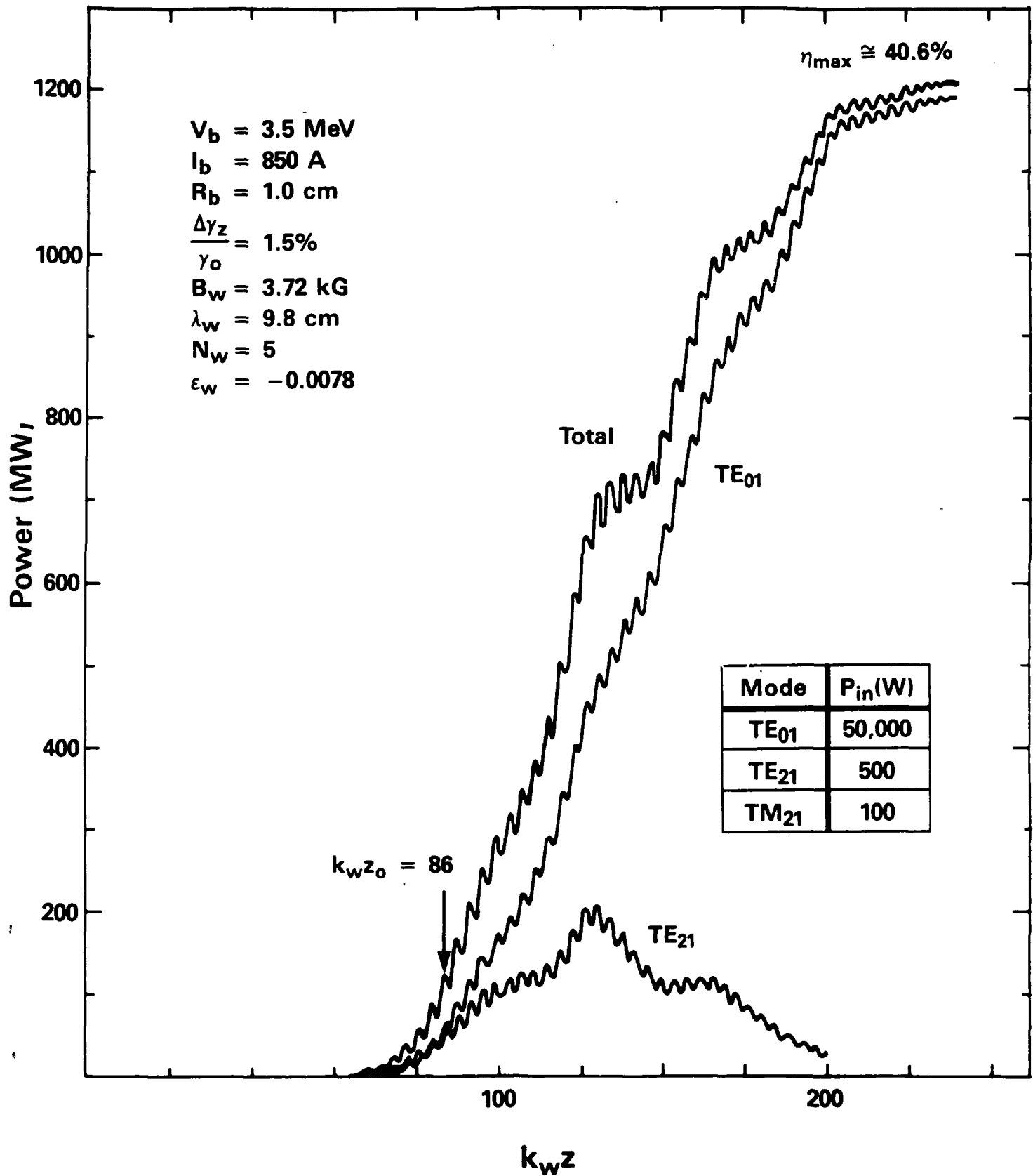
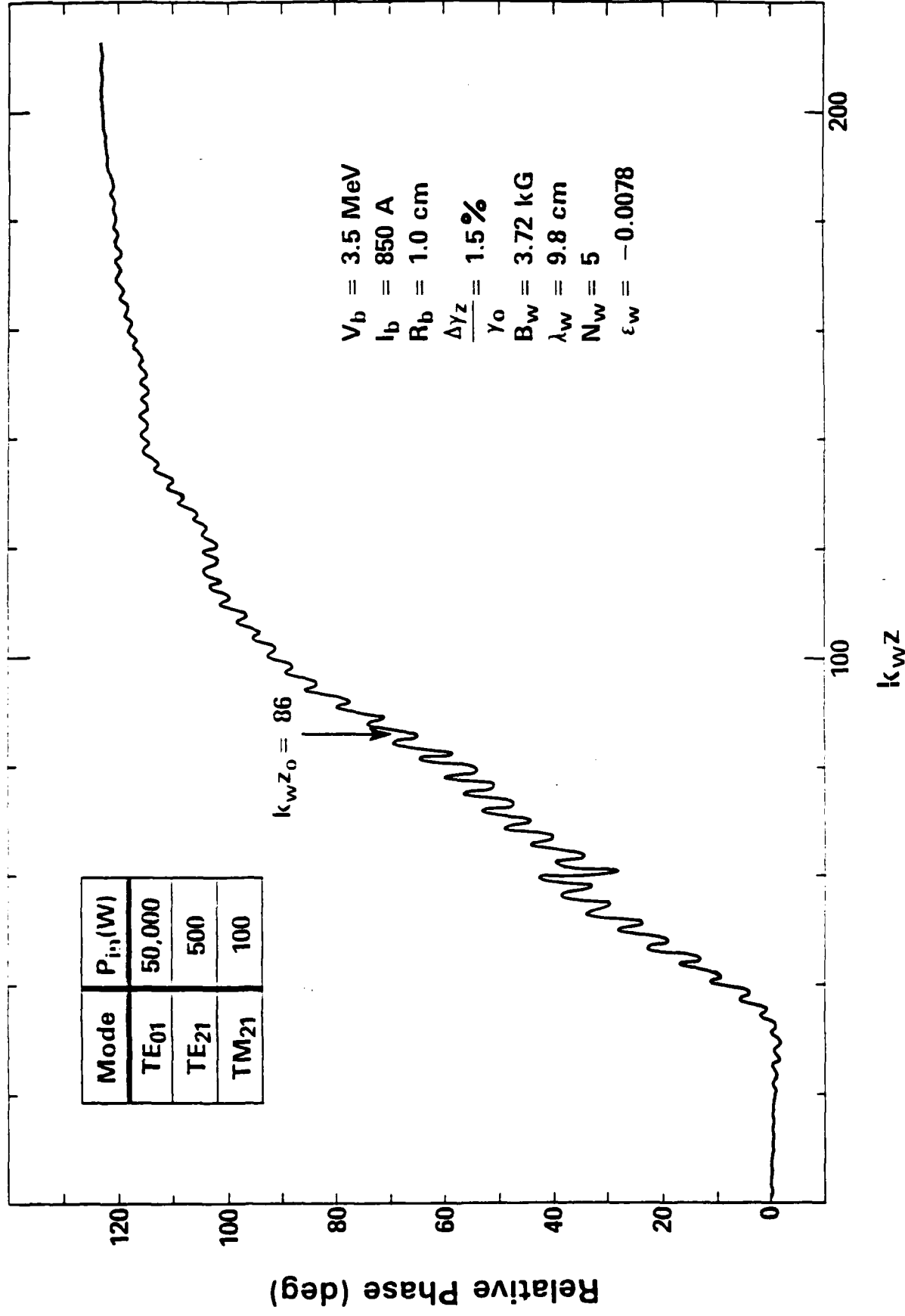


Fig. 9

TE₀₁ Mode (a = 9.8 cm; b = 2.9 cm; $\omega/ck_w = 11.3$)



Mode	P _{i1} (W)
TE ₀₁	50,000
TE ₂₁	500
TM ₂₁	100

$k_w z_0 = 86$

$V_b = 3.5 \text{ MeV}$
 $I_b = 850 \text{ A}$
 $R_b = 1.0 \text{ cm}$
 $\frac{\Delta\gamma_z}{\gamma_0} = 1.5\%$
 $B_w = 3.72 \text{ kG}$
 $\lambda_w = 9.8 \text{ cm}$
 $N_w = 5$
 $\epsilon_w = -0.0078$

FIG. 10

APPENDIX IV

EFFICIENCY ENHANCEMENT IN
FREE-ELECTRON LASERS DRIVEN BY
ELECTROMAGNETIC-WAVE WIGGLERS

Efficiency Enhancement in Free-Electron Lasers Driven by Electromagnetic-Wave Wigglers

HENRY P. FREUND

Abstract—A scheme for efficiency enhancement in free-electron lasers which are driven by electromagnetic-wave wigglers is described which employs a tapered axial guide magnetic field. While tapered magnetostatic wiggler designs have been proven to be an effective means of enhancing the efficiency of free-electron lasers, practical difficulties occur in the design of tapered electromagnetic-wave wigglers. For this reason, it is shown that a tapered axial guide field can be used in concert with an electromagnetic-wave wiggler for the purpose of efficiency enhancement.

AN extensive body of literature currently exists demonstrating the application of the free-electron laser as a source of radiation over an extensive range of wavelengths ranging from the microwave to the optical spectra [1]–[8]. The physical mechanism depends upon the propagation of an electron beam through a periodically rippled magnetic field referred to as the wiggler or undulator. Coherent radiation results from the undulatory motion of the electron beam which permits a wave-particle coupling to the output radiation by means of the ponderomotive potential formed by the beating of the wiggler and radiation fields. The wiggler field itself may be either magnetostatic or electromagnetic in nature. Although the bulk of experiments to date have relied on magnetostatic wigglers, the fundamental principle has also been demonstrated using a large-amplitude electromagnetic wave to induce the requisite undulatory motion in the electron beam [9]. The basic difference between the two classes of wiggler lies in the frequency of the output radiation, which depends upon both the wiggler period and the electron beam energy. In the case of a magnetostatic wiggler, the wavelength of the output radiation scales as $\lambda = \lambda_w / 2\gamma_b^2$ where λ_w denotes the wiggler period and γ_b is the relativistic factor for the beam. In contrast, the wavelength of the output radiation for an electromagnetic-wave wiggler scales as $\lambda = \lambda_w / 4\gamma_b^2$. As a result, for fixed wiggler periods and electron beam energies, the electromagnetic-wave wiggler will produce shorter output wavelengths.

The question addressed in this paper is a method of enhancing the efficiency of a free-electron laser driven by an electromagnetic-wave wiggler. The largest efficiencies observed with uniform magnetostatic wigglers are in the

neighborhood of 13 percent [10], [11]. The term "uniform" in this sense refers to a wiggler with a constant amplitude and period. Although such efficiencies have not yet been observed with electromagnetic-wave wigglers, the number of such experiments is small and there is no reason to think that such efficiencies are not possible. However, for many applications, higher efficiencies are desirable. The theory of efficiency enhancement by means of tapered magnetostatic wigglers has been amply discussed in the literature [12]–[17] and may be affected by either a tapered amplitude or period. Recently, experimental confirmation of the theory has demonstrated that efficiencies in the neighborhood of 35 percent are possible using tapered magnetostatic wigglers [18]. As in the case of magnetostatic wigglers, efficiency enhancement can also be achieved in free-electron lasers using tapered electromagnetic-wave wigglers. However, while tapered magnetostatic wigglers are relatively easy to design and construct, tapered electromagnetic-wave wigglers present technical difficulties in design due to problems in mode control. In particular, the coupling coefficient between modes in a tapered waveguide depends upon the slope of the taper. Difficulties may ensue, therefore, if the slope of the taper is comparable to the coupling coefficient describing the free-electron laser interaction.

For this reason, an alternate efficiency enhancement scheme is described in this paper which relies on a configuration in which a tapered axial guide field is used in addition to an electromagnetic-wave wiggler. This approach has the advantage of extreme ease of construction. Configurations in which an axial guide field is used have been analyzed both for magnetostatic and electromagnetic-wave wigglers [19]–[21]. The axial guide field is often employed for the purpose of confining the electron beam against the effects of self-fields, and enhancements in both the gain and efficiency are found both in theory and experiment [3] for a sufficiently strong *uniform* axial guide field that the Larmor period is comparable to the wiggler period. The essential point which should be emphasized here is that a *tapered* axial guide field can be used to enhance the efficiency of a free-electron laser without the necessity of a strong guide field.

Efficiency enhancement by means of a tapered guide field has been analyzed for free-electron lasers with magnetostatic wigglers [17], [22]. In order to formulate the problem for an electromagnetic-wave wiggler, we assume that the axial guide field is uniform for $z < z_0$ and displays

Manuscript received October 17, 1986; revised May 5, 1987. This work was supported by the Office of Naval Research and the Office of Naval Technology.

The author is with Science Applications International Corporation, McLean, VA 22102, on leave at the Naval Research Laboratory, Washington, DC 20375.

IEEE Log Number 8715826.

a linear taper thereafter. Thus,

$$B_0(z) = \begin{cases} B_0; & z < z_0 \\ B_0[1 + \kappa_0(z - z_0)]; & z > z_0 \end{cases} \quad (1)$$

where B_0 is a constant amplitude and $\kappa_0 (\equiv d \ln B_0(z)/dz)$ represents the inverse scale length for variation of the axial field. The electromagnetic wiggler is represented by a vector potential of the form

$$A_w(z, t) = -\frac{B_w}{k_w} [\hat{e}_x \cos(k_w z + \omega_w t) + \hat{e}_y \sin(k_w z + \omega_w t)] \quad (2)$$

where B_w denotes the amplitude of the wiggler magnetic field and (ω_w, k_w) are the frequency and wave vector. Observe that for positive ω_w , the Poynting flux is directed antiparallel to the z axis. The radiation field is assumed to be propagating parallel to the z axis, and is represented by a plane wave

$$\delta A(z, t) = \delta A(z) [\hat{e}_x \cos(kz - \omega t) - \hat{e}_y \sin(kz - \omega t)] \quad (3)$$

where $\delta A(z)$ denotes the slowly varying amplitude of the vector potential, ω is the frequency, and k is the wave vector. The electron beam equilibrium is described by the steady-state trajectories of electrons in the combined wiggler and axial fluid fields [19], [20]; hence, the equilibrium velocity is

$$v_0 = v' [\hat{e}_x \cos(k_w z + \omega_w t) + \hat{e}_y \sin(k_w z + \omega_w t)] + v' \hat{e}_z \quad (4)$$

where v' is the constant axial velocity,

$$v' = \frac{\Omega_w(\omega_w + k_w v')}{k_w [\Omega_w - \gamma_0(\omega_w + k_w v')]} \quad (5)$$

$\Omega_w \equiv |eB_w/mc|$, and

$$\gamma_0 = \left(1 - \frac{v_w^2}{c^2} - \frac{v'^2}{c^2}\right)^{-1/2} \quad (6)$$

We now determine the response of the electron beam to the radiation field, and write $v = v_0 + \delta v$ and $\gamma = \gamma_0 + \delta\gamma$ to first order in δA . The perturbed orbit equations have been solved for the case of a uniform axial guide field [21]. Based upon this analysis, the perturbed orbit equations can be shown to reduce to

$$\frac{d^2}{dz^2} \psi = K^2 (\sin \psi - \sin \psi_{res}) \quad (7)$$

where $\psi = (k + k_w)z - (\omega - \omega_w)t$ is the particle phase with respect to the ponderomotive wave,

$$K^2 = \frac{(k - k_w)^2 c}{\gamma_0 \gamma_w^2 v_w} \beta_w \delta a \Phi \quad (8)$$

and

$$\sin \psi_{res} \equiv \frac{\kappa_0 \gamma_0}{\omega_w \beta_w \delta a} \left[\frac{\Phi - 1}{\Phi} \right] \left[1 + \frac{\omega_w v_w}{ck_w c} \right]^{-1} \times \frac{\omega_w + k_w v_w}{(k + k_w)c} \quad (9)$$

In (8) and (9), $\delta a \equiv e\delta A/mc^2$, $\beta_w \equiv v_w/v_w$, $\gamma_w \equiv (1 - v_w^2/c^2)^{-1/2}$, and

$$\Phi \equiv 1 - \left[\frac{k_w v_w}{\omega_w + k_w v_w} \right]^2 \left[1 + \frac{\omega_w v_w}{ck_w c} \right]^2 \times \frac{\gamma_w^2 \beta_w^2 \Omega_0}{\left[1 + \frac{v_w^2}{c^2} \frac{(c^2 k_w^2 - \omega_w^2)}{(\omega_w + k_w v_w)^2} \right] \Omega_0 - \gamma_0(\omega_w + k_w v_w)} \quad (10)$$

Equation (7) describes the trapping of electrons in the ponderomotive potential formed by the beating of the wiggler and radiation fields, and is formally identical to the dynamical equation derived for magnetostatic wigglers. In particular, it should be noted that the term in $\sin \psi_{res}$ describes the bulk acceleration or deceleration of electrons due to the tapered guide field.

In order to determine the implications of this equation for the phase trapping on the efficiency enhancement in a tapered system we now calculate the small-signal gain. We assume the system has run to saturation at $z = z_0$, at which point the tapered guide field begins, and we define the gain over a length L relative to this point as

$$G_L \equiv \frac{\delta a(z = z_0 + L) - \delta a(z = z_0)}{\delta a(z = z_0)} \quad (11)$$

As a consequence, it may be shown that [21]

$$G_L = -\frac{\omega_h^2}{2kc^2} \frac{v_w}{c\delta a(z_0)} \int_{z_0}^{z_0+L} dz \langle \sin \psi \rangle \quad (12)$$

where $\langle \dots \rangle$ denotes a phase average over an ensemble of electrons. Since the system is assumed to have reached saturation at $z = z_0$, the bulk of the electron beam has been trapped in the ponderomotive potential and $\psi = \psi_{res}$. Hence,

$$G_L = \frac{\omega_h^2}{2c^2 k_w^2} \frac{\gamma_0 \beta_w^2}{\delta a^2(z_0)} \kappa_0 L \left[\frac{1 - \Phi}{\Phi} \right] \left[1 + \frac{\omega_w v_w}{ck_w c} \right]^{-1} \times \frac{k_w(\omega_w + k_w v_w)}{k(\omega - \omega_w)} \quad (13)$$

The efficiency enhancement $\Delta\eta(L)$ can be calculated by taking the ratio of the increase in the Poynting flux to the power flux of the electron beam. Since the Poynting flux increases by an amount $\Delta S = (\omega k/2\pi) G_L \delta A^2(z = z_0)$, the efficiency enhancement is

$$\Delta\eta(L) = \beta_{\parallel}^2(\kappa_0 L) \left[\frac{1 - \Phi}{\Phi} \right] \cdot \left[1 + \frac{\omega_w v_{\parallel}}{ck_w c} \right]^{-1} \frac{\omega(\omega_w + k_w v_{\parallel})}{k_w v_{\parallel}(\omega - \omega_w)}. \quad (14)$$

Observe that the efficiency enhancement for the case of the magnetostatic wiggler [22] is recovered in the limit as $\omega_w \rightarrow 0$.

In order to obtain estimates of the efficiency enhancements possible, we consider parameters consistent with those discussed previously [21], [22]. Specifically, we choose $\gamma_0 = 3.5$, $\Omega_w/\gamma_0 ck_w = 0.05$, $\omega_b/\gamma_0^{1/2} ck_w = 0.1$, and we assume that $\lambda_w = 1$ cm. We first consider Group I orbits for which $\Omega_0 < \gamma_0(\omega_w + k_w v_{\parallel})$ and we let $\Omega_0/\gamma_0 ck_w = 0.5$. This corresponds to an axial magnetic field of 18.7 kG. In order to obtain the frequency of the electromagnetic wiggler, we must solve the electron orbit equations [(5) and (6)] together with the dispersion equation for an electromagnetic wave in a uniformly magnetized plasma [21]. For this choice of parameters, we obtain $\omega_w/ck_w = 1.007$ (i.e., 30.2 GHz), and the interaction occurs at a resonant frequency $\omega/ck_w = 44.57$ with a wavelength of 0.22 mm. The orbit parameters are $\beta_{\parallel} = 0.956$, $v_w/c = 0.067$, and $\Phi = 1.018$. As a consequence, the efficiency enhancement per unit length is approximately $\Delta\eta(L)/L \sim -0.035 \kappa_0$. Thus, if we taper the axial field downward, then we obtain an efficiency enhancement of 3.5 percent if we taper the field to zero (i.e., $\kappa_0 L = -1$). As the resonance is approached more closely, the efficiency enhancement increases. To see this, we observe that if we double the magnetic field ($B_0 = 37.5$ kG and $\Omega_0/\gamma_0 ck_w = 1.0$) while remaining on Group I trajectories, then we find that $\omega_w/ck_w = 1.010$ (30.3 GHz), $\omega/ck_w = 41.66$ ($\lambda = 0.24$ mm), $\beta_{\parallel} = 0.9529$, $\omega_w/c = 0.1019$, and $\Phi = 1.117$. Hence, $\Delta\eta(L)/L = -0.10 \kappa_0$, and an efficiency enhancement of 10 percent is possible if the axial field is tapered to zero. The efficiency enhancement continues to increase as the resonance at $\Omega_0 \sim \gamma_0(\omega_w + k_w v_{\parallel})$ is approached further; however, v_{\parallel} and the resonant interaction frequency decrease rapidly and it becomes increasingly difficult to obtain short wavelength output radiation. Finally, the mechanism is also operative for Group II trajectories where $\Omega_0 > \gamma_0(\omega_w + k_w v_{\parallel})$, but at the cost of prohibitively high magnetic fields.

While the specific theory of efficiency enhancement described here is directly applicable only to the strong-pump (or Compton) regime of operation in which space-charge fields are negligible, the fundamental mechanism is also appropriate to the collective Raman regime as well. The principal advantage to the tapered-guide field approach to efficiency enhancement is the technical simplicity with which a tapered-guide field can be controlled. This contrasts with the difficulties inherent in the control of a tapered electromagnetic-wave wiggler. It should be re-

marked that the effect of the tapered guide field is resonantly enhanced when $\Omega_0 \sim \gamma_0(\omega_w + k_w v_{\parallel})$ which, depending upon the specific experimental parameters, may require a strong axial field. However, the efficiency enhancement mechanism is operable at all levels of the axial field, and does not require strong guide fields near resonance.

ACKNOWLEDGMENT

The author would like to thank Dr. A. K. Ganguly, Dr. R. K. Parker, and Dr. R. H. Jackson for helpful discussions.

REFERENCES

- [1] L. R. Elias, W. M. Fairbanks, J. M. J. Madey, H. A. Schwettman, and T. I. Smith, *Phys. Rev. Lett.*, vol. 36, pp. 717-720, 1976.
- [2] V. L. Granatstein, S. P. Schlesinger, M. Herndon, R. K. Parker, and J. A. Pasour, *Appl. Phys. Lett.*, vol. 30, pp. 384-386, 1977.
- [3] R. K. Parker, R. H. Jackson, S. H. Gold, H. P. Freund, V. L. Granatstein, P. C. Efthimion, M. Herndon, and A. K. Kinkaid, *Phys. Rev. Lett.*, vol. 48, pp. 238-242, 1982.
- [4] R. W. Warren, B. E. Newnan, J. G. Winston, W. E. Stein, L. M. Young, and C. A. Brau, *IEEE J. Quantum Electron.*, vol. QE-19, pp. 391-401, 1983.
- [5] M. Billardon, P. Elleaume, J. M. Ortega, C. Bazin, M. Bergher, M. Velghe, Y. Petroff, D. A. G. Deacon, K. E. Robinson, and J. M. J. Madey, *Phys. Rev. Lett.*, vol. 51, pp. 1652-1655, 1983.
- [6] J. Fajans, G. Bekefi, Y. Z. Zin, and B. Lax, *Phys. Rev. Lett.*, vol. 53, pp. 246-249, 1984.
- [7] T. J. Orzechowski, B. Anderson, W. M. Fawley, D. Prosnitz, E. T. Scharlemann, S. Yarema, D. Hopkins, A. C. Paul, A. M. Sessler, and J. Wurtele, *Phys. Rev. Lett.*, vol. 54, pp. 889-892, 1985.
- [8] J. Masud, T. C. Marshall, S. P. Schlesinger, and F. G. Yee, *Phys. Rev. Lett.*, vol. 56, pp. 1567-1570, 1986.
- [9] Y. Carmel, V. L. Granatstein, and A. Gover, *Phys. Rev. Lett.*, vol. 51, pp. 566-569, 1983.
- [10] R. M. Phillips, *IRE Trans. Electron Devices*, vol. ED-7, pp. 231-241, 1960.
- [11] J. Fajans, G. Bekefi, Y. Z. Yin, and B. Lax, *Phys. Fluids*, vol. 28, pp. 1995-2006, 1985.
- [12] N. M. Kroll, P. L. Morton, and M. N. Rosenbluth, in *Physics of Quantum Electronics: Free-Electron Generators of Coherent Radiation*, S. F. Jacobs, H. S. Pilloff, M. Sargent, M. O. Scully, and R. Spitzer, Eds. Reading, MA: Addison-Wesley, 1980, vol. 7, ch. 4 and 5, pp. 89-145.
- [13] D. Prosnitz, A. Szoke, and V. K. Neil, in *Physics of Quantum Electronics: Free-Electron Generators of Coherent Radiation*, S. F. Jacobs, H. S. Pilloff, M. Sargent, M. O. Scully, and R. Spitzer, Eds. Reading, MA: Addison-Wesley, 1980, vol. 7, ch. 22, pp. 571-588.
- [14] C. A. Brau and R. K. Cooper, in *Physics of Quantum Electronics: Free-Electron Generators of Coherent Radiation*, S. F. Jacobs, H. S. Pilloff, M. Sargent, M. O. Scully, and R. Spitzer, Eds. Reading, MA: Addison-Wesley, 1980, vol. 7, ch. 24, pp. 647-664.
- [15] P. Sprangle, C. M. Tang, and W. M. Manheimer, *Phys. Rev.*, vol. A21, pp. 302-318, 1980.
- [16] J. M. Slater, J. Adamski, D. C. Quimby, W. M. Grossman, T. L. Churchill, and R. E. Center, in *Proc. Int. Conf. Lasers '82*, R. C. Powell, Ed. McLean, VA: STS Press, 1982, pp. 212-217.
- [17] H. P. Freund and A. K. Ganguly, *Phys. Rev.*, vol. A33, pp. 1060-1072, 1986.
- [18] D. Prosnitz, *Bull. APS*, vol. 31, p. 809, 1986.
- [19] H. P. Freund, R. A. Kehs, and V. L. Granatstein, *IEEE J. Quantum Electron.*, vol. QE-21, pp. 1080-1082, 1985.
- [20] A. Goldring and L. Friedland, *Phys. Rev.*, vol. A32, pp. 2879-2886, 1985.
- [21] H. P. Freund, R. A. Kehs, and V. L. Granatstein, *Phys. Rev. A*, vol. 34, pp. 2007-2012, 1986.
- [22] H. P. Freund and S. H. Gold, *Phys. Rev. Lett.*, vol. 52, pp. 926-929, 1984.



Henry P. Freund was born in New York, NY, on May 23, 1949. He received the B.S. degree in physics from Rensselaer Polytechnic Institute, Troy, NY, in 1971, and the Ph.D. degree in physics from the University of Maryland, College Park, in 1976.

After graduation he spent a year as a Research Fellow at the Institute for Physical Sciences and Technology, the University of Maryland, College Park, MD, and two years as a National Research Council-Naval Research Laboratory Postdoctoral

Research Associate. His current research is devoted primarily to free-electron lasers at the Naval Research Laboratory. At present, he is with the Plasma Physics Division, Science Applications International Corporation, McLean, VA.